Design of Parallel Plate Condensers with Sintered Wicks for a Loop Heat Pipe

by

Catherine Helene Koveal

SUBMITTED TO THE DEPARTMENT OF MECHANICAL ENGINEERING IN PARTIAL FULFILLMENT OF THE REQUIREMENTS FORTHE DEGREE OF

MASTER OF SCIENCE IN MECHANICAL ENGINEERING
AT THE
MASSACHUSETTS INSTITUTE OF TECHNOLOGY

JUNE 2010

Signature of Author: _____
Department of Mechanical Engineering
May 19, 2010

Certified by: _____
Evelyn N. Wang
Assistant Professor of Mechanical Engineering
Thesis Supervisor

Accepted by: _____
David Hardt
Professor of Mechanical Engineering
Chairman, Graduate Thesis Committee

Design of Parallel Plate Condensers with Sintered Wicks for a Loop Heat Pipe

by

Catherine Helene Koveal

Submitted to the Department of Mechanical Engineering
On May 19, 2010 in partial fulfillment of the
Requirements for the Degree of Master of Science in
Mechanical Engineering

Abstract

New innovations and integrations of existing cooling methods are needed to enable high performance operation of high power electronic equipment. Air-cooled solutions are attractive due to their simplicity; however these solutions are normally limited to low power dissipation rates. Through a novel design and integration of a blower and a compact heat exchanger, low thermal resistance and high efficiency heat transfer can be achieved. This device combines the increased surface area of a finned geometry with the isothermal heat transfer of a heat pipe and the low speed operation of integrated fan blades to dissipate 1000 W using 30 W of input electrical power in a 10x10x10 cm^3 volume.

This thesis focuses on the design and experimental validation of the 2.5 mm thick, 200 cm^2 surface area flat plate condenser repeated in parallel in the loop heat pipe structure. The condenser was designed to ensure even mass flow distribution and phase-separation within each layer. To better understand the physics and governing parameters within the thin geometry of the condenser, an experimental setup was designed and fabricated that allowed for visualization and measurement of the condensing flow. Experimental studies were conducted to explore condensation within open and sinter channel geometries while varying flow rate, backside cooling, and gravitational orientation. Open channel flow exhibited sensitivity to cooling heat transfer and orientation resulting in a variable condensing length connected to a sharp drop in surface temperature and gravity-dominated flow patterns. In contrast, testing with sinter wick in the channel demonstrated an isothermal surface over the length of the condenser and gravitationally independent flow stability due to separation of the liquid and vapor phases. The addition of a sub-cooling length within the sinter channel was shown to retain high isothermal temperatures upstream while reducing condensate temperature below saturation before the condenser outlet. However, to prevent large pressure drops incurred by flow through the sinter, balance is required between desired sub-cooling and sinter permeability.

This work demonstrates the potential for a condenser design with a sintered wick and a sub-cooling section to mitigate the failure modes of parallel condensers. These results serve as guidelines for the continued development of the parallel plate condensers for the loop heat pipe integrated into the compact heat exchanger.

Thesis Supervisor: Evelyn N. Wang
Title: Assistant Professor of Mechanical Engineering

Contents

Chapter 1: Background

Air-cooling for Electronics

Demand for smaller handheld devices and faster processing speeds drives development in electronics toward smaller component footprints with enhanced functionality. Following Moore's law, the number of transistors on an integrated circuit has doubled approximately every 2 years leading to an exponential increase in component density and performance over the last several decades [1]. New innovations and integrations of existing cooling technologies are needed to keep up with the continual increase in power density. Although air-cooling is an attractive option due to its simplicity and low cost, devices utilizing fans and finned surfaces are typically limited to low heat flux applications [2]. To improve heat transfer, cooling designs augment surface area with large fins, imbedded fans, and incorporated heat pipes to transfer heat from the base as shown in Fig. 1-1. Even with these modifications, active cooling devices with footprints on the order of 10 cm x 10 cm x 10 cm are typically only capable of maximum power dissipations of 150 W at thermal resistances larger than 0.2 °C/W [3]. The integrated heat pipes use passive, internal phase-change to efficiently transfer heat to the fins. However, the small heat pipe contact area, typically 6 mm in diameter, and the thin geometry of the metal fins leads to high conduction resistance. This resistance to lateral heat spreading makes the fins susceptible to large temperature gradients that degrade heat transfer to the cooling air. To improve the performance of these cooling devices and expand their function to higher heat dissipations, the bottleneck of heat transfer to the air must be addressed.

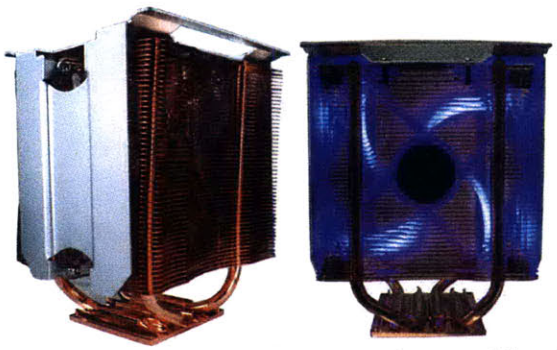

Fig. 1-1 Images of Kingwin KA-9226ACU CPU cooler capable of 150 W of power dissipation at 0.23 °C/W with dimensions of 92mm (L) x 74mm (W) x 113mm (H) [5].

Heat Pipe Design

Heat pipes leverage a fluid's ability to absorb or reject latent heat during phase-change to efficiently transfer heat between heating and cooling sources. Conventional heat pipes contain a saturated working fluid inside a sealed, high conductivity tube with a wick structure along the inside wall. When heat is applied to one end, the working fluid in the wick evaporates and flows to the cooler end of the pipe where it condenses onto the wick and then returns to the evaporator by capillary action at the wick interface [6]. As shown in Fig. 1-1, heat pipes are typically used as a passive transfer route from the hot component to the fins. In this application, optimization of the number of heat pipes involves a balance between improving the temperature uniformity of the fins and reducing impediments and disruption to the cooling airflow. Ultimately if the uniform temperature heat rejection of the heat pipe condenser could be applied over the entire fin surface area, the device could achieve much higher heat fluxes to the air.

Loop Heat Pipes

Loop heat pipes (LHP) have all the advantages of conventional heat pipes but additionally can operate over long distances and against gravity. By removing the wick from the liquid and vapor lines, the pressure drops in the system are reduced allowing the

capillary pumping mechanism to operate at higher heat transport limits. The evaporator in a LHP is designed for flow through the thickness instead of the length of the wick such that a fine pore material can be used to provide large capillary driving pressures without incurring large viscous pressure drops [7]. Recent literature has investigated the modeling and testing of a flat evaporator that could mate directly to components and thereby act as the base of a CPU cooler [9]. However typically, the condenser for a LHP is formed by routing open tubing through a section with fins or liquid cooling. The few examples of condenser design in a flat form factor are aimed at creating a stable separation of liquid and vapor phases by incorporating a wick structure [12]. The condenser wick improves startup by eliminating the need to clear vapor lines of liquid and thus preventing early evaporator dryout due to high pressures. For this reason, visualization was limited to monitoring the formation vapor bubbles as indicators of dryout in the compensation chamber on the backside of the primary wick. These designs relied on liquid cooling due to the limited surface area of the single condenser. For direct air-cooling in these LHPs, the condensation surface area must be significantly increased, potentially by using multiple condensers in parallel.

Condensing Flow / Condenser Design

For a conventional LHP condenser, the flow becomes two-phase within the cooled pipe until the vapor completely transitions to liquid. Two-phase flow patterns have been well-studied analytically and experimentally in literature for round and even square pipe geometry, therefore flow transitions in conventional condensers can be accurately predicted [14]. For large scale pipes, flow patterns are typically determined by a balance of shear forces and gravity. As dimensions reduce to the millimeter scale,

surface tension plays a dominant role and flow patterns are affected by all three forces [15]. Flat condensers have one dimension on the order of the capillary length and another more macroscale, therefore the flow patterns are a combination of both regimes and difficult to define accurately using the mapping provided in literature. Incorporation of a wick into the condenser will further affect condensation flow patterns, as well as the overall pressure drop in the LHP. This work aims to visualize condensation within flat geometries, both open channel and with wick, to develop a stable parallel condenser design for improved heat transfer by air cooling.

In this thesis, Chapter 2 describes the current loop heat pipe design and uses analytical calculations and modeling to support the incorporation of geometric features such as sinter wick in the condenser. Chapter 3 describes three deaeration methods that were experimentally investigated for removing non-condensable gases from the DI water working fluid prior to use in a condensing flow setup or the eventual heat pipe. Chapter 4 describes multiple revisions of the condensing flow experimental apparatus including a vapor generation system, test section for flow visualization, and measurement instrumentation. Chapter 5 describes the experimental testing that was performed on geometry similar in dimension to the heat pipe condenser design. The testing compared condensing flow in open channel, sinter wick, and sub-cooling section geometries while varying gravitational orientation, mass flow rate, and backside cooling heat transfer. Finally, Chapter 6 explains the conclusions for condenser design that can be drawn from this experimental work and details the future work leading to the manufacture of the complete loop heat pipe and high power heat exchanger.

Chapter 2: Loop Heat Pipe Design

Overview

The goal of this research is to develop a novel heat exchanger capable of dissipating 1000 W of heat using only 33 W of input power for air-cooling. To achieve a low thermal resistance of 0.05 °C/W, the heat exchanger incorporates a loop heat pipe for efficient heat transfer from a single heated surface to multiple parallel plate condensers. The performance demands of the heat exchanger and the parallel plate geometry heavily influence the condenser structure driving the need for an experimental setup to validate the design.

Motivation

The primary motivation for this experimental research was involvement in the Microtechnologies for Air-Cooled Exchangers Program (MACE) funded by the Defense Advanced Research Projects Agency (DARPA) under the Microsystems Technology Office (MTO). As shown in Table 2-1, the MACE program challenges participating teams to develop an air-cooled heat exchanger capable of dissipating 1000 W of power with a COP of 30. The device cannot exceed the volume of a 4" cube with uniform heat input over a 4" square area. A thermal resistance of 0.05 °C/W with 1000 W of heat transfer indicates that the surface of the cooled device should be 80 °C if the local air temperature is 30 °C.

Table 2-1 Matrix of heat exchanger performance requirements for the DARPA MACE program compared to current state-of-the-art heat exchangers.

Pumped Heat Exchanger Metrics	State-of-the-Art	Phase I (0-18 months)	Phase II (18-36 months)
Heat Sink Total Thermal Resistance	0.2 C/W	0.05 C/W equivalent	0.05 C/W
Total Heat Sink Size	4"x 4" x 4"	single "layer"	< 4"x 4" x 4"
System Coefficient of Performance	10	30	30
Electronic Power Dissipation	1000 W	1000 W/no. of layers	1000 W
Application Specific Metrics			
Heat Sink Lifetime	Infinite	170 hours	>10,000 hours
Storage Temperatures (min to max)		-54°C to 100°C	-54°C to 100°C
Shock G Loads (11 ms duration)		10 G	10 G

Overall Heat Exchanger Design

The heat exchanger design, shown in the schematic in Fig. 2-1, was developed to achieve the MACE program requirements. The program has just entered its second phase with a year and a half of development time remaining. Therefore, the device described in the following sections is the current design that is continually evolving based on experimental findings. The device integrates the airflow of an impeller with the increased surface area of a finned heat sink and the isothermal heat transfer of a heat pipe. The heat exchanger aims to remove 1000 W of heat at a power density of 10 W/cm^2 using air-cooling and less than 33 W of electrical power. In addition to efficient heat transfer, the heat exchanger must also be able to operate stably in any gravitational orientation. The heat pipe structure allows for efficient transfer of the heat from the single bottom surface to the multiple condenser layers with little temperature change. By interleaving the impellers with the condenser layers, high heat transfer to the air can be achieved while the impellers are spinning at speeds and torques manageable with low input power to the motor. The efficient heat transfer from the 80 °C base to 30 °C ambient air allows the device to achieve a thermal resistance of 0.05 °C/W. The heat exchanger operates in the following manner. The 1000 W of heat is input at the bottom

surface of the device and transferred at 80 °C to the multiple (15) condensers by evaporation of the heat pipe working fluid, which is water. The permanent magnet synchronous motor mounted at the top of the device spins a shaft and the 15 attached impeller blades to generate airflow that enters through the central core and exhausts over the condenser surfaces. The impellers are able to dissipate the heat from the nearly 80 °C condensers with a heat transfer coefficient of 100 W/m^2K to the air. This high heat transfer is due to a combined effect of convection across the layers from radial outflow at 5000 rpm and the continual shearing off of the airflow boundary layer by the impeller due to the 500 μm clearance between the impeller and the condenser.

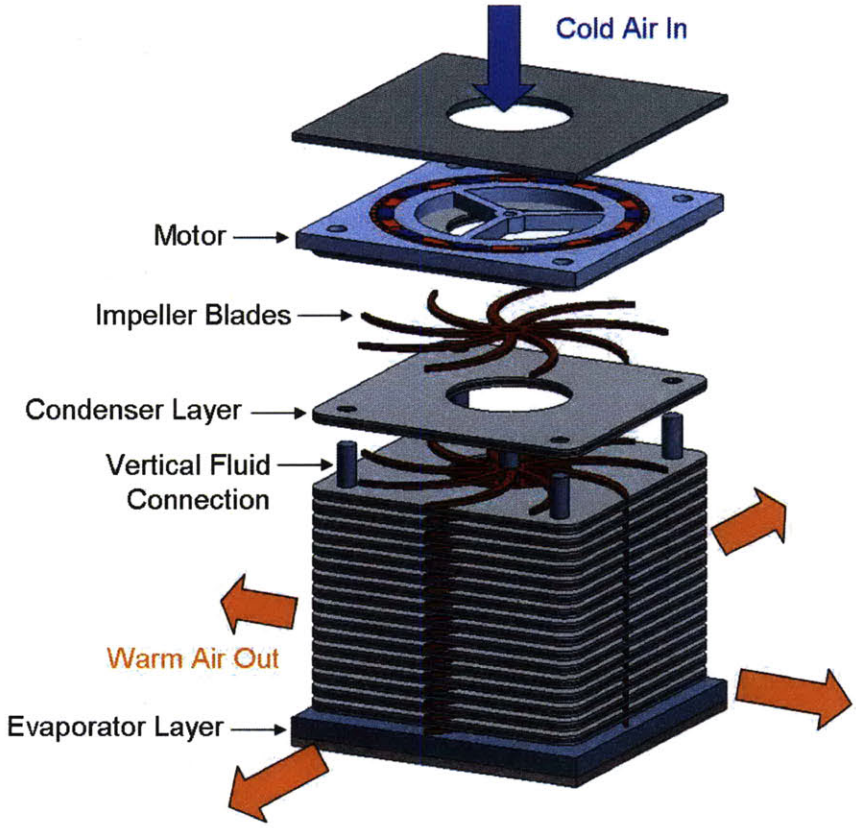

Fig. 2-1 Exploded view schematic of the current heat exchanger concept. Heat is input at the bottom evaporator layer and transferred isothermally by the heat pipe structure to the multiple condenser plates. The condensers are convectively cooled by the motor-driven impeller blades.

Conventional Loop Heat Pipe (LHP) Design

The heat pipe incorporated into the heat exchanger is a loop heat pipe design. Loop heat pipes (LHPs) are typically used in applications requiring large driving capillary pressure due to a long distance between the evaporator and condenser or multiple Gs of gravity force. In the case of this heat exchanger design, a LHP was implemented to handle the pressure drops from incorporation of sintered wick in the condensers in addition to the gravity head on the liquid lines.

A schematic of a conventional LHP is shown in Fig. 2-2. The evaporator is typically cylindrical with a single line for fluid circulation looping through the condenser and back to the reservoir. The reservoir within the evaporator acts as a constant liquid supply to the primary wick. When heat is applied at the outside wall, the working fluid evaporates from the liquid-vapor interface at the wick surface. The meniscus at the liquid-vapor interface is curved due to the pressure difference between the phases and this pressure difference acts as a capillary pump to circulate the working fluid in the heat pipe. The vapor generated in the evaporator moves nearly isothermally through an open line to the condenser. Heat removal from external air or liquid cooling causes the vapor to condense and, in small diameter lines, form a meniscus of between the vapor and liquid sides of the loop. As the cooling rate is varied, the location of the meniscus, also called the condensing length, will adjust according to the heat transfer. Downstream of the condenser, the condensed liquid flows back to the reservoir to restart the phase-change cycle.

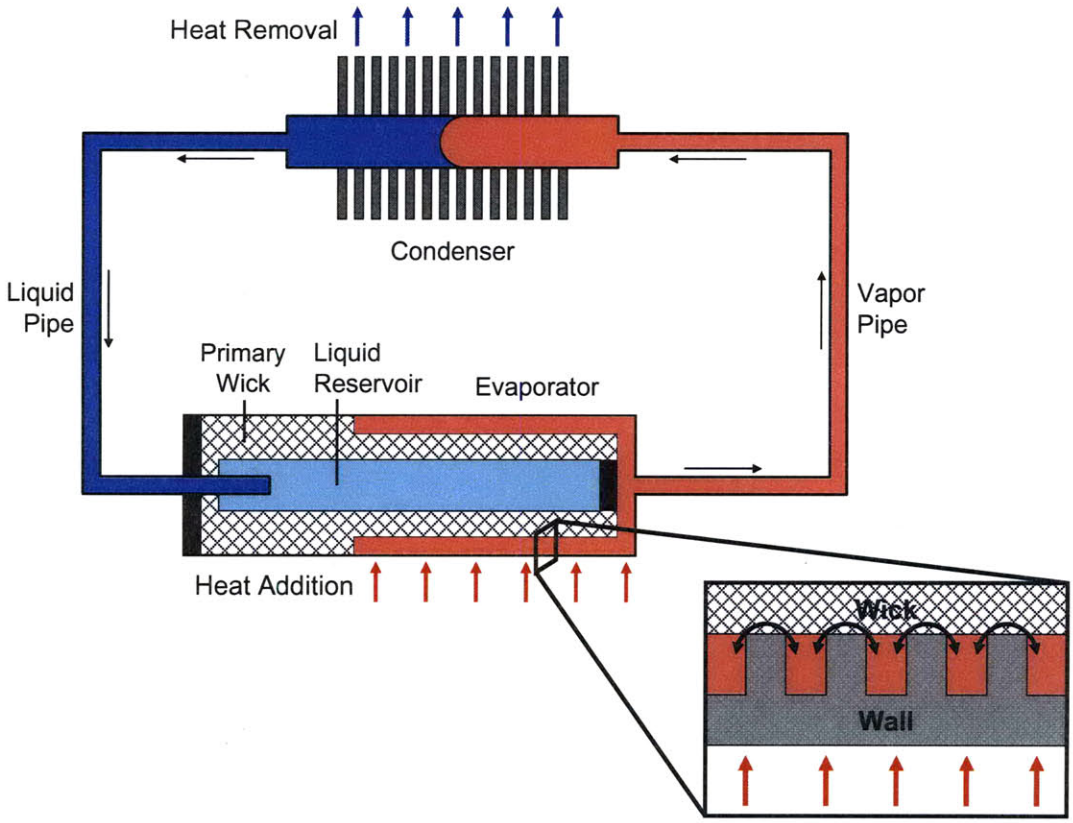

Fig. 2-2 Schematic of working fluid circulation within a standard cylindrical loop heat pipe.

LHP Design for Heat Exchanger

Overall LHP Design

The heat pipe incorporated within the heat exchanger uses all of the conventional LHP components; it just orients them into flat plate geometries and expands the cooling to multiple condensers in parallel. As shown in the schematic in Fig. 2-3, the bottom of the evaporator is copper to effectively spread any non-uniformity of the 1000 W of heat over the entire base. The heat conducts through the copper teeth and evaporates the working fluid, water, at the primary wick surface. The wick is fabricated from high conductivity copper sinter near the teeth to spread the incoming heat flux and low conductivity stainless steel sinter adjacent to the reservoir to maintain a temperature difference across the evaporator wick. The sinters used for the 4 mm thick primary wick

are on the order of 5-15 μm to provide high capillary driving pressure for the LHP. Once formed, the vapor flows through the copper base in channels formed by the teeth, up the 6 mm diameter stainless steel vapor pipes, and branches into each of the 15 condenser layers. The air-cooling over the exterior of the condenser causes the vapor to condense on the internal copper sinter surface. The liquid then flows through the wick, past the sub-cooling section, and recombines in the 6 mm diameter stainless steel liquid pipes. The liquid then flows back to the compensation chamber on the backside of the primary wick where it continually feeds liquid to the evaporating interface. Air-cooling over the top copper surface of the evaporator and the insulating primary wick ensure that the liquid in the compensation chamber remains saturated at a lower temperature than the evaporating surface. Additionally, this cooler saturation condition in the compensation chamber enables the wick in the condenser to operate with a receding meniscus. In order for water to change phase at 80 °C, the entire device must be pulled down to a vacuum pressure of 47.4 kPa. To hold vacuum, each layer is sealed with sheets of medium temperature braze and all joints between the fluid pipes and the layers are sealed with rings of low temperature braze.

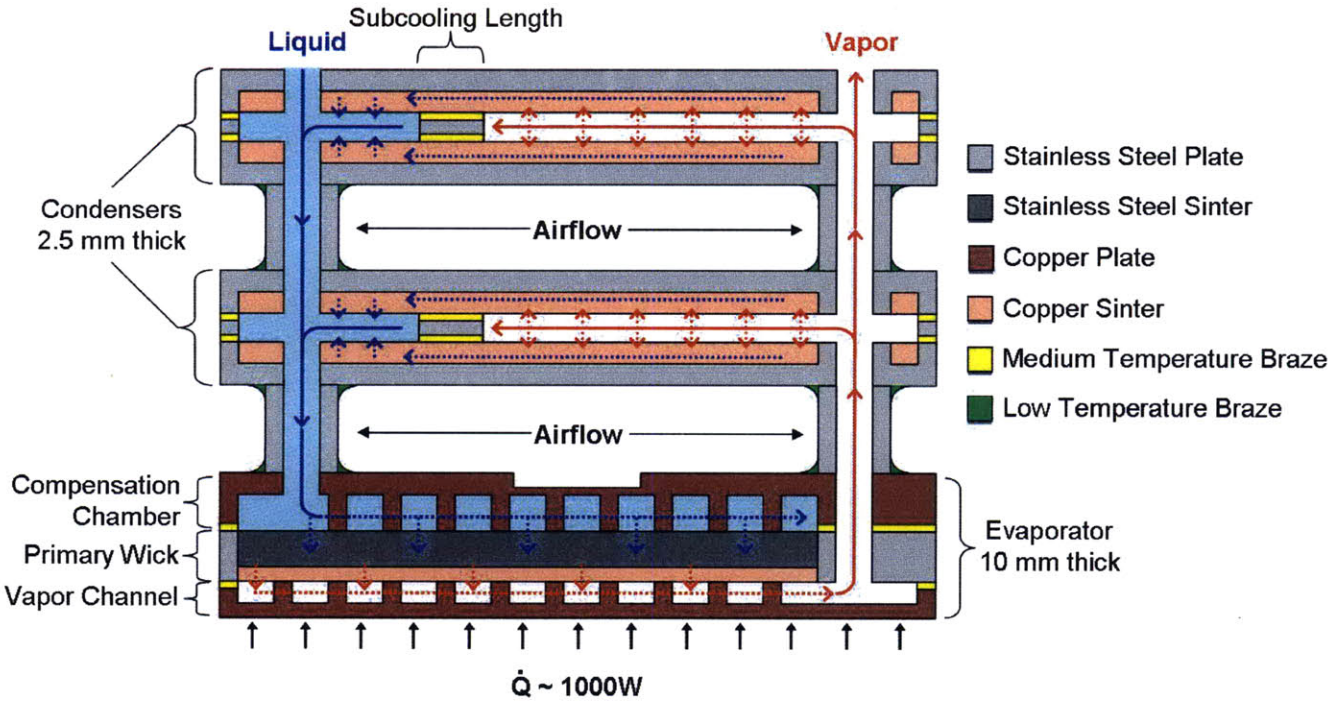

Fig. 2-3 Schematic showing the circulation of working fluid (water) inside the current Phump loop heat pipe.

Condenser Design

As shown in Fig. 2-4, the condenser plates are manufactured by a combination of MEMS fabrication, machining, and high temperature sintering. In step (1), the 1 mm thick stainless steel plate is chemically etched to form a 0.5 mm deep recess for the sinter. In step (2), the through holes are machined to a diameter allowing for a close-fit of the vertical fluid pipes. In step (3), alumina plugs are placed in the vapor inlet holes and the plate is filled with 75-100 μm diameter copper sinter powder. In step (4), after loose sintering the plate, the ceramic plugs are removed. As shown in Fig. 2-5, these plates are used as the top and bottom surface of the condenser with a similarly manufactured frame brazed in-between. The frame acts as a spacer to create the 0.5 mm thick vapor channel and the sub-cooling section.

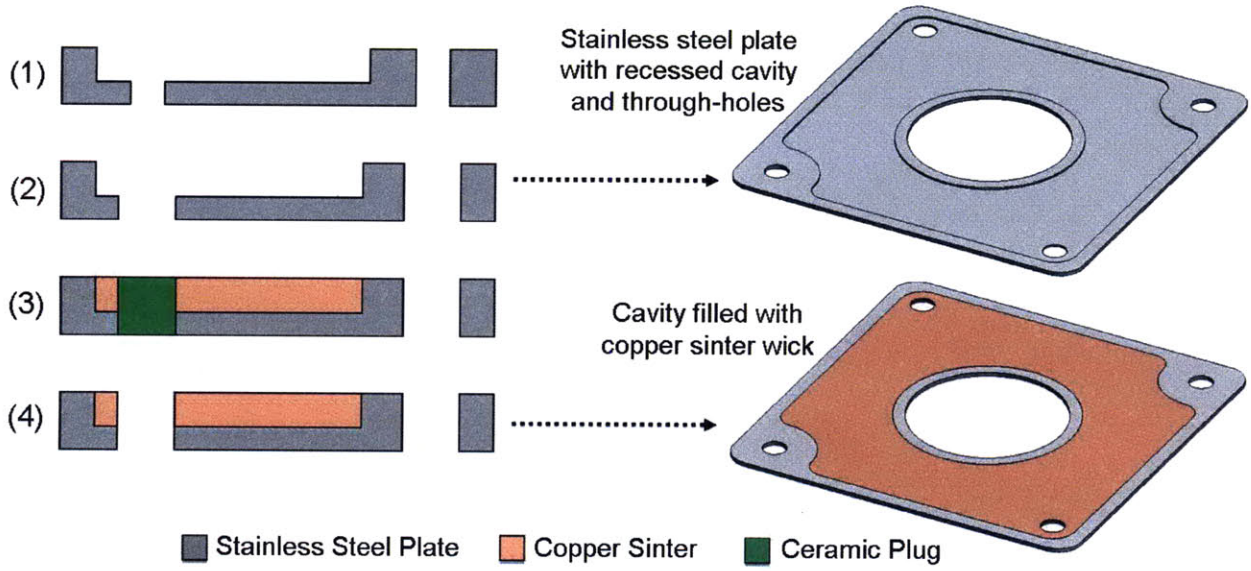

Fig. 2-4 Schematic of MEMS fabrication process to produce sinter-coated condenser plates including 3D images of steel plates after chemical etching and sintering.

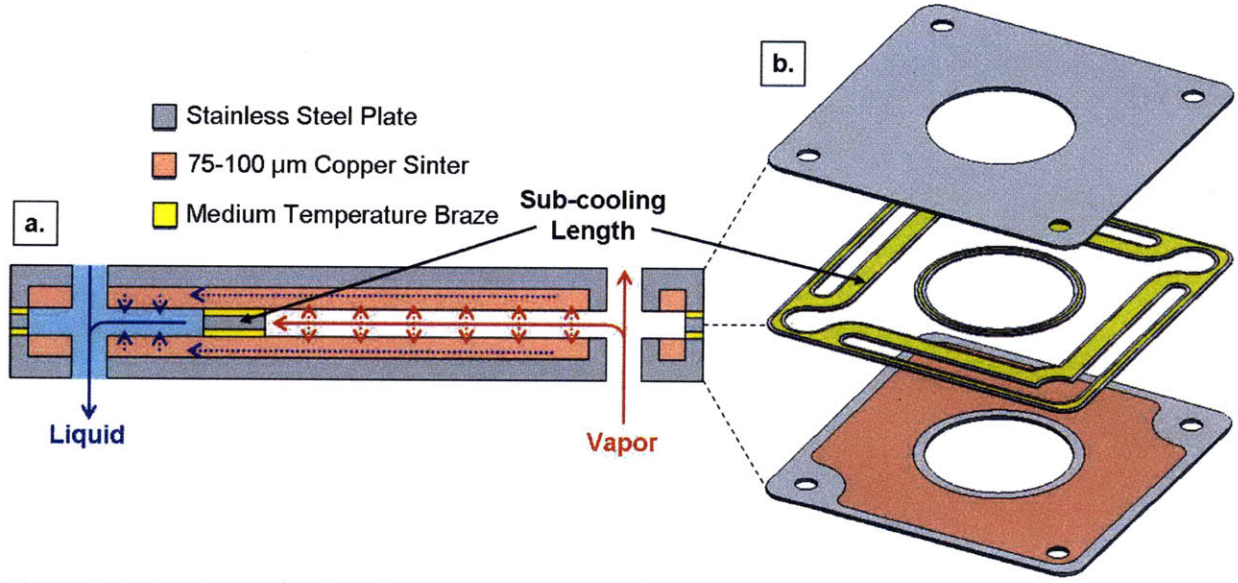

Fig. 2-5 (a.) Schematic showing a cross-section of the current condenser design and the flow path of the working fluid. (b.) 3D exploded view of the condenser to relate the cross-section to the physical design.

The parallel orientation of the condensers and the performance demands of the heat exchanger resulted in a condenser design of its current form. The condensers are fabricated from stainless steel plates to ensure structural rigidity and flatness of the thin parallel layers. Copper sinter is lined along the entire interior surface to facilitate

uniform condensation upstream of the sub-cooling section. This even condensation results in an isothermal surface over a majority of the condenser maximizing the heat transfer to the air. Although both stainless steel and the copper wick have low thermal conductivity on the order of 15 W/mK, the thin layers result in a low temperature between the vapor space and the condenser surface. Copper sinter in the range of 75-100 μm was used in the condensers for maintaining high permeability and a maximum capillary pressure of 5.6 kPa when operated with a receding meniscus. The receding meniscus set by the compensation chamber is key for preventing flooding of the lower condenser layers with wicks of this pore size due to the 1 kPa gravity head of a 10 cm column of liquid. To prevent re-vaporization of the liquid as it exits the wick into the liquid line, a 7 mm long sub-cooling section was added to the condenser. The section was sized such that the balance of temperature drop due to sensible heat and pressure drop from forcing flow through the wick result in a sub-cooled liquid state at the end of the condenser. Additionally, the pressure drop through the sub-cooling section effectively acts as a flow restrictor to ensure even mass flow distribution into each condenser layer. Essentially, as long as the pressure drops within the condenser exceed the pressure drops due to gravity and the viscous losses in the vapor and liquid pipes, the mass flow will be equal in each condenser. Even mass flow is desired so that the potential for heat transfer to the air is maximized in each layer.

Current LHP Design Calculations

For the LHP to function properly, the primary wick must provide enough driving capillary pressure to overcome the sum of the pressure losses within the system. These

pressure drops are caused by viscous losses, body forces, and capillary interfaces in the evaporator, condenser, vapor line and liquid line.

$$\Delta P_{cap,\max} \geq \Delta P_{evaporator} + \Delta P_{vapor} + \Delta P_{condenser} + \Delta P_{liquid} + \Delta P_{gravity} \tag{2.1}$$

The capillary pressure of the primary wick is determined by the Young-Laplace equation (2.2) as a function of wick effective pore radius (r_{eff}), the wetting contact angle of fluid on the wick (Θ), and the working fluid surface tension (σ).

$$\Delta P_{cap,\max} = \frac{2\sigma \cos \Theta_{receding}}{r_{eff}} \tag{2.2}$$

The contact angle of the working fluid on a certain wick material can vary within a range of values from a minimum receding angle ($\Theta_{receding}$) to a maximum advancing angle. The wick will operate at maximum capillary pressure with a receding contact angle.

For flows through open channels, such as the liquid and vapor pipes, the viscous pressure drop can be calculated with the Darcy–Weisbach equation:

$$\Delta P = f \frac{L}{D_h} \left(\frac{\rho v^2}{2} \right) \tag{2.3}$$

The equation is a function of Darcy friction factor (f), flow length (L), hydraulic diameter (D_h), density (ρ) and flow velocity (v). The hydraulic diameter can be calculated, for a circular pipe, as the diameter (D_h=D) or, for a rectangular pipe with side lengths a and b, as 4 times the area over the perimeter also written as

$$D_h = \frac{2ab}{a+b} \tag{2.4}$$

The mass flow rate ($\dot{m}$) circulating inside the heat pipe is generated by phase-change of the working fluid due to heat input into the evaporator. For the 1000 W known heat input

(Q) and working fluid heat of vaporization (h_{fg}), the total mass flow is defined as $\dot{m}_t = Q / h_{fg}$. If there are multiple (N) channels, the mass flow rate per channel is defined as $\dot{m} = Q / Nh_{fg}$. The flow velocity (v) is determined from the mass flow rate as a function of the density (ρ) and the channel cross sectional area (A) as $v = \dot{m} / \rho A$. The Reynolds number as a function of hydraulic diameter for the open channel flow is calculated as the following where the working fluid viscosity is μ:

$$\mathrm{Re}_{D_h} = \frac{\rho v D_h}{\mu} = \frac{Q D_h}{N h_{fg} A \mu} \tag{2.5}$$

For turbulent flow (Re > 2300), the friction factor can be calculated using [25]:

$$f = \left(0.79 \ln\left(\mathrm{Re}_{D_h}\right) - 1.64\right)^{-2} \tag{2.6}$$

For laminar flow (Re < 2300) through a circular pipe, the friction factor can be calculated as f = 64 / Re. Using this correlation and the velocity definition, Eqn. 2.3 can be modified into the Hagen–Poiseuille equation:

$$\Delta P = \frac{128 \mu L \dot{m}}{\rho \pi D^4} = \frac{128 \mu L Q}{\rho \pi D^4 N h_{fg}} \tag{2.7}$$

For laminar, fully developed flow in rectangular ducts with an aspect ratio α = b / a, the friction factor can be approximated as [17] :

$$f = \frac{24}{\mathrm{Re}_{D_h}} \left(1 - 1.3553\alpha + 1.9467\alpha^2 - 1.7012\alpha^3 + 0.9564\alpha^4 - 0.2537\alpha^5\right) = \frac{24\Phi}{\mathrm{Re}_{D_h}} \tag{2.8}$$

For laminar flow in rectangular ducts, Eqn. 2.3 can be rewritten using the definition of velocity and the friction factor as:

$$\Delta P = \frac{12 \Phi \mu L Q}{\rho A D_h^{\,2} N h_{fg}} \tag{2.9}$$

For flow through porous media such as sintered wicks, the pressure drop is calculated by Darcy's Law as a function of fluid viscosity (μ), fluid density (ρ), flow length (L), wick cross sectional area (A) and wick permeability (K):

$$\Delta P = \frac{\mu L v}{\mathrm{K}} = \frac{\mu L \dot{m}}{\rho A \mathrm{K}} = \frac{\mu L Q}{\rho A \mathrm{K} N h_{fg}} \tag{2.10}$$

For sintered wicks formed from unconsolidated, packed, spherical particles, the permeability can be estimated using [6]:

$$K = \frac{D^2 \varphi^3}{150\ (1-\varphi)^2} \tag{2.11}$$

The equation is a function of average particle diameter (D) and wick porosity (φ). The porosity is the ratio of pore volume to total wick volume.

The pressure drops for the entire LHP can be estimated analytically using the aforementioned equations, working fluid properties, and the current geometry. Starting with the wick interfaces, the driving pressure from the primary wick in the evaporator (ΔP_{cap}) and the capillary pressure maintaining phase separation in the condenser ($\Delta P_{cap,c}$) can both be calculated using Eqn. 2.2. For sintered wicks formed from unconsolidated, packed, spherical particles, the effective pore radius can be approximated as a function of the average particle diameter (D) by $r_{eff} = 0.21D$ [6]. For the evaporator wick, the sinter particle size ranges from 5-15 μm with an average D = 10 μm resulting in $r_{eff} = 2.1$ μm. For the condenser wick, the sinter particle size ranges from 75-100 μm with an average D = 88 μm and $r_{eff} = 18.5$ μm. For 80 °C saturated water on copper sinter, the surface tension (σ) is given in Table 2-2 and the receding contact angle ($\Theta_{receding}$) is 35° [6]. Therefore, the $\Delta P_{cap} = 48.9$ kPa and $\Delta P_{cap,c} = 5.6$ kPa.

Table 2-2 Properties of saturated water at 80 °C [24].

Liquid	Tsat (°C)	Psat (kPa)	Liquid Density (kg/m³)	Vapor Density (kg/m³)	Heat of Vapor. (kJ/kg)	Liquid Viscosity (μPa-s)	Vapor Viscosity (μPa-s)	Surface Tension (mN/m)
Water	80	47.414	971.77	0.29367	2308	354.33	11.592	62.673

When heat is input at the base of the evaporator, the working fluid evaporates at the surface of the primary wick and that vapor flows through channels in the copper base plate to the vapor pipes. As shown in Fig. 2-6, the current base plate design has 14 channels total; 7 channels (M) connected to each of the 2 vapor pipes (V). The vapor channels are approximated as ducts with a square cross section, 2 mm width (a) by 2 mm depth (b), and average length (L) of 70 mm. The hydraulic diameter (D_h) is 2 mm using Eqn. 2.4 and the aspect ratio (α) is 1. Using Eqn. 2.5, N = M*V, and the vapor viscosity (μ_v) and heat of vaporization (h_{fg}) from Table 2-2, the Reynolds number (Re) is calculated as 1335 which corresponds to laminar flow. Using Eqn. 2.8, the friction factor (f) is calculated as 0.0107 with $\Phi = 0.6$. Finally using Eqn. 2.9 and vapor properties from Table 2-2, the pressure drop ($\Delta P_{v,e}$) in the vapor channels is calculated to be 38 Pa.

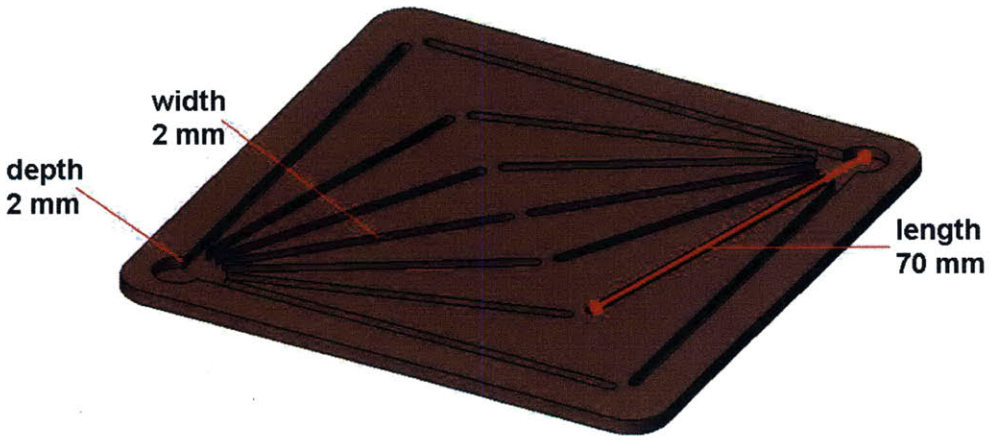

Fig. 2-6 Schematic of the evaporator copper base plate showing the 14 dimensioned vapor channels that lead to recesses for two vertical vapor pipes.

Once the vapor exits the base plate channels, it travels vertically through the 2 vapor pipes (N = V) and branches into each condenser layer. The vapor pipe is round

with a diameter D = 6 mm and a length L = 100 mm to the topmost condenser. The Reynolds number is calculated using Eqn. 2.5 as 3966 indicating that the flow is turbulent. The friction factor is calculated as 0.042 using Eqn. 2.6. Using Eqn. 2.3 and vapor properties from Table 2-2, the pressure drop ($\Delta P_{v,v}$) in the vapor pipes is calculated to be 69 Pa.

To maximize heat transfer from the condensers, the mass flow is assumed to divide evenly into each of the 15 condenser layers (C). As shown in Fig. 2-7, vapor enters the condenser from each of the 2 vapor pipes (V) and branches into 2 flow path (P) toward the outlet liquid pipes. The vapor channel has a 10 mm width (a), a 0.5 mm depth (b), a 76 mm flow length (L), an aspect ratio (α) of 0.05 and a 0.952 mm hydraulic diameter (D_h) using Eqn. 2.4. Using Eqn. 2.5, N = V*C*P, and vapor properties from Table 2-2, the Reynolds number (Re) is calculated as 119 which corresponds to laminar flow. Using Eqn. 2.8, the friction factor (f) is calculated as 0.1895 with $\Phi = 0.94$. Finally using Eqn. 2.9 and vapor properties from Table 2-2, the pressure drop ($\Delta P_{v,c}$) in the vapor channel of the condenser is calculated to be 54 Pa.

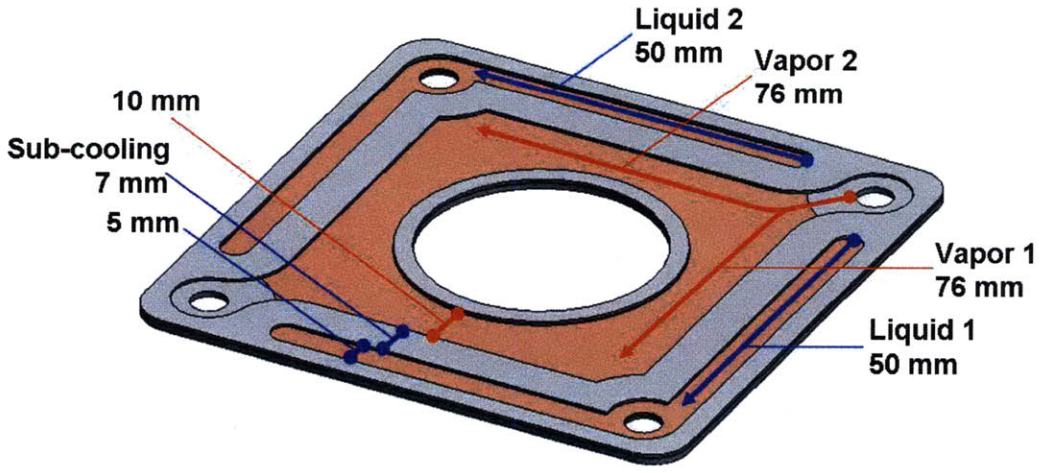

Fig. 2-7 Schematic of the condenser plate interior showing vapor flow paths (red) and liquid flow paths (blue) along with channel dimensions.

A sub-cooling length is formed by brazing a stainless steel frame to the sinter surface between the vapor and liquid channels in the condenser. Due to the air-cooling on the exterior of the condenser, the vapor condenses onto the sinter wick under the vapor channel. To reach the liquid channel, the liquid flows through 10 mm under the vapor channel and a 7 mm sub-cooling length for a 17 mm flow length (L) of sinter wick with a cross section (A) of 50 mm width (a) and 0.5 mm depth (b). The copper sinter has a particle size range from 75-100 μm with an average particle diameter (D) of 88 μm and an assumed porosity (φ) of 0.4. Using Eqn. 2.11, the sinter permeability is estimated as $K = 9.2 \times 10^{-12}$ m^2. Appling Eqn. 2.10, N = V*C*P from earlier, and liquid properties from Table 2-2, the pressure drop ($\Delta P_{l,sub}$) sub-cooling pressure drop is calculated to be 195 Pa.

Past the sub-cooling section, the liquid channel consists of a stacked sinter layer and an open channel. Because the sinter layer will have high resistance, the liquid will preferentially flow through the open channel to exit out the liquid pipes. The open channel has a 5 mm width (a), 0.5 mm depth (b) and 50 mm flow length (L). The low flow rates combined with the open geometry result in a negligible pressure drop ($\Delta P_{l,c}$) of less than 1 Pa.

The liquid flow recombines in the two liquid pipes (N=V) that connect the multiple condensers to the reservoir in the evaporator. The liquid pipes have a diameter (D) of 4 mm and a length (L) of 100 mm. The Reynolds number is calculated using Eqn. 2.5 as 195 indicating that the flow is laminar. Using Eqn. 2.7 and liquid properties from Table 2-2, the pressure drop ($\Delta P_{l,l}$) in the liquid pipes is calculated to be ~ 1 Pa.

The reservoir in the evaporator keeps the backside of the primary wick continually supplied with liquid as evaporation occurs on the opposite side. The reservoir can be approximated as an open flow channel with a 100 mm width (a), 3 mm depth (b), and 100 mm flow length (L). The low flow rates combined with the open geometry result in a negligible pressure drop ($\Delta P_{l,r}$) of less than 1 Pa.

The primary wick in the evaporator is made from layers of stainless steel and copper sinter with a particle size ranging from 5-15 μm. Assuming an average particle diameter (D) of 10 μm and a porosity (φ) of 0.4, the permeability can be calculated using Eqn. 2.11 as $K = 1.19 \times 10^{-13}\ m^2$. The liquid flows through the wick thickness such that the area (A) is 100 mm by 100 mm and the flow length (L) is 4 mm. Applying Eqn. 2.10, N=1, and liquid properties from Table 2-2, the pressure drop ($\Delta P_{l,w}$) for flow through the primary wick is 533 Pa.

The final pressure drop taken into consideration is gravity. Gravity head on columns of vapor is negligible due to the low density. However, if the 10 cm tall (L) device is oriented such that a gravity head acts in the flow direction on a column of liquid, the pressure drop can be calculated as $\Delta P_g = \rho_l g L = 953$ Pa.

The total pressure drop (ΔP_{total}) is calculated by summing all of the pressure drops within the loop heat pipe. Referencing back to Eqn. 2.1, $\Delta P_{evaporator} = \Delta P_{v,e} + \Delta P_{l,r} + \Delta P_{l,w} = 571$ Pa, $\Delta P_{vapor} = \Delta P_{v,v} = 69$ Pa, $\Delta P_{condenser} = \Delta P_{cap,c} + \Delta P_{v,c} + \Delta P_{l,sub} + \Delta P_{l,c} = 5.8$ kPa, $\Delta P_{liquid} = \Delta P_{l,l} \sim 1$ Pa, and $\Delta P_{gravity} = \Delta P_g = 953$ Pa. Therefore, $\Delta P_{total} = 7.2$ kPa which uses only 15% of the available $\Delta P_{cap} = 48.9$ kPa driving pressure with water as the working fluid. The large amount of pressure drop overhead allows for use of thinner geometries or finer sinter as required for manufacturing and LHP function.

Working Fluid Comparison

To determine whether water was the best working fluid choice, five pure fluids (water, ammonia, methanol, acetone and ethanol) were considered that would allow the heat pipe to operate at 80 °C. Water has the highest surface tension (σ) at 0.062 N/m and heat of vaporization (h_{fg}) at 2308 kJ/kg. However, water typically boils at 100 °C under atmospheric pressure, therefore the heat pipe would have to operate at vacuum conditions. The other working fluids boil at atmospheric pressure closer to the heat pipe operating temperature, but their lower heat of vaporization results in higher mass flow rates within the system. To analyze these tradeoffs, the pressure drops throughout the entire heat pipe were recalculated and compared for the different working fluids.

The detailed calculations from the previous section on the current LHP design with water were repeated, aided by a Matlab script, for the additional working fluids. The assumed properties for each fluid are given in Table 2-3 and the computed values for each pressure drop are displayed in Table 2-4. As shown in Fig. 2-8, the LHP design is not capillary pressure limited for any working fluid under consideration because $\Delta P_{cap} > \Delta P_{total}$. Any of these working fluids could be functionally incorporated into the current design. However, while water only uses 15% of the available capillary pressure, the other working fluids require 25-35%. Therefore working fluids besides water would have less margin for redesign into geometries with higher pressure drops.

Fig. 2-9 shows the breakdown of the total pressure drop into each portion of the LHP. As shown in the previous section for water, liquid flow through the open channel in the condenser, liquid pipe, and reservoir contribute negligible pressure drop. The largest pressure drops occur due to the sintered wick in the evaporator and condenser. In

the evaporator, the pressure drop ($\Delta P_{l,w}$) is due to liquid flow through the homogeneous wick with a pore size dimensioned to achieve high capillary driving pressure. In the condenser, the pressure drop is due to both capillary pressure difference at the wick surface ($\Delta P_{cap,c}$) and flow through the sinter under the sub-cooling length ($\Delta P_{l,sub}$). Water has the largest capillary pressure drop in the condenser due to its high surface tension; ethanol has the highest pressure drops for flow through sinter due to its high liquid viscosity and low heat of vaporization that results in high mass flow rates.

Table 2-3 Properties of saturated fluids at 80 °C [24]. Receding contact angles are approximate and referenced from [6].

Liquid	Tsat (°C)	Psat (Pa)	Liquid Density (kg/m³)	Vapor Density (kg/m³)	Heat of Vapor. (kJ/kg)	Liquid Viscosity (μPa-s)	Vapor Viscosity (μPa-s)	Surface Tension (mN/m)	Theta Receding (°)
Water	80	0.047414	971.77	0.29367	2308	354.33	11.592	62.673	35
Ammonia	80	4.142	505.67	33.888	873.97	77.98	11.954	9.614	35
Methanol	80	0.18111	732.58	2.1229	1069.2	274.24	11.265	17.573	25
Acetone	80	0.21548	719.79	4.6423	473.88	201.40	8.938	15.676	7
Ethanol	80	0.10857	734.64	1.7591	846.97	429.47	10.431	15.030	7

Table 2-4 Matrix comparison of pressure drops throughout the LHP for 5 different working fluids. The pressure drops are given in Pa.

	ΔPcap	ΔPtotal	ΔPcap,c	ΔPv,e	ΔPv,v	ΔPv,c	ΔPl,sub	ΔPl,c	ΔPl,l	ΔPl,r	ΔPl,w	ΔPg
Water	48894.0	7205.4	5556.1	38.0	69.1	53.6	195.1	0.7	1.3	0.0	533.2	953.3
Ammonia	7500.5	1951.4	852.3	0.9	3.2	1.3	217.9	0.8	1.4	0.0	595.5	496.1
Methanol	15168.1	3690.2	1723.7	11.0	35.0	15.6	432.4	1.5	2.8	0.0	1181.9	718.7
Acetone	14818.2	4473.6	1683.9	9.0	61.8	12.8	729.1	2.5	4.7	0.1	1992.8	706.1
Ethanol	14207.6	4772.6	1614.5	15.6	61.8	22.0	852.3	2.9	5.5	0.1	2329.5	720.7

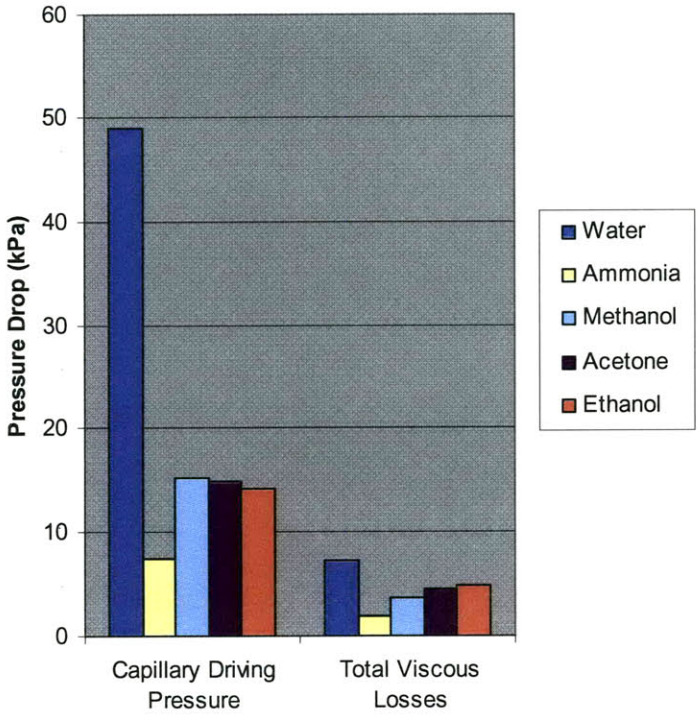

Fig. 2-8 Bar graph showing comparison of capillary driving pressure to the total viscous (and gravity) losses within the LHP for 5 different working fluids. Although ΔP_{cap} exceeds ΔP_{total} in all cases, water has the largest margin.

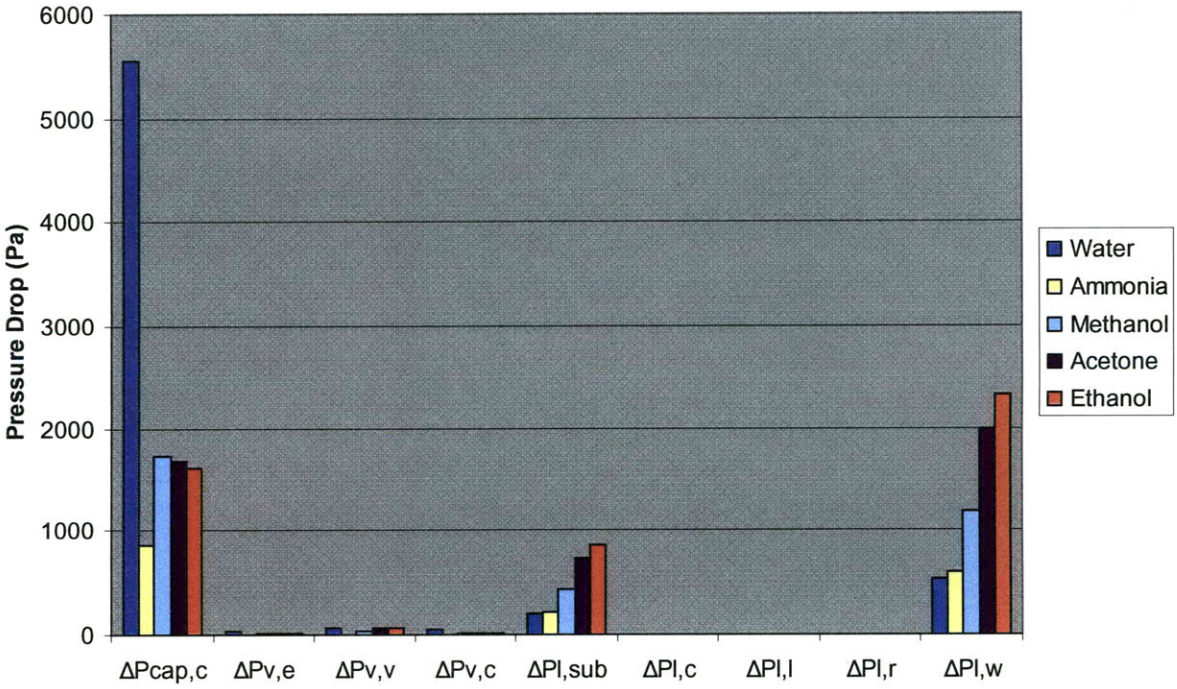

Fig. 2-9 Bar graphing showing individual pressure drops comprising ΔP_{total} for 5 different working fluids. In all cases, flow through sinter in the sub-cooling length ($\Delta P_{l,sub}$) and the primary wick ($\Delta P_{l,w}$) and the capillary interface in the condenser ($\Delta P_{cap,c}$) contribute the largest pressure drops.

Sintered Wick vs. Open Channel in Condenser

The calculations thus far have proven that the capillary driving pressure exceeds the pressure drops due to the addition of sinter in the condensers. This section will investigate whether that sinter is needed for flow stability of the parallel condensers. As stated in the design section, sinter was incorporated into the condensers to create a stable separation of phases. When gravity acts in the same direction as flow through the liquid pipe, a pressure rise is created between the top and bottom condensers. If the gravity head sets a pressure exceeding the pressure drop within the layer, the bottom condenser will experience high pressure at the outlet and low pressure at the inlet causing flow reversal and flooding of the layer.

To better understand the role of sinter, the current LHP design was compared to a design with an open channel condenser, shown in Fig. 2-10. In each of the 15 layers (C), vapor enters from the 2 vapor pipes (V), branches into 2 flow paths (P) and condenses as during flow to the liquid pipes. For these calculations, the two-phase flow is approximated as separate vapor and liquid flows, each for half the flow length, and a capillary interface between the phases. The open channel has a 20 mm width (a), 1.5 mm depth (b), 76 mm total flow length (L), 2.8 mm hydraulic diameter (D_h), and aspect ratio of 0.075. The flow is assumed to be laminar for both phases due to the slow flow rates and open geometry in each layer. Applying Eqn. 2.9 and vapor properties from Table 2.2, the pressure drop due to vapor flow ($\Delta P_{v,c}$) is ~ 0.5 Pa. Applying Eqn. 2.9 and liquid properties from Table 2.2, the pressure drop due to liquid flow ($\Delta P_{l,c}$) is << 1 Pa. Finally, using Eqn. 2.2, the capillary pressure drop ($\Delta P_{cap,c}$) at the liquid-vapor interface is 68 Pa

assuming a receding contact angle ($\Theta_{receding}$) of 35° and an effective radius (r_{eff}) equal to the 1.5 mm channel depth.

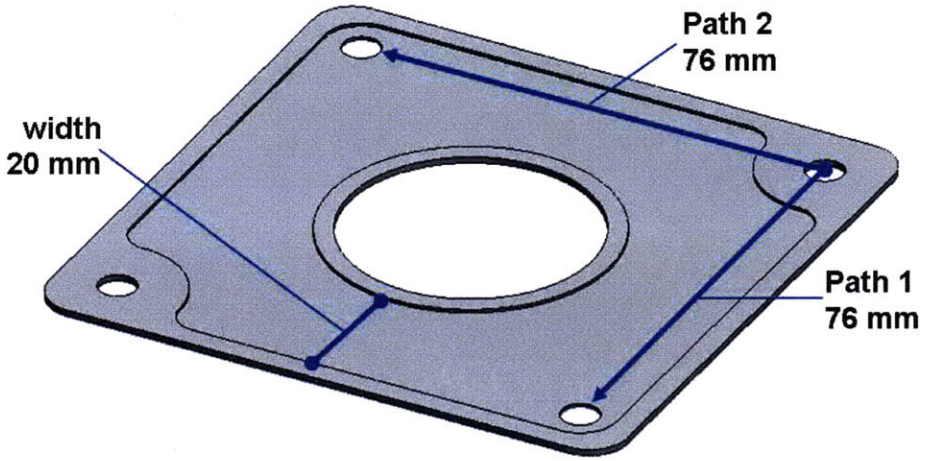

Fig. 2-10 Schematic of open channel condenser showing flow paths and dimensions.

The absolute pressure can be mapped for each design given a known starting pressure and the pressure drops within each segment of the loop. The starting pressure at the evaporation interface of the primary wick is assumed to be the 47.4 kPa saturation condition (P_{sat}) for water at 80 °C. To form the graph in Fig. 2-11, pressures are calculated at each point P_1 thru P_4 by subtracting pressure drops over that portion of the LHP from the absolute pressure and these points are connected with a smooth fit curve. To graph the blue vapor curve from left to right, the following equations are used along with the pressure drops for water in Table 2-4:

$$P_{1,vapor} = P_{sat}$$
$$P_{2,vapor} = P_{1,vapor} - \Delta P_{v,e}$$
$$P_{3,vapor} = P_{2,vapor} - \Delta P_{v,v}$$
$$P_{4,vapor} = P_{3,vapor} - \Delta P_{v,c}$$

To graph the pink liquid curves from right to left, the following equations are used along with the pressure drops for water in Table 2-4 and the open channel calculations from above:

$$P_{4,liquid} = P_{4,vapor} - \Delta P_{cap,c}$$

$$P_{3,liquid} = P_{4,liquid} - \Delta P_{l,sub} - \Delta P_{l,c} \text{ (sinter)} \qquad P_{3,liquid} = P_{4,liquid} - \Delta P_{l,c} \text{ (open)}$$

$$P_{2,liquid} = P_{3,liquid} - \Delta P_{l,l} + \Delta P_g \text{ (gravity)} \qquad P_{2,liquid} = P_{3,liquid} - \Delta P_{l,l} \text{ (no gravity)}$$

$$P_{1,liquid} = P_{2,liquid} - \Delta P_{l,r} - \Delta P_{l,w}$$

The graph in Fig. 2-11 shows that the largest pressure drops due to gravity (ΔP_g) and the capillary interface in the condenser ($\Delta P_{cap,c}$) heavily influence the pressure profile inside the LHP. The blue vapor curve is fairly flat because the pressure drops due to vapor flow never exceed 160 Pa. The solid pink curve for the current LHP design with sinter but neglecting the influence of gravity shows a substantial pressure jump across the condenser wick interface and then a gently decreasing pressure from right to left due primarily to viscous drops from flow through the two sinter wicks. In contrast when gravity head is applied to the liquid pipe, the design with sinter and the open channel (no sinter) both experience a pressure rise between P_3 and P_2. In the open channel, that pressure rise causes the liquid pressures (pink dotted line) to cross above the vapor pressures. The flow in the lower condensers will go from the high pressure liquid to the lower pressure vapor causing flooding of the condenser layer. However, in the case of the design with sinter, the capillary pressure drop substantially reduces the liquid pressures such that the gravity rise will increase pressure but maintain the correct circulation inside the LHP.

These results indicate that a pressure drop exceeding the gravitational pressure rise is required within the condenser and liquid pipe to prevent flooding of the lower parallel layers. Within the current LHP design, the sinter interface in the condenser creates a large enough pressure drop to ensure stable circulation of the working fluid through all layers.

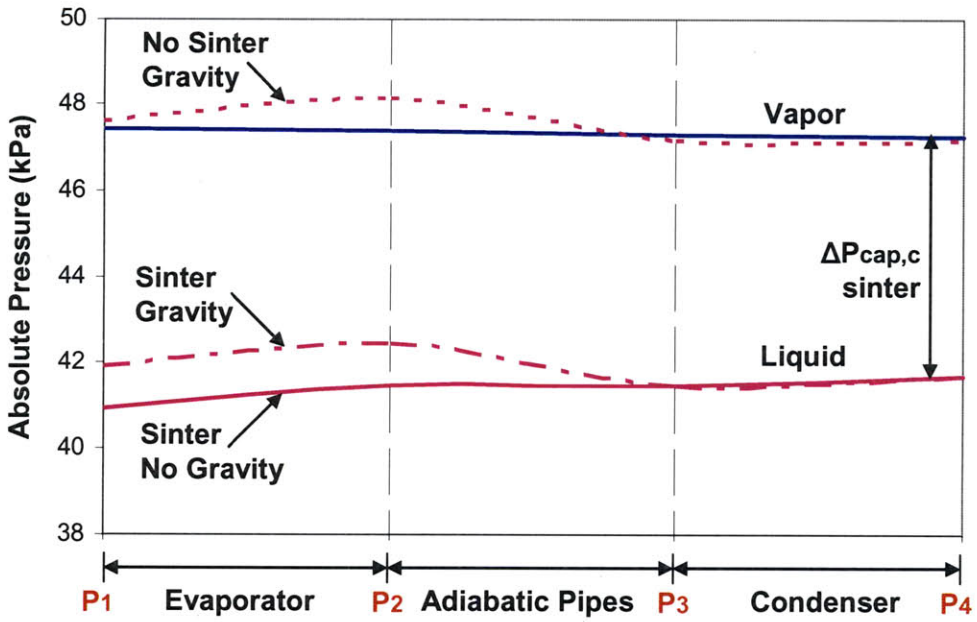

Fig. 2-11 Graph showing absolute pressure versus location in the heat pipe. The open channel (no sinter) case will experience flooding because the liquid pressure is higher than the vapor pressure. In contrast, the capillary interface at the sinter surface creates a large enough pressure drop to prevent cross-over of the liquid and vapor pressures.

Mass Flow Balance

The previous section determined that a pressure drop exceeding the gravitational head is needed to prevent flooding of the lower condensers. That pressure drop can occur interchangeably within the condenser or the liquid pipe to satisfy the stable flow criteria. This section will investigate whether the location of that pressure drop affects mass flow balance between each of the parallel condensers. As stated in the design section, the open geometry of the vapor channel and liquid pipe and the high pressure drop geometry of the capillary interface and sub-cooling section are all intended to ensure equal mass flow in each condenser layer.

A Matlab model was developed to explore the sensitivity of mass flow distribution to magnitudes and locations of pressure drops within the vertical pipes and condenser layers. The code for this Matlab model is provided in Appendix A. As shown

in Fig. 2-12, the model represents the heat pipe as a network of resistors and capacitors. Given an input total amount of mass flow along with known flow resistances and constant pressure effects, the model solves for mass flow through each parallel condenser and pressure drop for this portion of the heat pipe. The resistances represent viscous losses in the system due to vapor or liquid flow. The capacitors represent pressure drops due to capillary interfaces and pressure rises due to gravity head. Assuming laminar flow throughout the system, the resistances are defined in the following manner:

Flow through circular pipe $$R = \frac{128\mu L}{\rho \pi D^4} \tag{2.12}$$

Flow through rectangular duct $$R = \frac{12\Phi\mu L}{\rho A D_h^{\,2}} \tag{2.13}$$

Flow through sinter wick $$R = \frac{\mu L}{\rho A K} \tag{2.14}$$

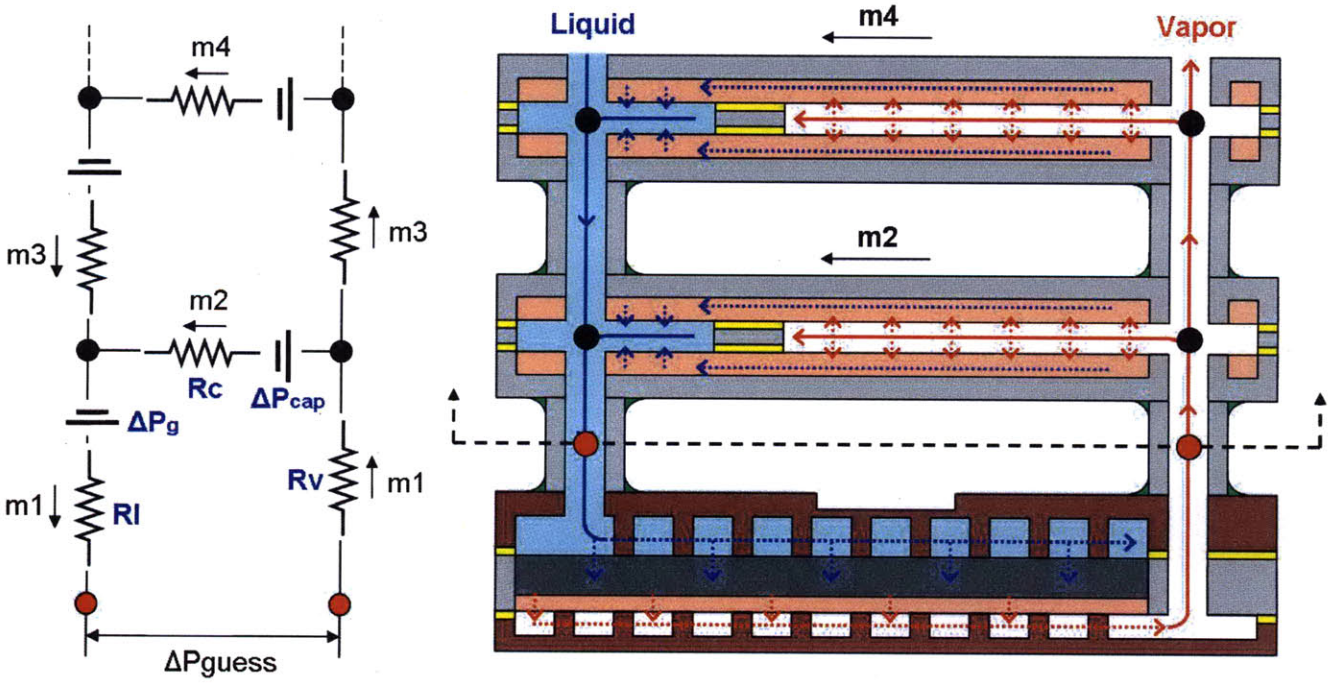

Fig. 2-12 Schematic of resistor and capacitor network used to model the parallel condenser plates and vertical fluid lines.

The total flow resistance through the vapor pipe (Rv_{total}) is calculated using Eqn. 2.12 and the water vapor properties given in Table 2-2. Both open and sinter filled liquid pipes are explored with this model, therefore either Eqn. 2.12 or Eqn. 2.14 is used along with the liquid properties in Table 2-2 to calculate total flow resistance through the liquid pipe (Rl_{total}). Both Rv_{total} and Rl_{total} are calculated for the full 100 mm pipe length. The resistance for flow through each segment connecting the "n" number of parallel condensers is therefore $Rv = Rv_{total} / n$ and $Rl = Rl_{total} / n$. In essence, the model assumes that the LHP will take up the full 100 mm allocated height regardless of the number of condensers. The total flow resistance of the condenser (Rc) is calculated by summing the resistance from flow through the vapor space using Eqn. 2.13 and liquid flow through the sinter wick using Eqn. 2.14. The total pressure drop due to gravity is always 968 Pa assuming a 100 mm gravity head, therefore the gravity head applied to each segment connecting the "n" number of parallel condensers is $\Delta Pg = 968 / n$. Finally, the capillary pressure at the condenser wick interface ($\Delta Pcap$) is assumed to be constant and equal in every condenser layer and is calculated using Eqn. 2.2 for the sinter composition.

Given a known input mass flow (m1) and an initial estimate of total pressure drop (ΔP_{guess}), the model solves for the mass flow in every segment of the loop and pressure at every branching node. Mass flow must be conserved at every node within the system e.g. $m1 = m2 + m3$. In the top most layer of the condenser stack, the mass flow through the condenser equals the mass flow in the liquid and vapor pipes. For example, if the maximum number of condensers is 2 as shown in Fig 2-13(a), $m3 = m4$. Within the parallel condenser structure, every flow path must result in the same ultimate pressure

drop (ΔP_{guess}) across the network. As shown in Fig. 2-13(a), the following equations must be equal:

Path 1 $$\Delta P_{guess} = m1(Rv + Rl) + m2(Rc) + \Delta P_{cap} - \Delta P_g \quad (2.15)$$

Path 2 $$\Delta P_{guess} = (m1 + m3)(Rv + Rl) + m4(Rc) + \Delta P_{cap} - 2(\Delta P_g) \quad (2.16)$$

Of course, the number of equations will increase directly with the number of condensers. The actual solving scheme is modeled after the loops shown in Fig. 2-13(b). Loop 1 is represented by Eqn. 2.15. Loop 2 is represented by:

$$m3(Rv + Rl) + (m4 - m2)(Rc) = \Delta P_g \quad (2.17)$$

For any Loop n within the network, Eqn. 2.17 can be written more generally as:

$$m_{2n-1}(Rv + Rl) + (m_{2n} - m_{2n-2})(Rc) = \Delta P_g \quad (2.18)$$

The model iterates the value of ΔP_{guess} until the system of equations for conserved mass flow and loop pressure drop are satisfied. The model solves for mass flow within each segment of the network for n = 2 to 18 condensers and pressure drop for the entire flow loop.

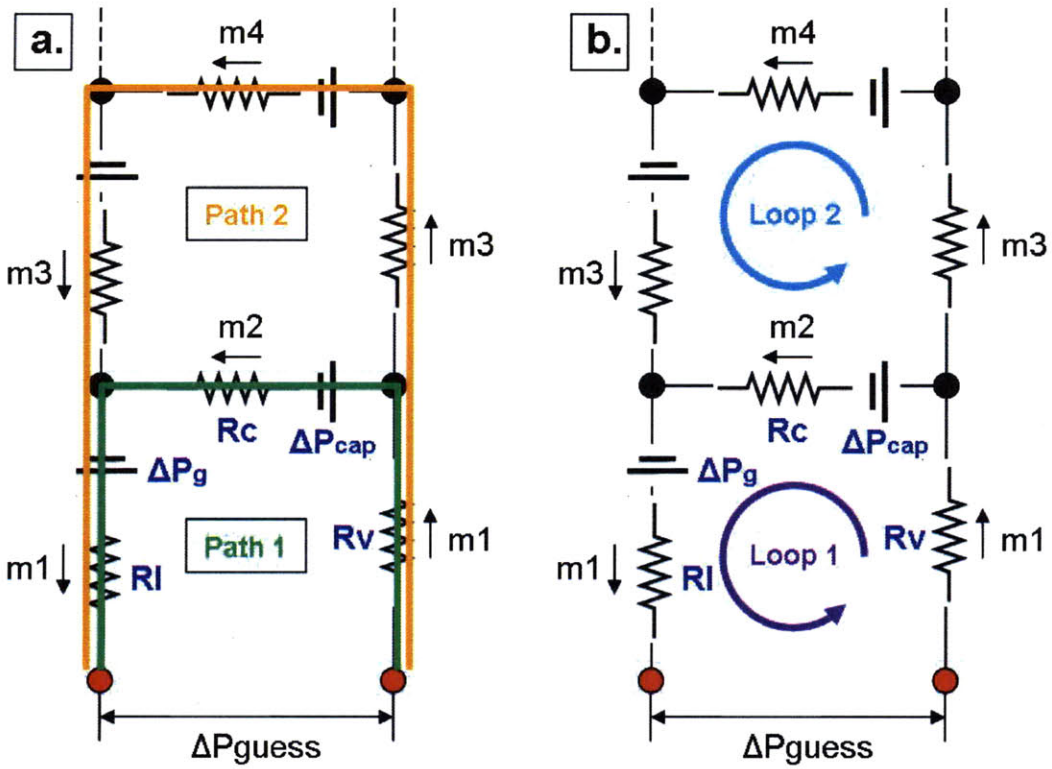

Fig. 2-13 Schematic of resistor network illustrating methods of solving within the Matlab code. (a) Flow paths beginning and ending at the same points must have the same pressure drop. Additionally, mass flow is conserved at every node. (b) Given an initial guess of pressure drop and input mass flow, the code solves each loop and iterates ΔP_{guess} until constraints in (a) are satisfied.

The following calculations were performed for an earlier iteration of the loop heat pipe design. That iteration had sinter in the condenser and liquid pipe, no sub-cooling length, and assumed 100 mm length of liquid flow through the wick between condensation and the outlet port. Although the geometries are different, the conclusions from this model helped guide the current design and therefore the modeling results are shown here. The model under initial evaluation had the following conditions, with high resistance in both the condenser layer and the liquid pipe:

Rv	1.2594×10^5
Rc	2.0632×10^8
Rl	1.3102×10^8
ΔPcap	2177
ΔPg	969

As shown in the graph in Fig. 2-14, this geometry experiences high mass flow through the lowest condenser layers and low mass flow through the higher layers. This indicates that a large viscous pressure drop is required through the bottom condenser to balance pressure drops through the vertical pipes. The capillary pressure (ΔPcap) was varied from 0 to 50,000 with all other parameters held constant. Although the total pressure drop increased, the mass flow subdivided in the same manner as shown in Fig. 2-14. Therefore, while the capillary pressure was shown to prevent flooding in the previous analysis, this study suggests that only viscous flow resistances affect flow distribution.

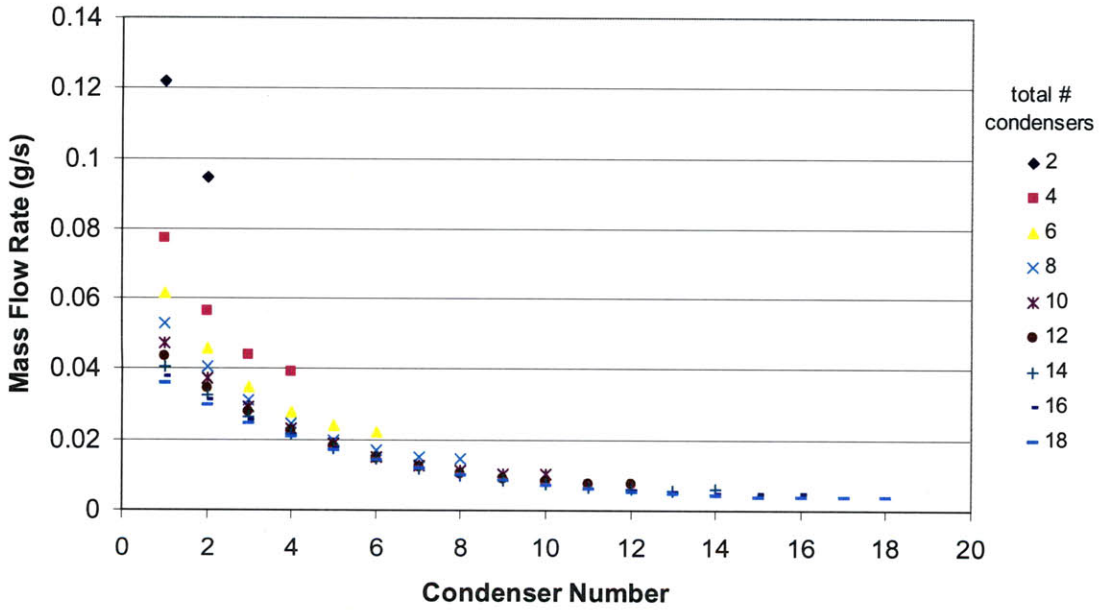

Fig. 2-14 Graph of mass flow rate within each condenser layer. Data shows trends of high mass flow through bottom condensers and low mass flow through high level ones.

To study the effect of the viscous resistance location, another version of the model was solved with a reduction in condenser resistance by one order of magnitude such that $Rc = 2.0632 \times 10^7$ and all other parameters held the same. As shown in Fig. 2-15, the data again shows unbalanced flow rates within the condensers. Compared to Fig. 2-14,

this data shows an even steeper drop off in mass flow suggesting that high liquid pipe resistance with low condenser resistance will always result in unbalanced flow.

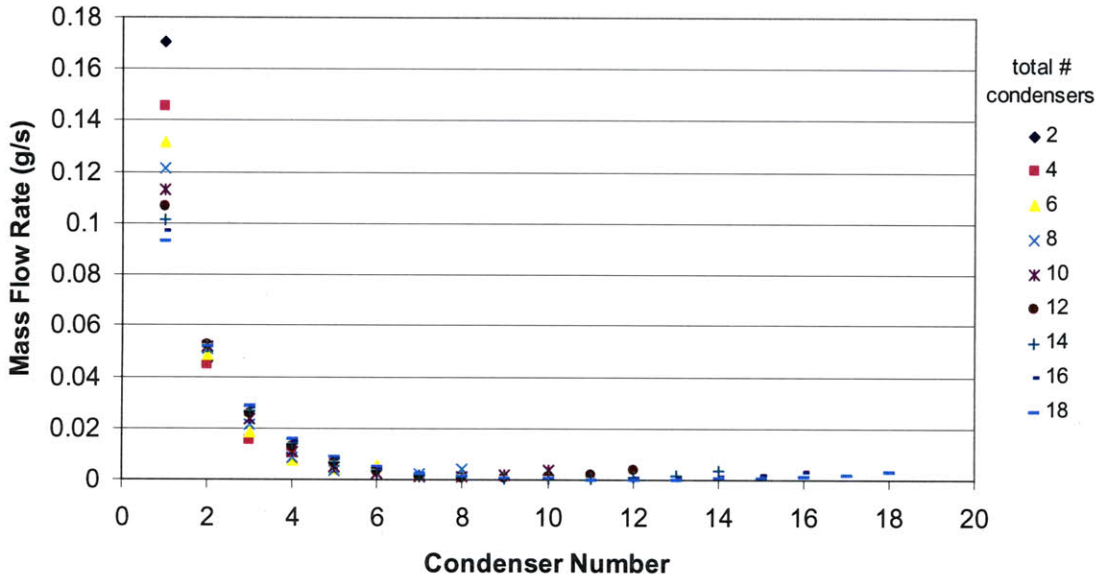

Fig. 2-15 Graph of mass flow rate within each condenser for reduced condenser resistance.

To test the reverse scenario, this time the liquid pipe resistance was reduced by one order of magnitude to Rl = 1.3102 x 10^7 with all other parameters held constant from the initial model. As shown in Fig. 2-16, the mass flow per condenser forms approximately a horizontal line indicating that flow is balanced. These results suggest that high condenser flow resistance with low liquid pipe resistance creates even mass flow. To further investigate this conclusion, the liquid pipe resistance was further reduced by 4 orders of magnitude to Rl = 1.3102 x 10^3. As shown in Fig. 2-17, the data still shows a slightly increasing, but still horizontal trend supporting a design with very low liquid pipe resistance, which can be achieved using open pipe geometry.

In conclusion, the Matlab model showed that high flow resistance in the condenser combined with low resistance in the liquid pipe resulted in balance flow

between the condenser layers. These results support the use of sinter and a sub-cooling length in the condensers to create a high pressure drop flow restriction.

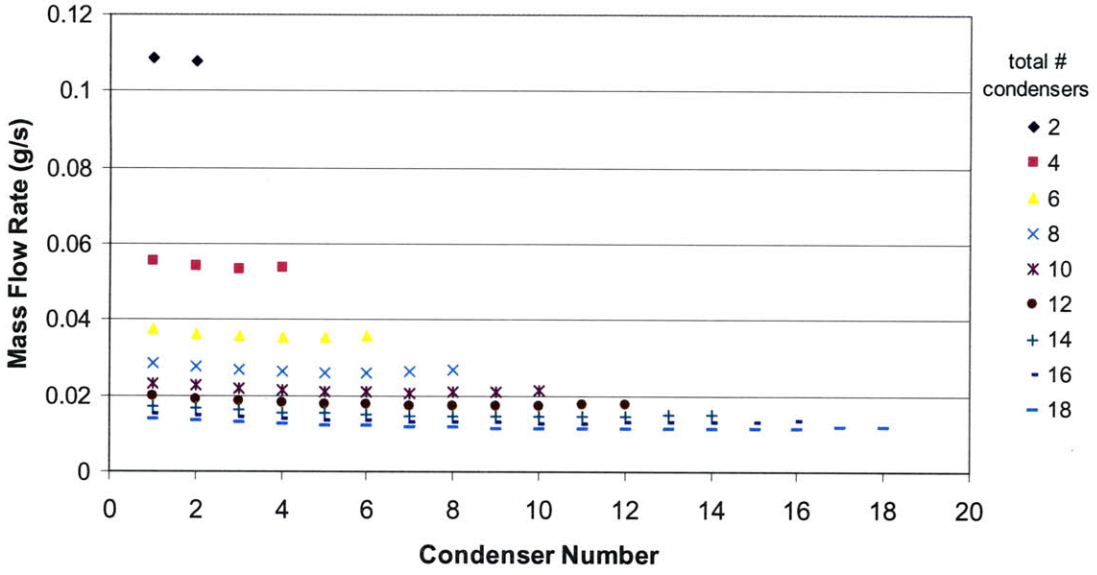

Fig. 2-16 Graph of mass flow rate within each condenser for reduced liquid pipe resistance. Data for each number of condensers is almost horizontal suggesting that flow is balanced between the layers.

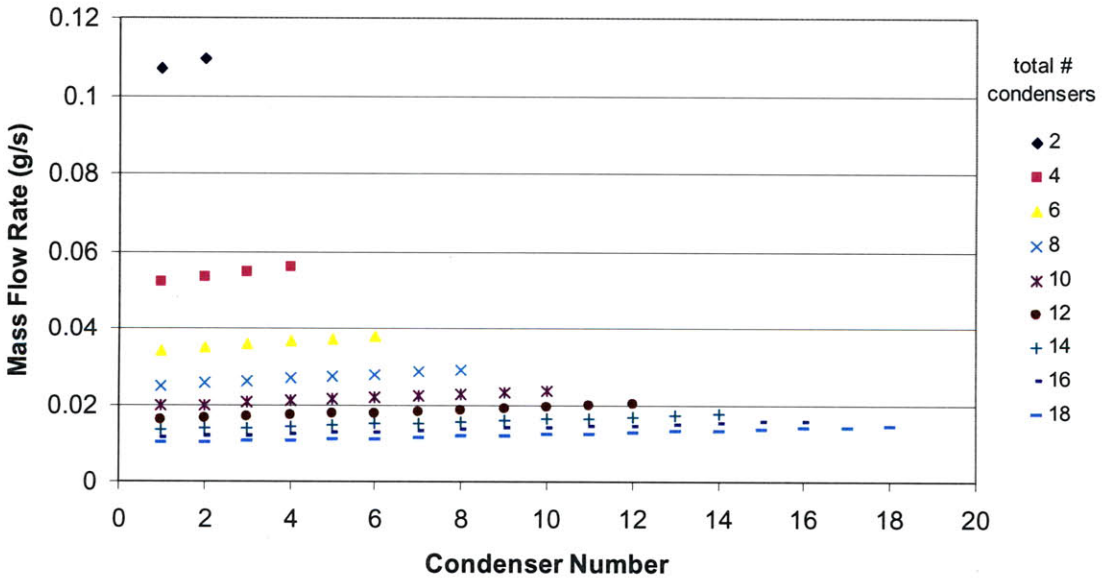

Fig. 2-17 Graph of mass flow rate within each condenser for very low liquid pipe resistance. Data suggests that even open geometry liquid pipe could be used in design.

Chapter 3: Working Fluid Deaeration

Overview

Within the heat pipe evaporator, gases dissolved in the working fluid are released during phase change to vapor. These gases travel with the vapor to the condensers where they accumulate, effectively blocking off area from vapor condensation. Three different methods of deaeration were investigated as a means of removing dissolved non-condensables from the water prior to use as the working fluid in a condensing flow test setup or the heat pipe design. Vacuum degassing, helium sparging, and freeze-pump-thaw cycles were performed on containers of DI water and their results were qualitatively validated via condensing flow experimental testing. The freeze-pump-thaw method turned out to be the most effective at removing non-condensable gases owing to the small container volume, ability to pull down to low vacuum, and direct use as the vapor generation tank in the experimental setup.

Vacuum Degassing

Concept

Vacuum degassing is a technique where vacuum pumping is used on a tank of liquid to remove dissolved non-condensable gases. Fig. 3-1 shows the solubility of O_2 and N_2, the main components of air, in room temperature water as a function of pressure. The vacuum pump removes gases in the vapor space above the water that is being degassed. The saturation pressure of water at 25 °C is 0.031 atm [24], so initially the gas that is removed is mostly air. At atmospheric pressure, 0.009 g of O_2 and 0.011 g of N_2 are soluble in one liter of water. As the pressure above the water is decreased by the

vacuum pump, the amount of O_2 and N_2 soluble in the water decreases, so O_2 and N_2 must come out of solution. The O_2 and N_2 diffuse to the water surface where the dissolved gas concentration is the lowest and the gases are then removed by the vacuum pump. As the pressure approaches 0.031 atm (saturation pressure of water at 25 °C), the solubility of both N_2 and O_2 decrease below 0.001 g/L and water vaporization increases.

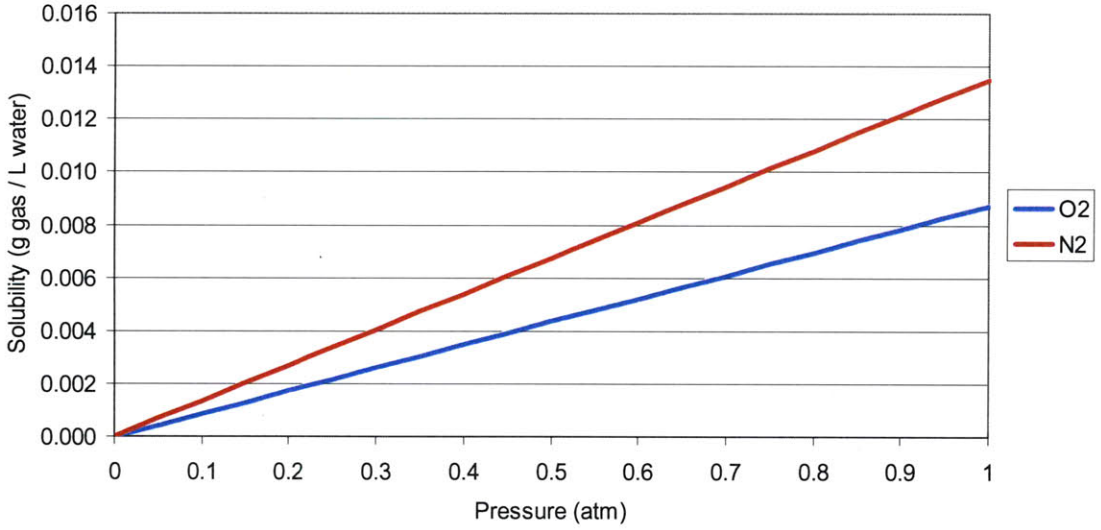

Fig. 3-1 Graph of solubility of oxygen and nitrogen in room temperature water as a function of pressure. Based on Henry's Law, solubility decreases with decreasing pressure. The Henry's law constants used for this plot were 769.23 L.atm/mol for O_2 and 1639.34 L.atm/mol for N_2 [17].

Equipment

The water used in the deaeration is ACS Reagent Grade, ASTM Type I deionized, double distilled water (RC91501, Ricca Chemical). Approximately 2.5 gallons of water are poured directly into a 3 gallon capacity, stainless steel pressure vessel (41705K42, McMaster) that acts as the vapor generation tank in the experimental setup. A schematic of the setup for vacuum degassing is shown in Fig. 3-2. The tank is connected to a port with a ball valve via 12" of ¼" diameter stainless steel tubing. The vacuum pump and a liquid nitrogen trap are then attached to the port with ½" diameter flexible plastic tubing.

The vacuum pump used for degassing is a two-stage, belt-driven high vacuum pump (1402, Welch) capable of an ultimate pressure of 0.1 mTorr as shown on the performance curve in Fig. 3-3. The liquid nitrogen trap (CG-4515, Chemglass) is located upstream of the pump with its body immersed in a dewar of liquid nitrogen to prevent vapor from reaching the vacuum pump. A thermocouple vacuum sensor (DV-6M, Teledyne Hastings) with a 1 – 1000 μHg range analog vacuum gauge (VT-6A, Teledyne Hastings) is located between the trap and the vacuum pump. This placement of the vacuum pressure sensor prevents water damage to the sensor, but it should be noted that the sensor measures the pressure with the condensable vapors removed by the nitrogen trap, which is a lower pressure than the actual pressure in the water tank.

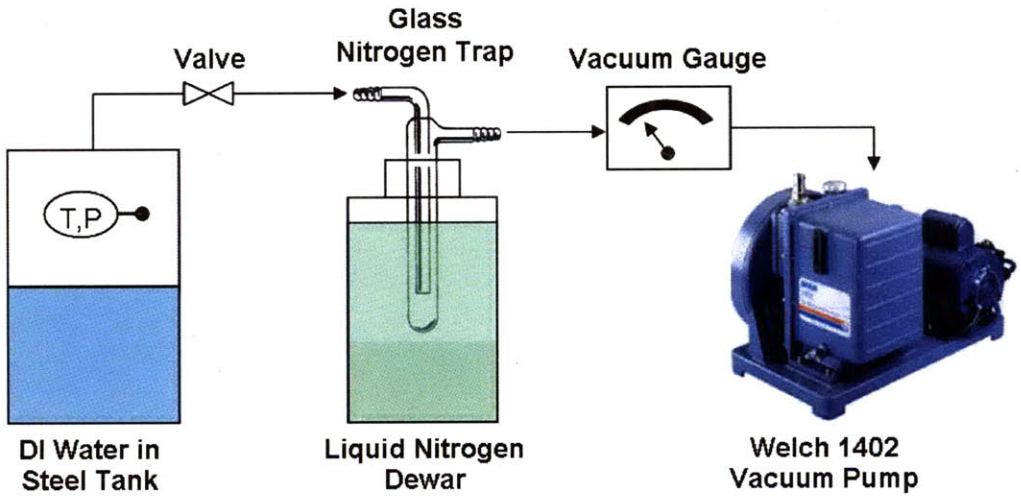

Fig. 3-2 Schematic of the experimental setup for vacuum degassing.

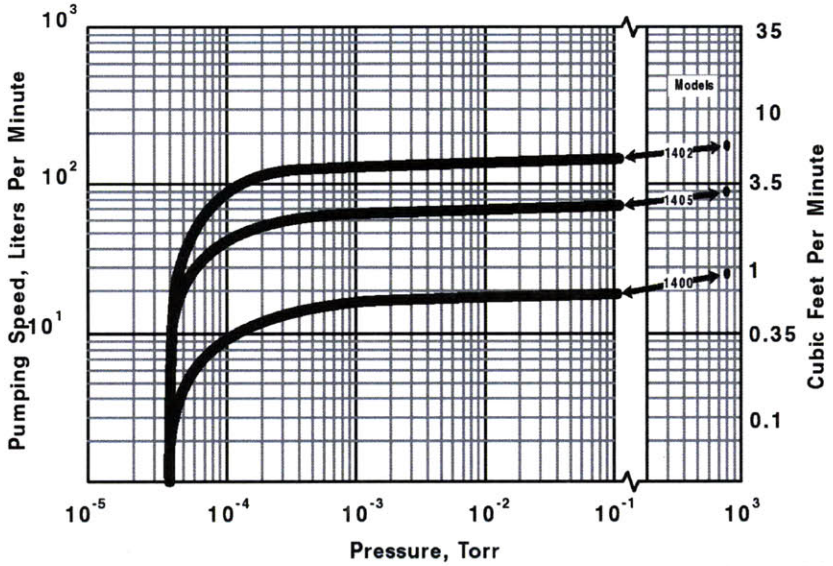

Fig. 3-3 Pump performance curve for Welch 1402 vacuum pump with an ultimate pressure of 0.1 mTorr and a maximum pumping speed of 5.6 cfm (mTorr = μHg) [19].

Procedure

Once the tank is filled with 2.5 gallons of water, the mouth is sealed with a vacuum cap. With the ball valve closed and the nitrogen trap in ambient air, the vacuum pump is started. The oil needs to warm up and air in the plastic lines needs to be evacuated prior to placing the trap into the full nitrogen dewar. After a few minutes, the trap can be inserted into the dewar and the ball valve opened. Initially the vacuum gauge will read between 1000 μHg and ambient pressure, but over time the value will decrease. It has been found that after pumping for 40 hours the gage pressure measurement no longer changes therefore vacuum was pulled on the tank for a minimum of this amount of time. After the time has elapsed, the valve is shut and the vacuum pump disconnected from the system so that tank can be used as a vapor source in the experimental setup.

Throughout each day, the nitrogen trap should be checked hourly to ensure that the inlet is not frozen shut. The vacuum pumping causes water in the tank to vaporize and that vapor often freezes immediately upon entering the nitrogen trap. If the buildup

of ice forms at the inlet, this blockage is often indicated by the vacuum gauge reading a falsely low valve. To remove the trap, the ball valve should be shut and the plastic line downstream of the trap pinched closed so that the pump can continue running. It is suggested to have multiple traps on hand so that another dry trap can be swapped into the line while the frozen trap thaws at room temperature. Rapid thawing under tap water often causes shattering of the glass trap due to cracking of the ice inside.

To test the level of non-condensables remaining after vacuum degassing, the water is vaporized by a band heater on the tank and then condensed in a test section that allows for viewing of the flow. As shown in Fig. 3-4, a large non-condensable gas bubble forms in the test section where the vaporized water is re-condensed. This indicates that even after multiple days of vacuum degassing, a large amount of non-condensable gas is still dissolved in the water in the 3 gallon stainless steel pressure vessel. It is hypothesized that volume of water is just too large to be degassed in an efficient manner by this method. Additionally, an ideal container would have a large surface area and a short height instead of the container used in this testing that had a 9" diameter and a 15" height.

Fig. 3-4 Image of condensing flow after vacuum degassing in an open channel. Vapor enters from the left, condenses due to liquid cooling on the backside and exits as liquid on the right. The elongated bubble extending across much of the flow channel is non-condensable gas.

Helium Sparging

Concept

Helium sparging is a degassing technique where helium is bubbled through a liquid reservoir to displace dissolved gases. These gases are absorbed into the helium bubbles and then carried to the surface by buoyancy. As shown in Fig. 3-5, helium has a much lower solubility in water than air. Even though some helium may dissolve into the water, it will only be a small fraction of the helium bubbled though in the sparging process. By vacuum pumping during or immediately after sparging, the remaining helium can be removed from solution.

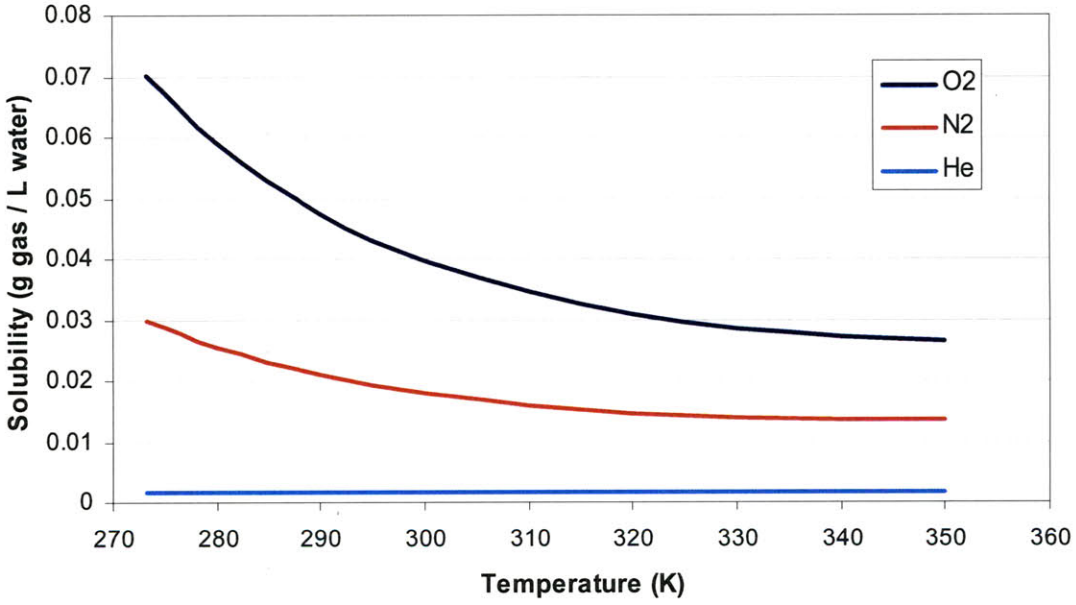

Fig. 3-5 Comparison of the solubility of oxygen, nitrogen and helium in water at one atmosphere (101.325 kPa) as a function of temperature [20].

Equipment

The water degassed by helium sparging is ACS Reagent Grade, ASTM Type I deionized, double distilled water (RC91501, Ricca Chemical). The sparging equipment, shown in the schematic in Fig. 3-6 and the photograph in Fig. 3-7, includes a vacuum

pump, a liquid nitrogen dewar, a helium cylinder, and a 3 inch diameter, 3 foot tall polycarbonate column with aluminum end caps. The o-rings recessed into the end caps form a face seal when compressed onto the ends of the column. This compression is accomplished by tightening nuts on the two vertical steel threaded rods. The end cap has a ¼" NPT threaded hole for a bourdon tube dial vacuum gauge reading from 0-30 inches of Hg. The cap also has a bored-through, Ultra-Torr vacuum fitting (SS-4-UT-1-4, Swagelok) that allows for vertical height adjustment of a ¼" diameter stainless steel tube extending into the column. One end of the tube is threaded to fit a 40 μm porous bronze sparging head (8226T11, McMaster) and the other end is connected by Swagelok fittings to flexible PFA tubing. The tubing can be lowered into a water container for filling of the column or connected to the helium tank to sparge the liquid. The end cap also has a vacuum-rated valve with ½" diameter flexible hosing that connects the column to the vacuum pump. Upstream of the pump, the hose connects to a glass vacuum trap (CG-4515, Chemglass) with its body immersed in a dewar of liquid nitrogen to prevent vapor from reaching the vacuum pump.

A Teflon-coated magnetic stirring rod is placed inside the column before the ends are sealed. Once assembled, the entire column is placed on a hot plate stirrer and held upright using a support stand and a three-prong clamp.

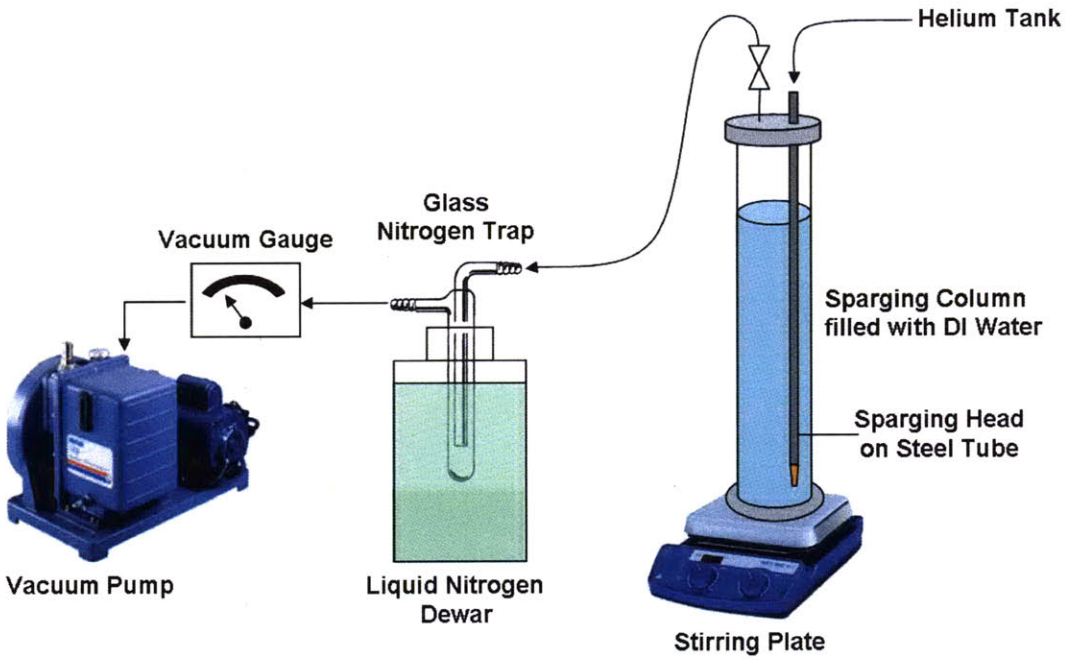

Fig. 3-6 Schematic of the experimental setup for helium sparging.

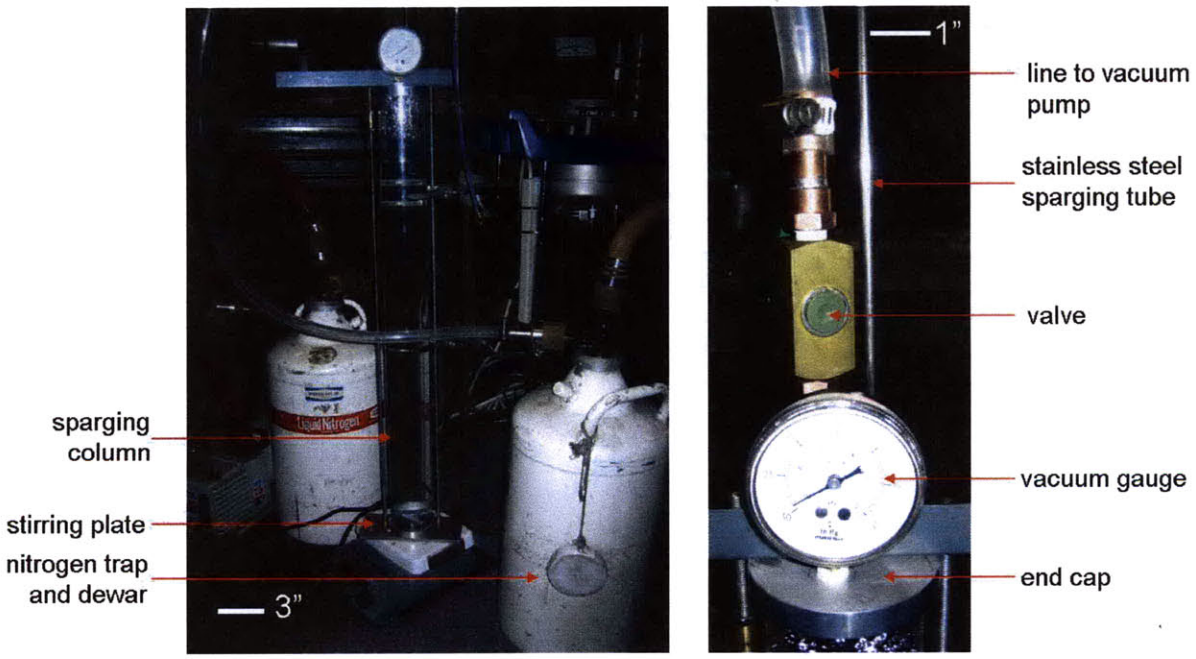

Fig. 3-7 Experimental apparatus used for helium sparging of DI water.

Procedure

To remove any contaminants prior to sparging, the polycarbonate column is cleaned with isopropanol, rinsed with DI water, and dried with kim wipes. The

aluminum end caps are cleaned with acetone, the o-rings are coated with vacuum grease, and then the stirring rod is sealed inside the column. Once the assembly is mounted on the hot plate and the lines are connected, the next step is to fill the column with DI water straight from the original container. The steel rod is raised until the sparging head is located 3 inches below the top end cap and the Ultra-Torr fitting is tightened to ensure a vacuum seal. The loose end of the PFA tubing is immersed in the container of DI water. The pump is then turned on and, as it pulls down to vacuum pressure, liquid is pulled into the column from the container. The column is filled with 2 liters of water, allowing for open space at the top to prevent the vacuum line from pulling out liquid. The PFA tube is capped, the steel rod is lowered slightly below the surface of the water, and the pump is allowed to pull vacuum for an hour. Over that time, bubbles of air will come out of solution and increase in diameter as they rise by buoyancy in the 3 foot column. The diameter increase leads to violent eruptions at the water surface. The vacuum pumping is continued until these eruptions calm and the bubbles appear stagnant.

To begin sparging, the PFA tube is connected to the helium tank and the stirring rod is activated. The speed of the stirring rod is increased until the water surface exhibits a whirlpool shape indicative of the entire column of liquid being rotated. The helium tank is opened and the flow slowly increased until frequent small bubbles appear from the sparging head. The steel rod is then lowered to the bottom of the column, leaving enough room for the stirring rod to rotate freely. As shown in Fig. 3-8, the helium bubbles will rise to the surface by buoyancy in a helical path following the rotation of the stirred liquid. Helium sparging is continued for 30 minutes while the pump pulls vacuum on the column. After that time, the helium tank is closed, the PFA line is disconnected, and

pumping is allowed to continue on the column for an additional 30 minutes to remove any remaining helium. The vacuum-rated valve on the column is then closed, the stirring rod is turned off, and the tubing connecting to the vacuum pump is detached. If the pump will be used again for another degassing, the line connecting the trap and the column should be pinched so that the pump can remain running without pulling in air. If all degassing is complete, the pump should be shut off and the nitrogen trap disconnected and allowed to thaw at room temperature. Rapid thawing by placing the trap under running tap water frequently leads to cracking of the glass body.

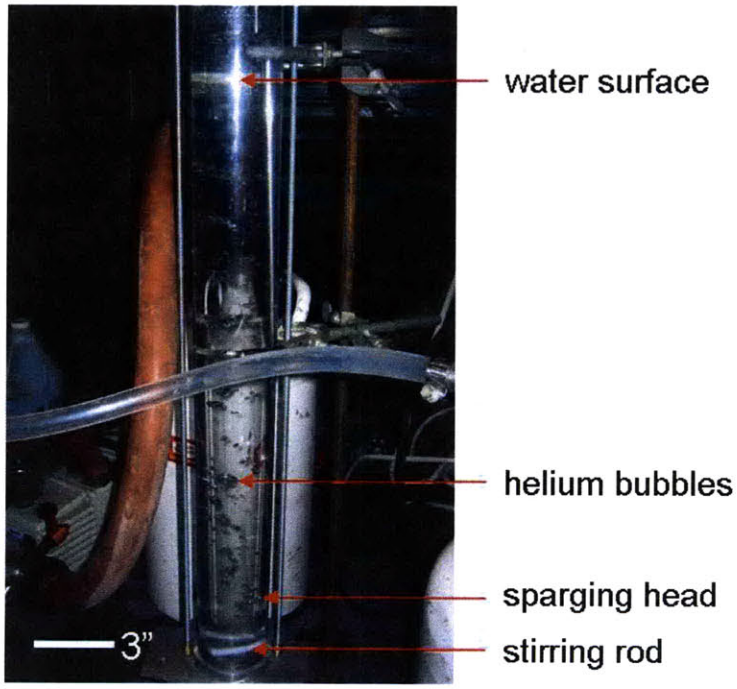

Fig. 3-8 Image of helium bubbling through a column of DI water during sparging. Due to the decrease in pressure and the accumulation of air, the helium bubbles will increase in diameter as they rise to the top surface of the liquid.

The next step is to transfer the degassed water into the vapor generation tank in the experimental setup. The helium tank is connected via plastic tubing to the vacuum-rated valve and the PFA tubing is connected to a Swagelok port on the vapor tank. Once the valve is opened, the helium is used to pressurize the surface of the liquid column and

force the water to flow out through the sparging head, steel rod, and PFA tubing into the vapor tank. The liquid transfer is continued until the water level is slightly higher than the sparging head. The valve is then closed and the PFA tubing disconnected from the vapor tank. To fill the vapor generation tank, helium sparging must be repeated 5 times for a total liquid volume of 10 L.

A dissolved oxygen probe (DO-BTA, Vernier) with a range of 0-14 mg/L is used to quantify the change in dissolved air content before and after helium sparging. As shown in Fig. 3-9, the sensor measures the current flowing between the anode and cathode which is proportional to the oxygen diffusing across the membrane at the tip of the sensor. As a baseline, the oxygen content of DI water directly from the VWR container was measured to be approximately 8.6 mg/L as seen in Fig. 3-10. After transferring the degassed liquid into the vapor tank, a small portion of the remaining liquid in the column is transferred into an open-top glass beaker. The oxygen sensor is immersed below the water surface and continually circulated as the measurement is taken. Because the membrane absorbs oxygen across its surface, if the sensor remains in a steady location, it will deplete the oxygen content over time and give a false low reading. However, in our testing, the continual swirling of the probe reintroduces oxygen into the degassed water, therefore as seen in Fig. 3-10, the oxygen content appears to rise over time from an initially low reading of 0.1 mg/L. From this measurement, the oxygen content in the water has dropped 8.5 mg/L due to helium sparging. However, since nitrogen and helium content cannot be measured, it can only be inferred that the total reduction in non-condensable gases is of similar magnitude.

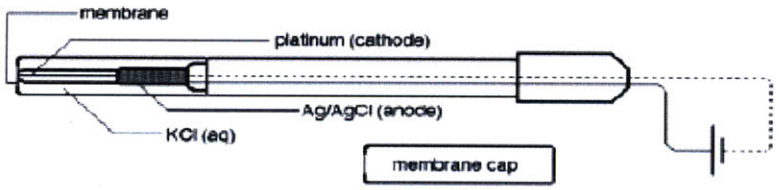

Fig. 3-9 Diagram of the Vernier DO-BTA dissolved oxygen sensor showing the interior anode-cathode circuit that measures current proportional to the diffusion of oxygen across the membrane [21].

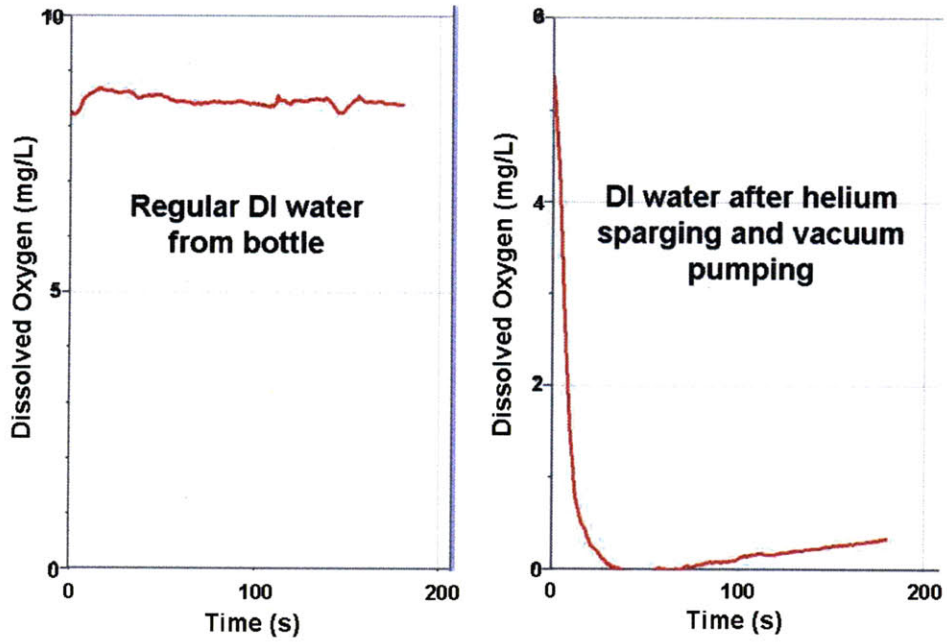

Fig. 3-10 Screen snapshot of Vernier Logger Pro 3.8 graph of dissolved oxygen content versus time.

In addition to the dissolved oxygen measurement, the non-condensable content is also verified by condensing flow testing. For an initial simple test, the degassed water is vaporized at 80 °C and sent through a stainless steel tube immersed in an ice bath as shown in Fig. 3-11. The exiting line was all liquid at a temperature of 65 °C, therefore completely condensed, and displayed few non-condensable gas bubbles. These results showed enough promise to move forward with imaging in the test section. As shown in Fig. 3-12, the condensing flow showed fewer non-condensable bubbles collected in the test section than previous results from vacuum degassing. However, the single bubble

near the right-side liquid exit was still large implying that further improvement to the degassing is required. In evaluating drawbacks of the helium sparging method, major concerns revolved around the large volumes required to fill the vapor tank and the need to transfer the liquid after degassing by gas pressurization.

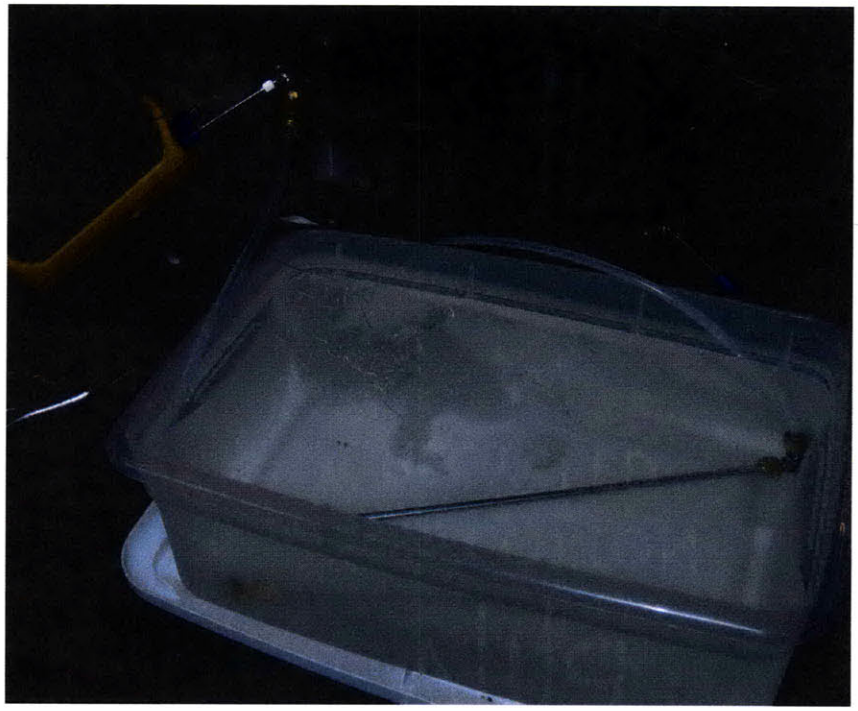

Fig. 3-11 Initial testing of degassed water quality by vaporizing and condensing by flowing through a stainless steel tube immersed in an ice bath. The vapor comes in on the right and exits as water on the left. The water line showed few non-condensable bubbles implying that helium sparging was moderately successful.

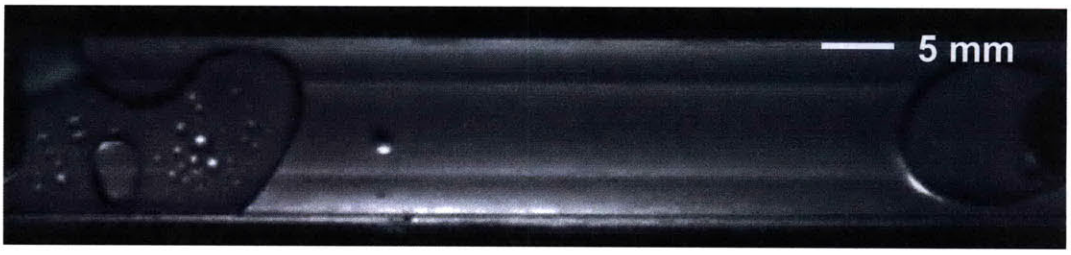

Fig. 3-12 Image of condensing flow in an open channel after helium sparging. The bubble on the right hand side of the flow channel is still substantial but shows an improvement in removal of non-condensable gases when compared to vacuum degassing.

Freeze-Pump-Thaw (FPT) Cycling

Concept

In Freeze-Pump-Thaw (FPT) cycling, the fluid to be degassed is sealed in a container and rapidly frozen by immersion in liquid nitrogen [22]. During crystallization, the air separates from the water and either escapes to the vapor space or is trapped into a pocket by the freezing front. Vacuum is pulled on the container with the fluid frozen to minimize the removal of vapor while the non-condensable gases collected in the vapor space are evacuated. The fluid is then warmed to room temperature during which time bubbles of trapped gases can escape to the liquid-vapor interface by buoyancy before dissolving back into solution. The cycle is repeated multiple times (3 minimum) to successively decrease the concentration of non-condensable gases in the fluid. This method is especially attractive for condensing flow testing because the degassed water can be processed in the same container that can be later used as a vapor source for experimental setup. Therefore in addition to achieving low levels of dissolved gases, this method also minimizes the chance for the gas to dissolve again prior to experimental use.

Equipment

The water first used in the FPT cycling was ACS Reagent Grade, ASTM Type I deionized, double distilled water (RC91501, Ricca Chemical). In later FPT experiments, the water was improved to high purity HPLC grade (JT4218-2, J.T. Baker) due to its low levels of organic compounds. The water is degassed in the 500 mL volume stainless steel container shown in Fig. 3-13. The container was fabricated from a 3" diameter butt weld tube adaptor (50485K195, McMaster) with a sanitary tube fitting flange at the top and a rounded cap welded onto the base. A lid with the complementary sanitary tube flange

(50485K224, McMaster) was modified by welding in the following ports: a female ¼" Swagelok fitting, a male ¼" NPT fitting, and a male bored-through 1/16" Swagelok fitting. A ball valve and copper line running to the vacuum pump are attached to the ¼" Swagelok. An absolute pressure transducer capable of reading -14.7 to 15 psi (PX209-30V15G5V, Omegadyne) is attached to the NPT fitting to monitor vacuum level during degassing and later during experimental testing. A 2" long type-T thermocouple probe (TTSS-116U-2, Omega) is inserted into the container through the 1/16" Swagelok to monitor temperature. The container and lid are sealed with a PTFE gasket (43315K27, McMaster) and high-pressure bolted clamp (4322K714, McMaster).

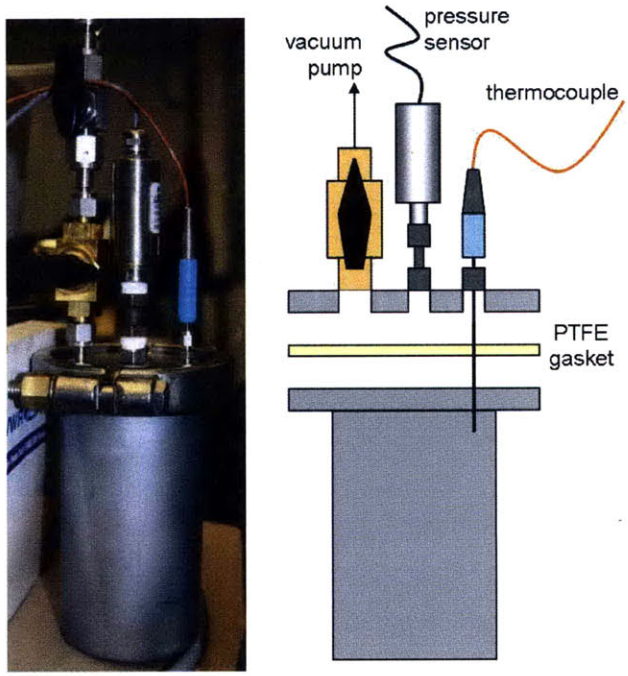

Fig. 3-13 Image and schematic of the stainless steel container used for FPT. The lid included a ball valve to control vacuum pumping on the container and a pressure transducer and thermocouple to monitor conditions inside the container during the cycles.

A schematic of the experimental setup used for FPT degassing is shown in Fig. 3-14. The oil-lubricated rotary vane vacuum pump (2010SD, Adixen) shown in Fig. 3-15 is used to pull vacuum on the container. The 60 Hz performance curve for this pump is

shown in Fig. 3-16, indicating an ultimate pressure of 2 mTorr. The container is connected to the pump via the following vacuum system components: (in order) vacuum sensor, vacuum-rated valve, liquid nitrogen trap and pump filter. A thermocouple vacuum sensor (DV-6M, Teledyne Hastings) with a 1 – 1000 μHg range analog vacuum gauge (VT-6A, Teledyne Hastings) is located adjacent to the container for sensitivity to vacuum level in the vapor space and gasket leakage. A ball valve immediately upstream can be shut to allow the vacuum sensor to read static pressure in the container or to allow pump to remain running while the container is disconnected from the line. The inline liquid nitrogen trap (LNT-4-100-K, Key High Vacuum Products) is used to protect the pump by freezing vapor and any liquid water from the evacuated air stream. Water that reaches the pump and contaminates the oil causes degradation of the vacuum pump's ability to reach low ultimate pressures. The adjacent filter (335025, Mass-Vac Posi-Trap) prevents contaminants from entering the vacuum pump and oil vapors from backtracking from the pump to freeze in the liquid nitrogen trap. An oil mist eliminator (OME 25 S, Adixen) is used on pump exhaust to prevent oil vapor from being vented into the room.

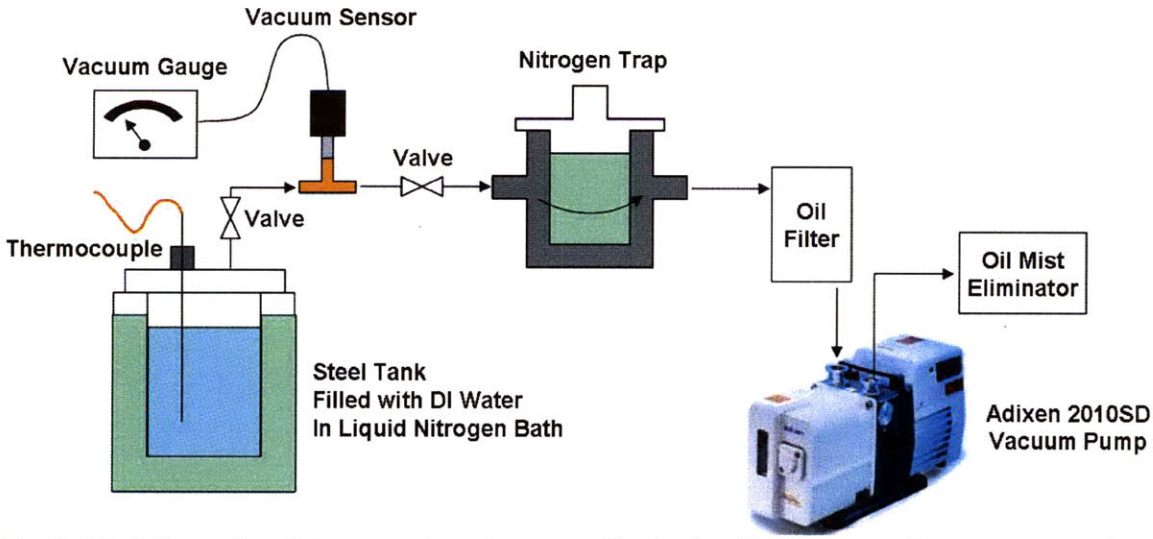

Fig. 3-14 Schematic of the experimental setup for during the freeze and pump steps of FPT cycle degassing.

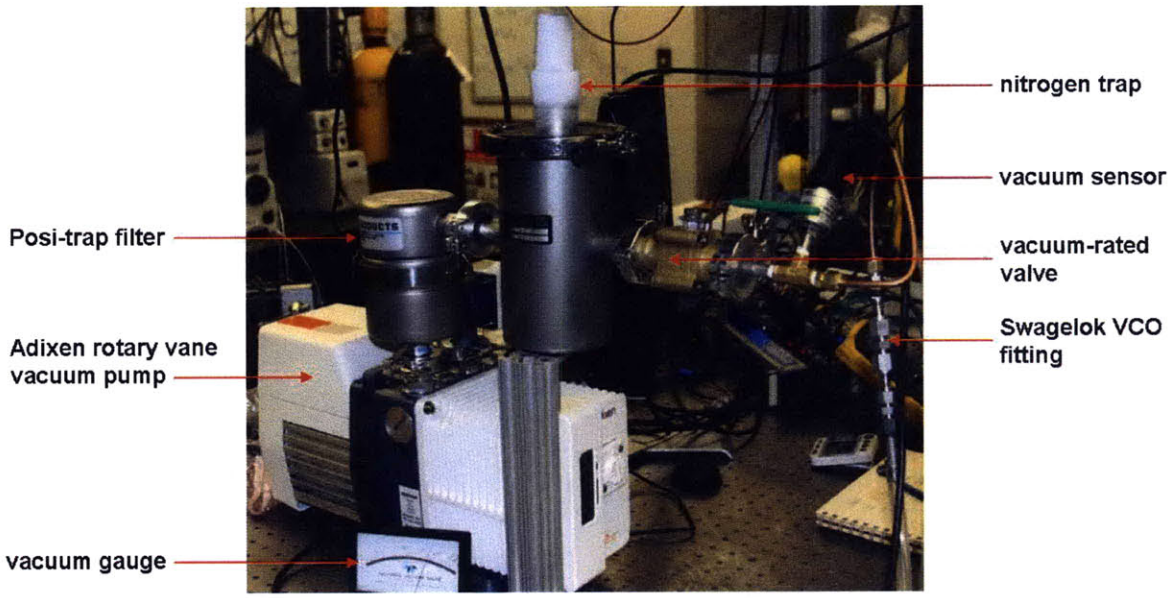

Fig. 3-15 Image of the vacuum pump setup used for FPT degassing.

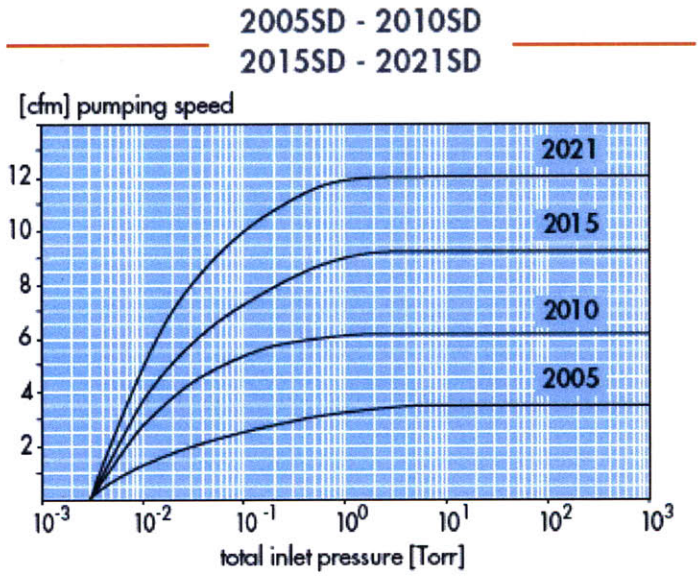

Fig. 3-16 Pump performance curve for Adixen 2010SD vacuum pump operating at 60 Hz with a ultimate pressure of 2.3 mTorr and a maximum pumping speed of 6.8 cfm (1 mTorr = 1 μHg) [23].

Procedure

To remove organic contaminants prior to starting FPT cycling, the stainless steel container is disassembled and the interior, lid, and gasket sealing surface are cleaned thoroughly with acetone. The parts are then rinsed with DI water to remove any alcohol

residue. The PTFE gasket is cleaned with isopropanol, lightly regreased with fluorosilicone-based Vac Goop (MS-TL-VGT, Swagelok), and then reinserted between the lid and the container body. The bolted clamp is tightened to create a vacuum seal. A mica band heater (3671K151, McMaster) capable of 400 W at 120 VAC is wrapped around the container and the assembly is connected to the vacuum pump using Swagelok fittings and copper tubing. A Swagelok VCO o-ring face seal fitting is included in the line to accommodate frequent disconnection of the container without concern of wearing out the traditional Swagelok ferrules. The container is evacuated for one hour while the heater is operated at half power by means of a variac (TDGC-2KVA, Johsun) to vacuum bake-out any compounds that may outgas from the stainless steel tank. After cooling to room temperature, the clamp and lid are removed to allow for filling the container with water. To accommodate the volume change when water freezes and still allow for a vapor space over the ice, the 500 mL container is filled with only 440 mL of DI water. If the volume of water is too large, the expansion of the ice could push up on the lid and potentially cause damage to the thermocouple or leakage of the gasket. The gasket is then regreased and the container resealed.

To prepare for the freezing step of the FPT cycle, a sheet of fiberglass insulation and a ring of Styrofoam are slid onto the container until they touch the clamps to insulate the gasket from the liquid nitrogen vapor. During previous FPT tests, gasket leakage was identified during the pumping step as a rapid rise in pressure on the vacuum gauge after closing the ball valve. The leak appeared to develop over time on an initially sealed container as the gasket grew colder. It was found that insulating the gasket prevented leakage for the duration of the freezing and pumping steps.

During the freezing step of the FPT cycle, the container and gasket insulation are placed upright in an insulated basin filled with liquid nitrogen as shown in Fig. 3-17. The container is connected to the vacuum pump with the valve closed in order to evacuate the copper tubing. The vacuum gauge will typically read below 10 μHg and often as low as 1 μHg when just pumping on the dead-ended copper line. As the water freezes, the liquid nitrogen vaporizes and the level in the basin drops. During the freezing and pumping steps, liquid nitrogen needs be refilled periodically, in our case by pouring from a 1 liter dewar, to maintain the level approximately 1" below the insulation. The freezing step should last for 20 to 30 minutes until the thermocouple reads below 0 °C.

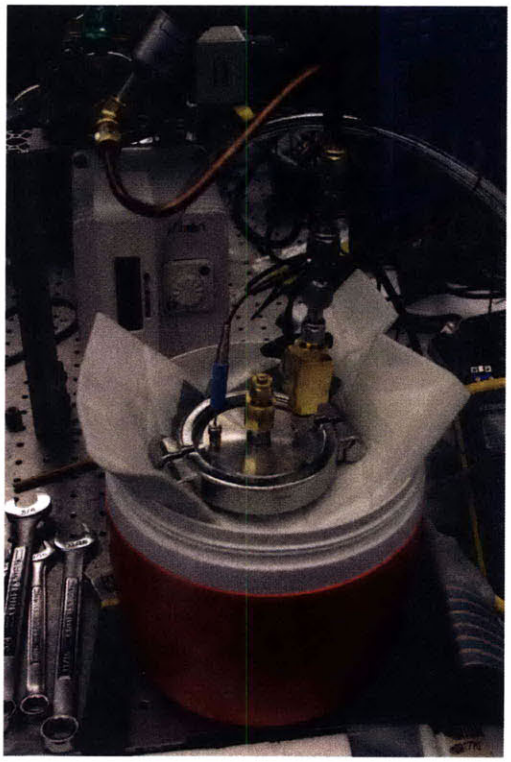

Fig. 3-17 Freezing step of FPT cycle where container is sitting in a basin of liquid nitrogen. A sheet of fiberglass insulation and a ring of Styrofoam (not shown) are used to insulate the gasket and prevent leaking.

For the pumping step, the valve on the container lid is opened to the vacuum pump while the container remains in the nitrogen basin. Upon opening the valve after the

first freezing step, the vacuum gauge will jump up to a reading between 1000 μHg and ambient as all the non-condensables, trapped in the tank during filling and released during the first freezing, start to be removed. Over 20 to 30 minutes of pumping, the vacuum gauge will fall as the non-condensables in the vapor space are evacuated and the water further drops in temperature. As shown in Fig. 3-18, the vapor pressure of water under saturation conditions will be above 10 μHg until the ice surface temperature drops below -60 °C. Therefore, the vacuum gauge will read high pressures until the thermocouple temperature falls sufficiently. The water vapor removed by the pump will freeze in the nitrogen trap, requiring more liquid nitrogen to be added to the trap periodically during the pumping step. From previous testing, it was found that air trapped in the valve could also cause higher gauge readings. To eliminate the air, the valve should be cocked halfway between open and closed while pumping until rotation between the two positions no longer causes a jump in the vacuum gauge reading. At the end of the pumping step, the valve on the container and the vacuum pump ball valve are shut and the container is disconnected at the Swagelok VCO fitting. With the vacuum ball valve shut, the pump can continue to run if the FPT cycle will be repeated. The container is then lifted out of the liquid nitrogen basin using protective gloves and the insulation is removed. A frost layer will build up on the container surface from freezing water vapor in the air. Therefore, it is important to quickly attach the mica band heater for the thawing step to ensure good contact with the stainless steel surface.

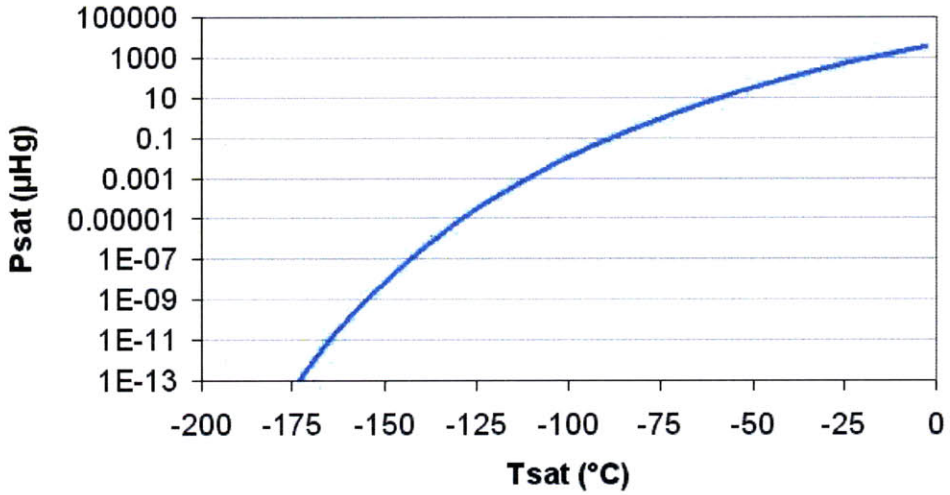

Fig. 3-18 Graph of saturation pressure vs. saturation temperature for water. For the vacuum gauge to read below 10 µHg during the pumping step, the top surface of the ice must be below -60 °C.

Once the band heater is attached for the thawing step, the tank is placed on a sheet of fiberglass insulation to prevent it from freezing to the optical table. The variac is set to 30 V to allow for slow heating. The thermocouple in the lid is monitored and the thaw step is ended when it consistently reads 40 °C, usually in 20 minutes. Additionally to ensure that all the ice has melted, the container is lightly shaken to detect the sound of floating ice colliding with the stainless steel surface. Once thawed, the variac is turned off and the band heater is removed from the container.

The FPT cycle is repeated five times. As a final shutdown procedure after the last pump step is completed, the vacuum pump is turned off and the ball valve is opened to release vacuum inside the trap. The quick-clamp on the trap is unfastened so that the nitrogen reservoir can be removed. Any remaining nitrogen is poured back into the larger dewar. Commonly, the frozen water vapor will form "snow caps" at the inlet and outlet that can potentially block flow through the trap as shown in Fig. 3-19. The stainless steel reservoir is held under running tap water to melt any ice on the surface and bring the container back to room temperature. After towel drying, it is fastened back into

the trap and the vacuum pump is turned back on for a few minutes with the ball valve closed. During previous experiments, it was found that a frozen trap when left overnight under vacuum would be completely dry the following morning. Therefore, it is hypothesized that the ice melts once the nitrogen boils off and then vaporizes under the vacuum conditions. This water vapor could migrate to the pump oil and, over repeated cycles, cause degradation of pump performance. Pulling vacuum on an empty, dry nitrogen trap ensures that the pump will be sealed from any water vapor or contaminants in the air when not in use.

To determine the success of the five cycles of FPT, the container filled with degassed water is incorporated into the experimental setup described in detail in Chapter 4. Heat is applied to the container via the same mica band heater used for thawing and this heat provides the vapor source to a test section where condensing flow is visually observed. The images of the condensing flow with FPT water in Fig. 3-20 show a reduction in gas bubbles after the condensing length when compared to the results from the other degassing methods. Additionally, the clear plastic outlet line of the test section is monitored during the flow imaging and, with few exceptions, the line is filled with liquid and no gas bubbles are observed. This method resulted in the highest quality of water degassing for condensing flow testing. The experimental testing used to generate the image in Fig. 3-20 will be discussed in detail in Chapter 5.

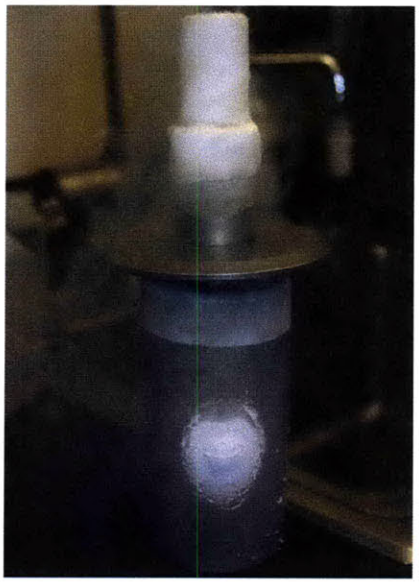

Fig. 3-19 Image of "snow caps" on the exterior of the nitrogen trap caused by droplets of water vapor freezing upon contact with the cold nitrogen trap.

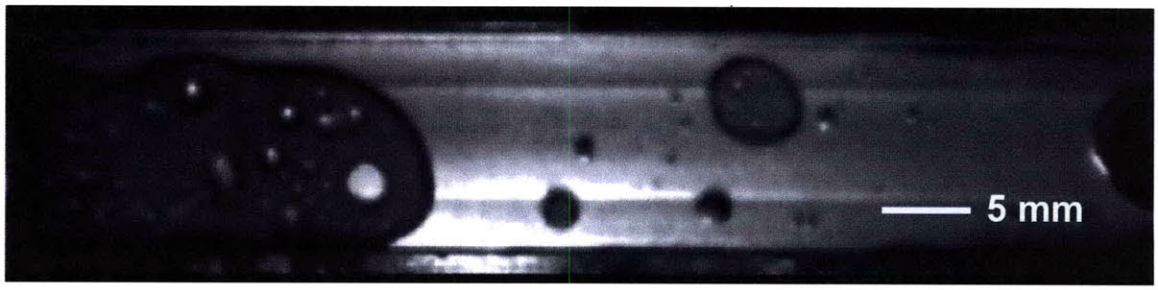

Fig. 3-20 Image of condensing flow after FPT degassing in an open channel. The small bubbles near the middle of the channel and over the exit hole on the right show the decreased presence of non-condensable gases when compared to vacuum degassing and helium sparging techniques.

Conclusion

In conclusion, vacuum degassing, helium sparging, and freeze-pump-thaw (FPT) cycling were all investigated as potential methods for deaerating the water used as a working fluid in the experimental setup and the future heat pipe. Condensing flow testing with the processed water showed that the lowest non-condensable concentration remained after FPT cycling. This advantage stems primarily from the low achievable vacuum pressure, small volume, and minimal air exposure after degassing.

Chapter 4: Experimental Test Setup

Overview

An experimental test setup was constructed to validate the heat pipe condenser design. The system was improved three times, over the course of many "lessons-learned". The outcome was a setup with a small footprint, reliable measurement results, and flexibility to test a variety of designs. In the end, the setup was capable of mimicking the condenser conditions within the heat pipe

Initial "Cart-Scale" Experimental Setup

System Design

The first experimental setup was designed around high capacity reservoirs, heavily instrumented flow paths, and versatile testing conditions. The large volume of liquid could accommodate both fast condensing flow rates and long testing periods. The instrumentation could measure pressures, temperatures, and flow rates in both the condensing and cooling loops. The test section could easily adapt to varying channel geometries in addition to different mediums and orientations of backside cooling.

As shown in the schematic in Fig. 4-1, the complete setup includes a vapor generation system and a test section with a cooling loop. The vapor generation system consists of two large capacity tanks connected in a loop with a vacuum pump, a post condenser, and a valve to control mass flow. An image of the entire "cart-scale" system is shown in Fig. 4-2. The tanks are 3-gallon capacity pressure vessels (41705K42, McMaster) with vacuum caps and four ports (three ¼" and one $^{3}/_{8}$" NPT) for connection to additional lines and measurement apparatus. The evaporation ("hot") tank is mounted

right-side up with an absolute pressure transducer (PX209-30V15G5V, Omegadyne) monitoring the vapor space and a 12" long thermocouple (NB1-CPSS-116U-12RP-TT36, Omega) extending into the liquid. The tank is wrapped with a silicone rubber heater (35765K385, McMaster) capable of dissipating 720 W and used to generate the vapor input into the test section. The leads for the heater are routed through a solid state relay (SSR330DC75, Omega) that flashes the heater on/off at full power to maintain the tank at a constant 80 °C. The low temperature ("cold") tank is mounted upside down on the top level of the cart to create a gravity head capable of draining water back into the hot tank. The vapor space of the cold tank is monitored by a pressure transducer and thermocouple like the ones used on the hot tank. The vacuum pump (1402, Welch) is used to remove air and pull both tanks and the connecting lines down to vacuum pressure such that the water in the tanks is under saturation conditions. The saturation pressure difference between the 80 °C hot tank and the 25 °C room temperature cold tank drives flow through the condensing loop. A post condenser is located downstream of the test section to ensure that the flow is completely condensed and at room temperature before returning to the cold tank. The post condenser is a fan-cooled heat exchanger (35145K521, McMaster) capable of 300 W of air-cooling at a liquid flow of 2 gpm inside the stainless steel tubing. Shown in Fig. 4-3 alongside other equipment, a metering valve and liquid flow meter are located downstream of the post condenser to control and quantify the condensing flow rate. The low-flow metering valve (SS-SS4-VH, Swagelok) has 10 turns until open and a maximum flow coefficient (c_v) of 0.004. The liquid water flow meter (L-50CCM-D/5V, Alicat Scientific) has a range of 0-50 ccm and calculates the volume flow rate ($\dot{V}$) using the Poiseuille Equation 4.1 for laminar flow.

$$\dot{V} = \frac{\pi r^4 \Delta P}{8\eta L} = K \frac{\Delta P}{\eta(T)} \tag{4.1}$$

The meter subdivides the liquid into multiple small channels of known geometry (K) and measures the pressure drop (ΔP) and temperature. The temperature is used to determine the viscosity (η) of the water flowing through the meter. Although ¼" diameter stainless steel tubing is used at the ports of both tanks, most of the connecting lines in the system are made from ¼" diameter, semi-clear, vacuum-rated PFA tubing (51805K86, McMaster) for its low conductivity and the ability to see the condition of the condensed liquid flow between the test section exit and the downstream cold tank.

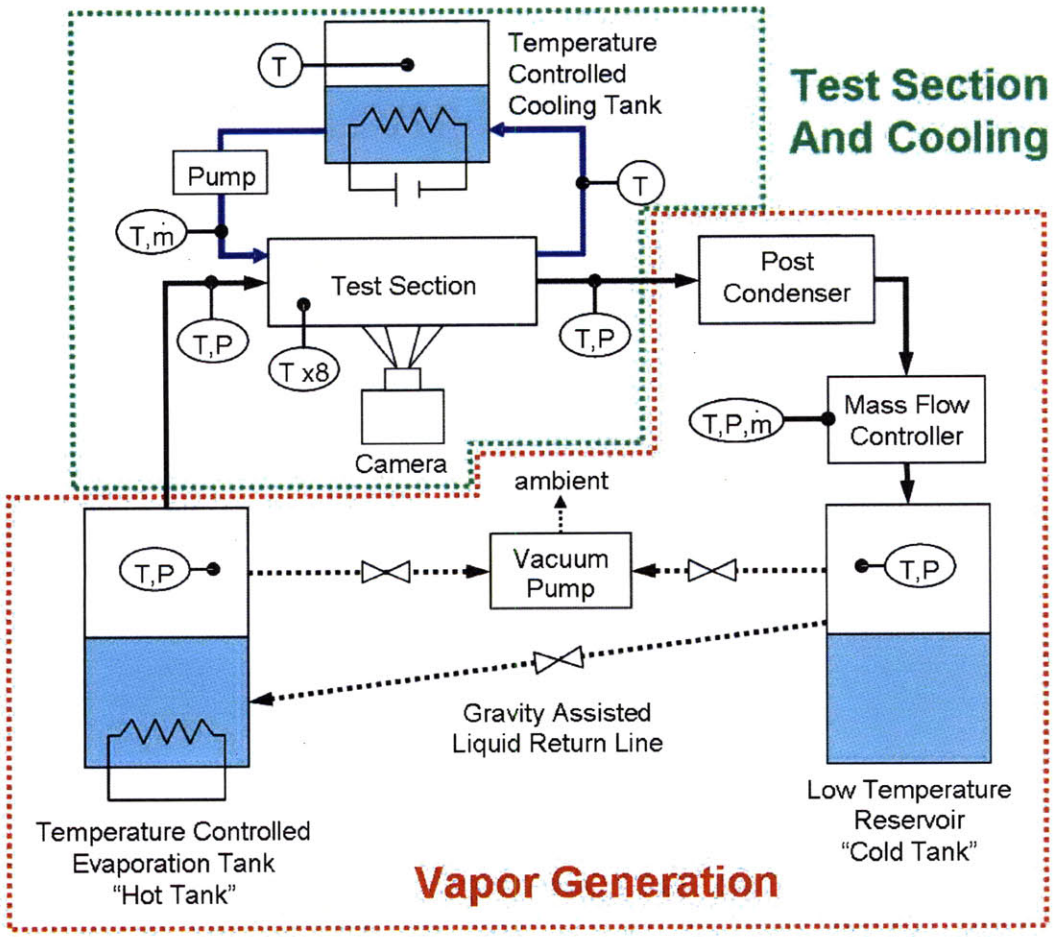

Fig. 4-1 Schematic of initial experimental setup showing both the system that generates and monitors the condensing flow and the test section where the condensing flow is visualized and modified. T = thermocouple, P = pressure transducer, m = mass flow meter.

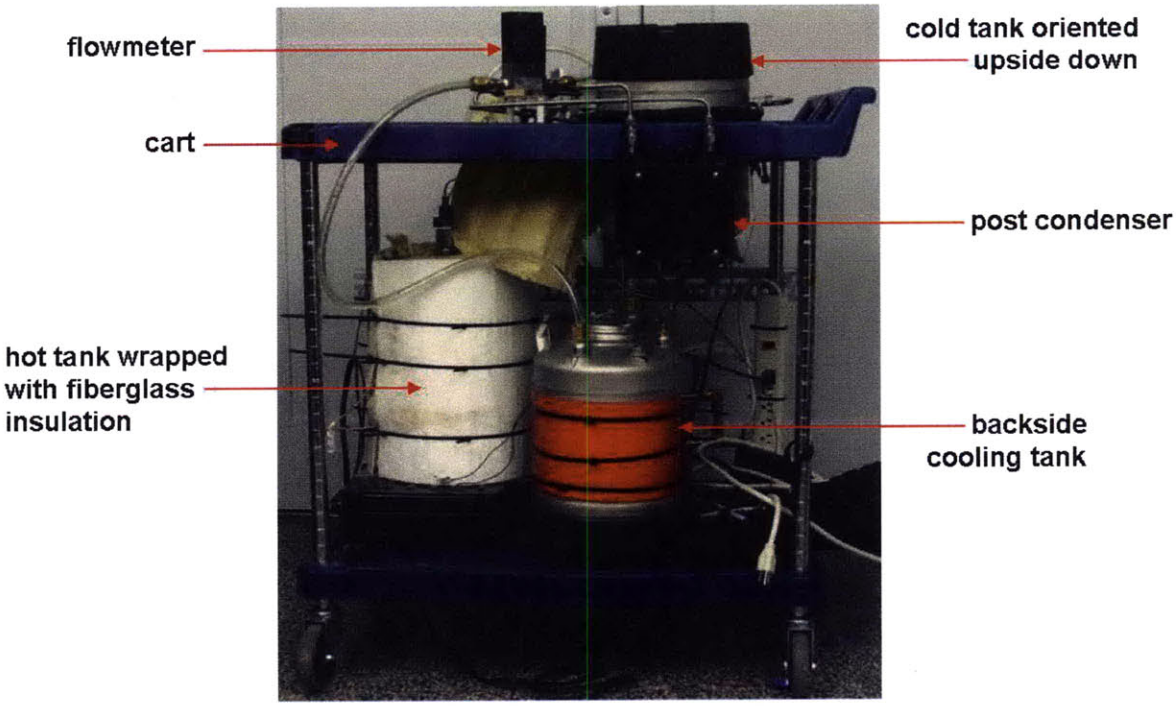

Fig. 4-2 Image of initial experimental setup showing scale and relative locations of the vapor generation and backside cooling equipment.

Fig. 4-3 Image of the mass flow meters, pressure transducers, and valves for monitoring and controlling flow in the condensing and cooling loops.

The cooling loop on the backside of the test section consists of a water storage tank, circulating pump, volume flow meter and multiple thermocouples. The tank and pump are shown in Fig. 4-4. The water storage tank is a duplicate of the 3-gallon

pressure vessel wrapped with a silicone rubber heater that is used as the hot tank. The tank is filled with standard DI water that has not been degassed. The silicone heater is again controlled by a solid state relay to set the circulating liquid to a desired temperature in the range of 30 °C-70 °C. A port on the top of the tank remains open to maintain ambient pressure while a thermocouple monitors the liquid temperature. The liquid is circulated through the heat exchanger on the backside of the test section using a flexible impeller pump (4381K17, McMaster) capable of a maximum flow rate of 6 gpm. A bypass line with a globe valve is included near the impeller to allow for flow rate adjustment between 1000 and 2000 ccm. The flow meter and thermocouples at the inlet and outlet of the heat exchanger enable calculation of the heat absorbed by the cooling water due to the condensing vapor in the test section.

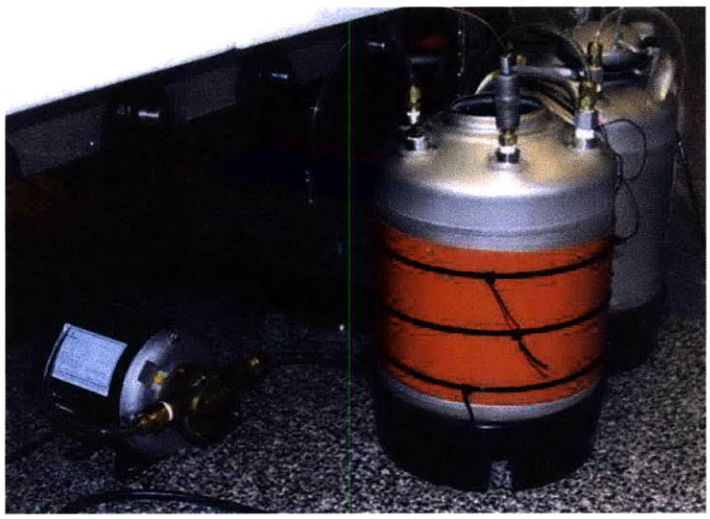

Fig. 4-4 Image of the water storage tank with silicone heater and the circulation pump used in the backside cooling loop.

The test section, shown in the schematic in Fig. 4-5, is a combination of a condensing flow visualization channel and a heat exchanger. The top plate, machined from ½" thick ultem, includes a recess for the viewing plate, o-ring groove, inlet and outlet ports for condensing flow, and ports for attachment of a differential pressure

transducer. The viewing plate is $^1/_8$" thick polycarbonate sealed into the top plate with either Bondit 45 epoxy (7513A1, McMaster) or soft silicone gasketing (9010K111, McMaster). The $^1/_8$" thick copper base plate is machined to include the condensing flow channel on the front and 7 thermocouple grooves on the back. The standalone heat exchanger, shown in Fig. 4-6, is formed by adhering the $^1/_{16}$" thick copper cover onto the bottom plate using Bondit 45. The bottom plate, also machined from ½" thick ultem, includes inlet and outlet ports and a 1 mm thick gap for flow of the cooling liquid on the backside of the copper cover. To assemble the full test section, a thin layer of thermal grease (OT-201-2, Omega) is coated onto the copper cover and the copper base is placed on top. The condensing flow side is vacuum sealed by tightening the 10-32 screws around the periphery of the top plate causing the o-ring to compress onto the copper base plate. Thermocouples are then inserted from the side into the appropriate copper base plate grooves. A photograph of the assembled test section is shown in Fig. 4-7.

During operation, vapor enters the test section through the inlet port on the top plate, takes a 90° turn, and flows into the channel. Due to the water cooling on the backside of the channel, the vapor condenses as it flows across the plate. The backside cooling flow is oriented perpendicular to the condensing flow to ensure that any point along the length of the channel experiences the same cooling liquid temperature. When the condensed flow reaches the end of the plate, it takes another 90° turn and exits through the top plate outlet port. The condensing flow is imaged from above using a 1.3 megapixel monochrome camera (PL-B741EF, PixelInk) at 30 fps as shown in Fig. 4-8. The temperatures of the inlet and outlet flow of the test section are monitored with type-T thermocouples protruding into the flow path and the pressure drop across the test section

is measured with a differential pressure transducer (FDW-1-AT-2d-5a-6q-1y, Honeywell). The temperature profile along the flow channel is measured by 7 type-T thermocouples (5TC-TT-T-30-36, Omega) inserted into the grooves on the backside of the copper base plate.

Temperatures, pressures and mass flow rates were monitored and recorded as excel files during experimental testing using a Labview program. Additionally, the interface included adjustable set points for control of tank heaters and offsets for zeroing measurement equipment prior to testing. The block diagram and interface for the program is shown in Appendix B.

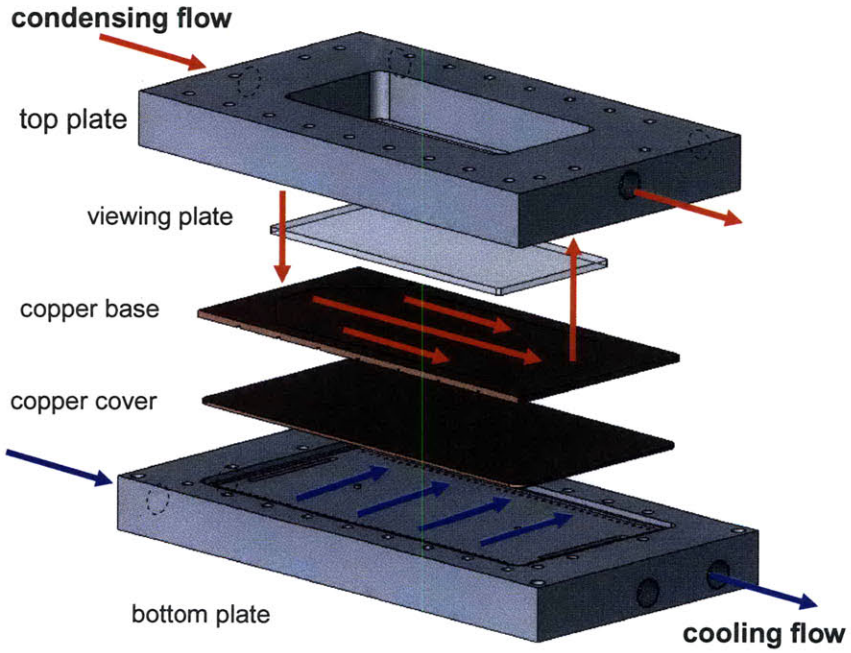

Fig. 4-5 Schematic of the test section design showing the condensing flow path (red) that can be imaged through the viewing plate and the cooling flow path (blue) through the backside heat exchanger.

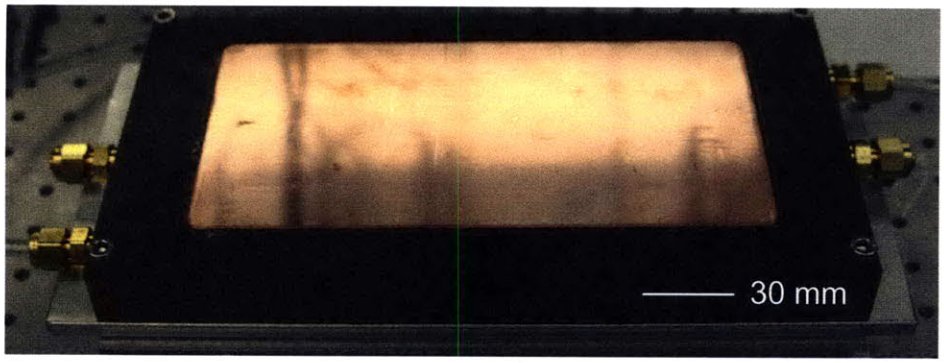

Fig. 4-6 Image of the sealed heat exchanger portion of the test section. A thin layer of thermal grease is coated on the surface to ensure good thermal contact between the copper cover and the copper base with the flow channel.

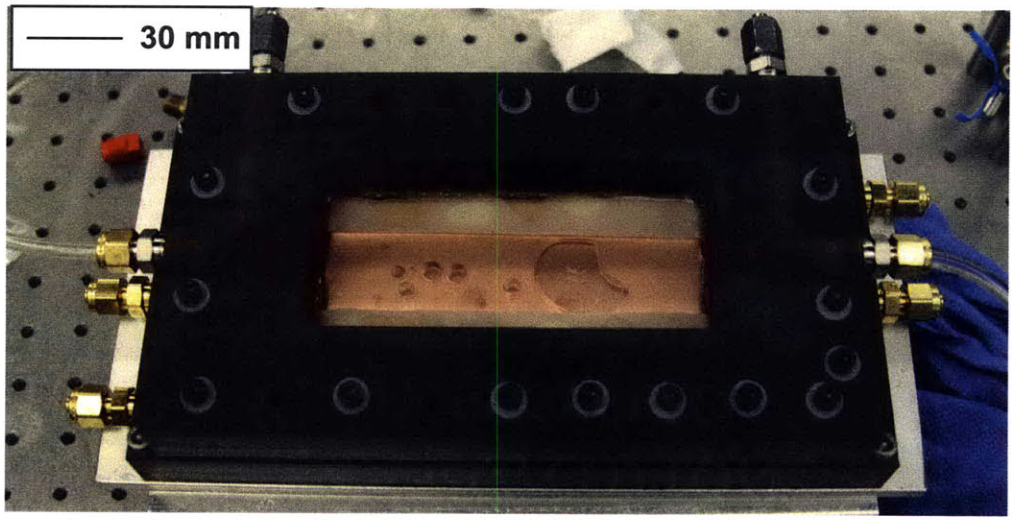

Fig. 4-7 Image of the test section showing liquid and bubbles moving through the condensing flow channel.

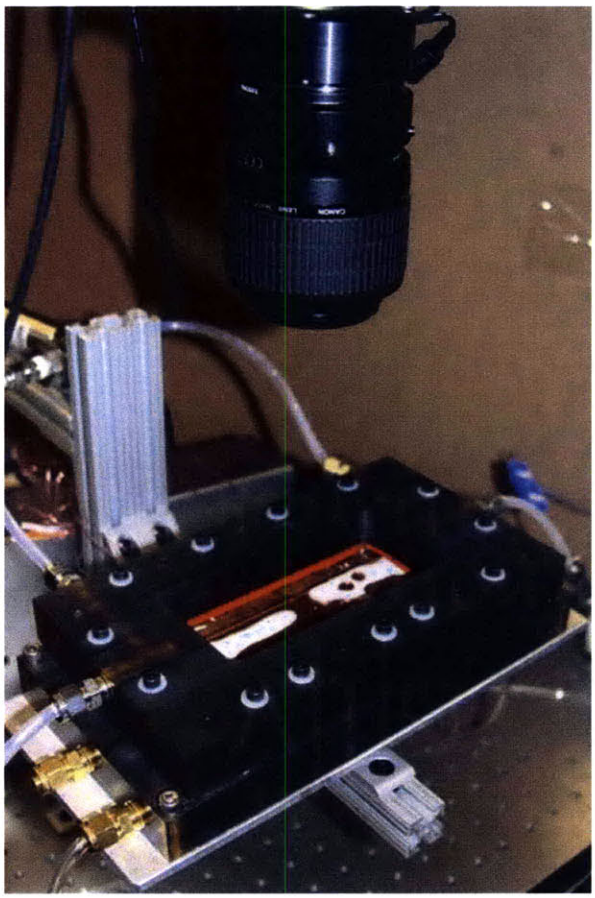

Fig. 4-8 Image of test section in operation as the overhead high speed camera records the condensing flow seen through the viewing plate.

System Performance

Although robust in size, the system had many drawbacks that were uncovered during condensing flow testing. To begin with, the large size of the system was a problem. Having the experiment on wheels was useful when it needed to be transported to other buildings for debugging, but when stationary, the "cart-size" setup occupied a large footprint that was then magnified when the liquid nitrogen dewar and vacuum pump were placed adjacent. The large volume of water in the tanks was a plus for system operation because it allowed for high flow rates and long experimental runs before the liquid needed to be emptied back into the vapor tank. However, the large volume also

made degassing difficult and resulted in flow imaging with large bubbles of non-condensables affecting the flow pattern. As described in Chapter 3, both vacuum degassing of liquid within this system and helium sparging of liquid that was then transferred into the system had mediocre results. Additionally, such methods were difficult to perfect when such a large volume was required to run validation tests of the condensing flow. These results implied that a smaller scale, smaller volume system would be advantageous.

Besides their scale, the tanks also had problems due to liquid level and connection lines. Since both tanks were stainless steel, it was impossible to see the change in liquid level over the course of condensing flow testing. A mechanical scale was placed under the hot tank in hopes of measuring weight change; however the stainless steel lines attached to the hot tank had enough of a spring constant that any change was difficult to resolve. Another problem was that the silicone heater on the hot tank was as wide as the tank's height. As the liquid level in the hot tank dropped, a portion of the heater was above the water line and just heating the steel tank. As shown in Fig. 4-9, extended operation under this condition caused the heater to turn black and effectively "burn-out". The rigid lines, lack of valves, and upside down orientation of the cold tank also made it impossible to remove the tanks from the system for easy emptying and filling. This became an especially big problem when it was discovered that the gravity head of liquid in the cold tank was not sufficient to overcome the vapor lock in the return line to the hot tank. The only way to get the liquid back to the hot tank was to release vacuum pressure in the cold tank to generate a full atmosphere of driving pressure. One of the biggest lessons learned in this design was that any exposure to air, no matter how brief, undoes

all of the effort to degas water in the system. Based on these findings, an improved system would allow for easy disconnection of the tanks for weighing, degassing and liquid return. The hot tank would have a thin heater located near the bottom to remain below the water level. Finally, the tanks would remain sealed and under vacuum after degassing to prevent non-condensables from contaminating the water.

Fig. 4-9 Image of hot tank wrapped in silicone heater shown distinct water line above which the heater has turned black from being burned out.

The test section also required improvement from its original version. Ultem was chosen for the main test section body because of its ability to withstand high temperatures. However its amber color required the viewing plate to be made from a different clear material (polycarbonate) and adhered in place. Ultem's property as a difficult-to-bond plastic limits the adhesives to Bondit 45, which does not bond with polycarbonate. It was possible to form a vacuum-tight seal by applying a frame of silicone gasket around the edges of the polycarbonate and pressing it into place. However, this method of sealing limited the base plate geometry to channels narrower than the viewing window for applying pressure to the gasket. The test section also had

problems with design and placement of the ports. The 90° turns within the ultem prevented direct viewing of the flow at the inlet and outlet. The placement of the inlet hole close to the top surface of the ultem lead to cracking adjacent to the inlet fitting due to the thermal gradient between the incoming 80 °C steam and the external ambient air. An image of the cracked top plate, after applying adhesive to seal, is shown in Fig. 4-10. Also, the large surface of the copper-copper interface between the base and cover plates required a large amount of thermal grease that was difficult to spread evenly over the entire area. The uneven coverage could lead to additional thermal resistance between the cooling liquid and the condensing flow. Finally, the substantial size and weight of the test section made it difficult to maneuver when investigating flow under different gravitational orientations. These results indicate that an improved test section would have a smaller size, higher visibility of the full channel, and be constructed from a single, thick, transparent material such as polycarbonate that can withstand the temperature range of the experiment testing. Additionally, the liquid cooling would be applied directly to the backside of the channel for improved heat transfer and to eliminate the use of thermal grease.

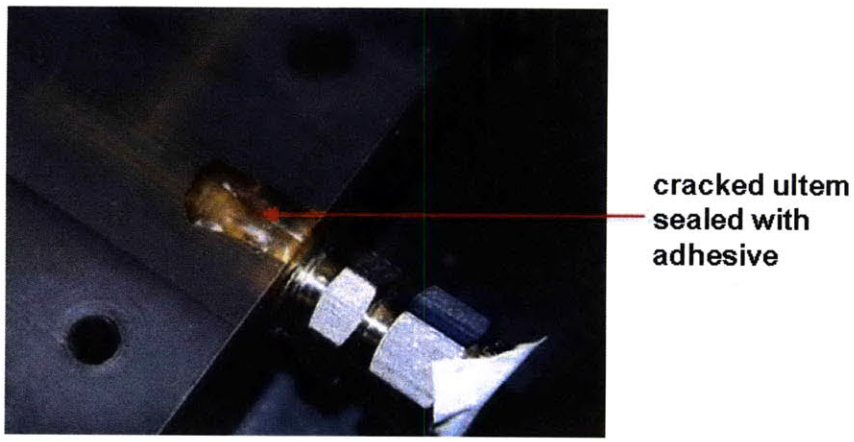

Fig. 4-10 Image of the test section after cracking at inlet fitting due to thermal gradient between incoming 80 °C steam and the external ambient air.

"Tabletop-scale" Experimental Setup

System Design

The "tabletop-scale" experimental setup was designed to address the problems observed during the build and operation of the initial condensing flow system. As shown in the schematic in Fig. 4-11, the fundamental components of the system are the same but most parts have been reduced in size to allow them to mount on an optical table. A photograph of the "tabletop" setup is shown in Fig. 4-12.

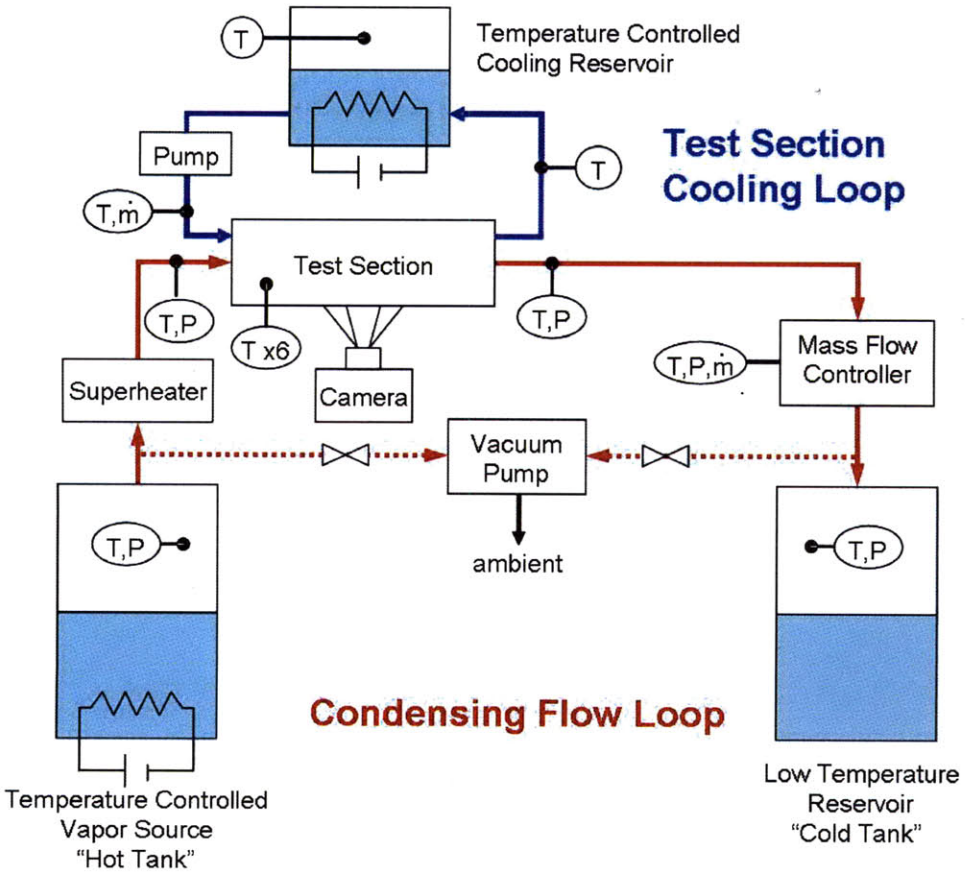

Fig. 4-11 Schematic of the "tabletop" experimental setup showing the condensing flow loop and the test section backside cooling loop.

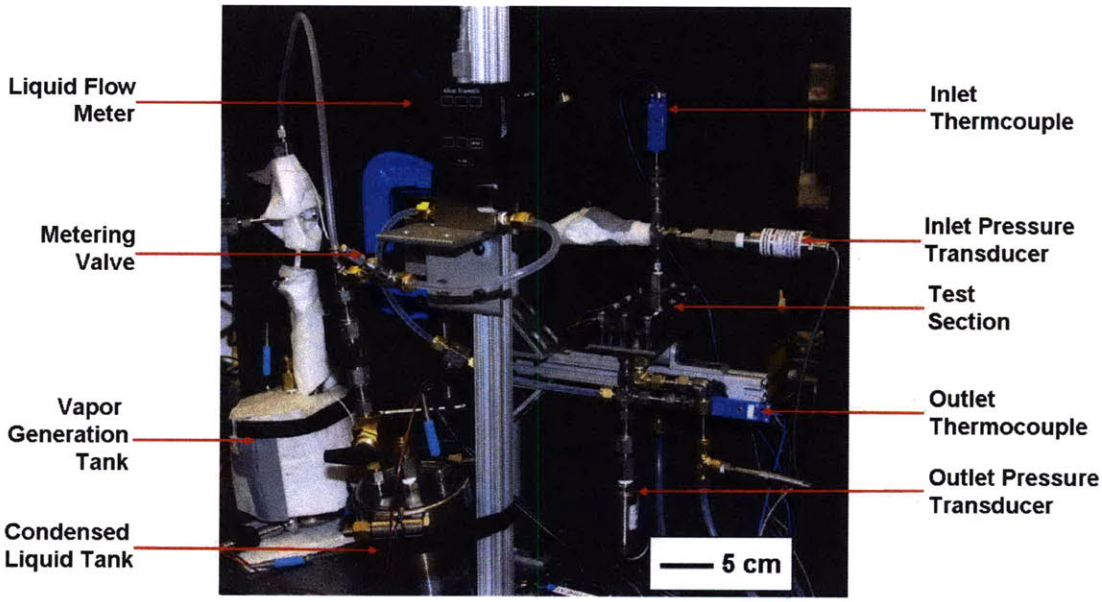

Fig. 4-12 Image of the "tabletop" experimental setup showing the smaller scale that enables all components to be mounted on an optical table.

The condensing flow loop operates in the same manner as in the previous experimental setup. The entire system is pulled down to vacuum pressure and flow is driven from the 80 °C hot tank to the ambient cold tank by the difference in saturation pressure. However, in this setup, the hot and cold tanks are 500 mL stainless steel containers described in detail in Chapter 4, the section on freeze-pump-thaw degassing. The tanks are outfitted with Swagelok VCO face-seal fittings and ball valves, as shown in Fig. 4-13, that allow for frequent, quick disconnection of the tanks from the lines without releasing vacuum in any part of the system. This disconnection feature is especially important because it eliminates the need for a liquid return line between the tanks. When the hot tank is empty, the hot and cold tanks can be switched with the valves closed and condensing flow continued once the tanks stabilize at the required temperatures. Therefore testing time is not limited by the smaller tank volume. The quick-disconnect feature also allows the tanks to be mobile for weighing, to determine water volume

inside, or for degassing external to the test system. The tanks are also outfitted with type-T thermocouples (TTSS-116U-2, Omega) extending just below the lid into the vapor space and the same absolute pressure transducers used on the tanks in the previous setup. This configuration allows for direct monitoring of the saturation conditions in both tanks during testing.

To generate the vapor, the hot tank is heated with a 3" diameter, 1.5" width mica band heater (3671K51, McMaster) capable of 400 W of heat dissipation at 120 VAC. The band heater is located near the bottom of the tank to ensure that, during a typical operation, the water level will remain above the heater to prevent burnout. The band heater is controlled by the solid state relay from the previous setup and the voltage can be reduced by adjusting the variac (TDGC-2KVA, Johsun) included in the circuit. As seen in Fig. 4-13, the tank is wrapped with fiberglass insulation (9346K38 and 9323K21, McMaster) to prevent heat loss from the band heater to the ambient environment.

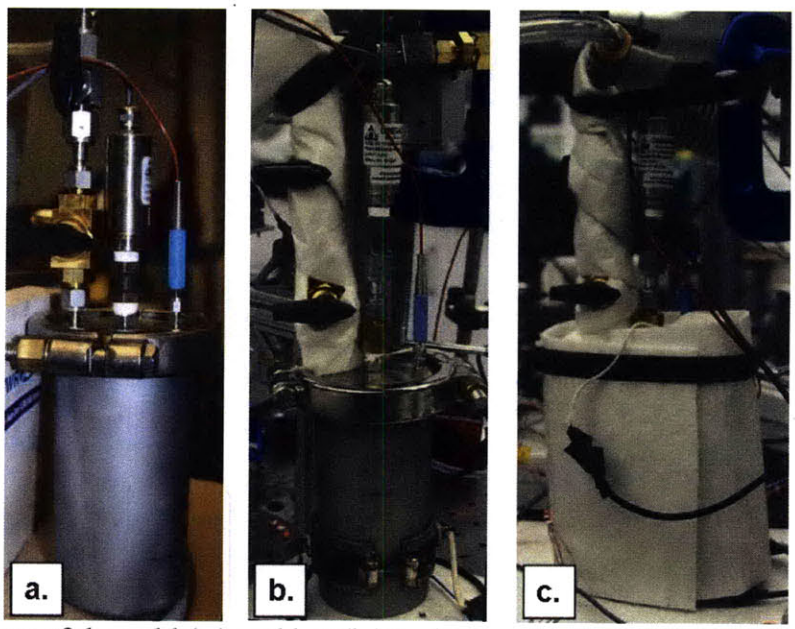

Fig. 4-13 Image of the cold (a.) and hot (b.) tanks used in the tabletop test system depicting that the lid is instrumented with valves and quick-disconnect fittings, a pressure transducer, and a thermocouple extending into the vapor space. Image (c.) is of the hot tank wrapped with fiberglass insulation.

To prevent pre-condensing of the vapor between the tank and the test section, a superheating coil was fabricated from 10 feet of ¼" diameter copper tubing and the entire vapor line is wrapped with high-temperature rope heaters (3641K24, McMaster). An image of the superheating section is shown in Fig. 4-14. During testing, a constant voltage of 60 V is applied to the rope heaters by a variac. The setting of the variac was determined as the voltage that caused the thermocouples at the test section inlet and inside the hot tank to match within 2 °C. Additionally, short lengths of PFA tubing were included after the superheating coil to visually verify that the vapor stream did not contain droplets of pre-condensed liquid.

It was not necessary to include a post condenser in this test setup because the condensed water lost enough heat as it traveled through the PFA tubing connecting the test section and the mass flow meter that vapor could not reach the mass flow meter.

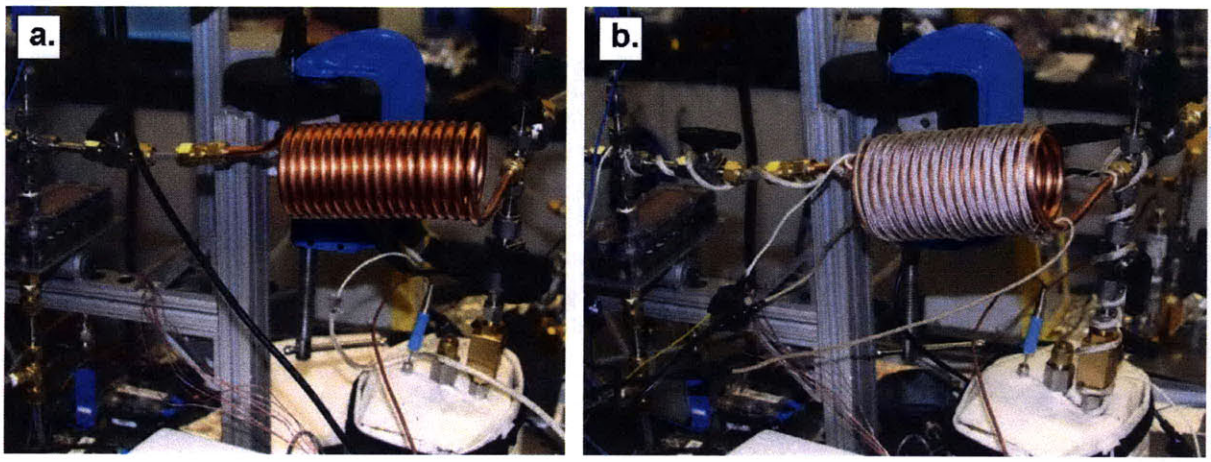

Fig. 4-14 Image of the superheating coil fabricated from 10 feet of ¼" OD copper tubing (a.). Image of rope heaters wrapped around the entire length of tubing, Swagelok fittings, and superheating coil connecting the hot tank to the test section (b.).

In addition to improving the quality of the vapor, the test section was also redesigned to better visualize the condensing flow and correct for the problems

experienced during the previous testing. As shown in the schematic in Fig. 4-15, the vapor enters through the top inlet on the viewing plate, condenses as it flows across the copper plate, and exits as liquid through a hole in the copper plate and an outlet in the heat exchanger. The transparent polycarbonate cover and the downward exit hole allow for viewing of the entire condensation path except for a small fraction at the inlet. Additionally, by placing the inlet and outlet holes into the large surface of the polycarbonate, problems resulting from thermal gradients are prevented. The vapor condenses as it flows across the copper plate due to direct liquid cooling on the backside of the channel. The cooling loop utilizes the same components as in the previous setup but now the heat exchanger is formed from the channel plate. This approach eliminates the use of thermal grease as an interface material and results in higher heat transfer to the cooling flow. Another improvement is that both open channel and sinter-filled channel copper plates can be studied in this test section. In the previous design with the inlet and outlet on the top, the liquid would have to reemerge from the sinter to exit which would likely result in vapor just bypassing the plate and exiting the test section. In this design as shown in Fig. 4-16, the sinter fills the outlet hole in the copper plate creating a direct path for the liquid in the sinter to exit while restricting the vapor to condensing on the sinter surface.

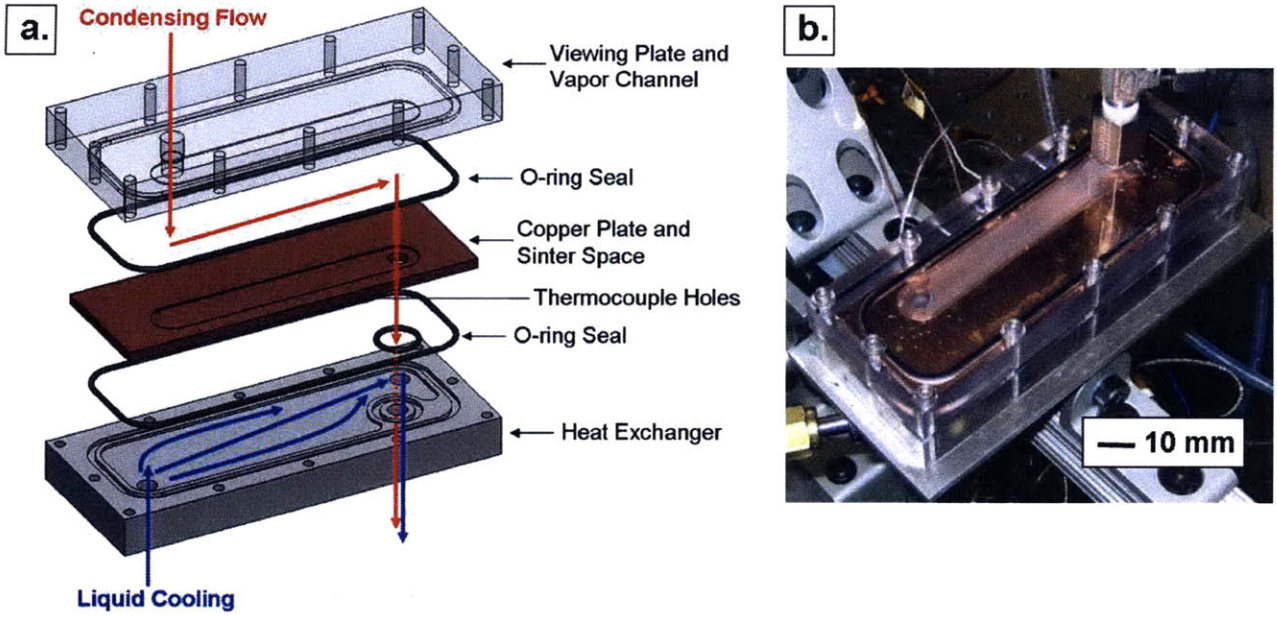

Fig. 4-15 Schematic (a.) and photograph (b.) of the redesigned, smaller test section that can be imaged from above through the polycarbonate top plate. The heat exchanger provides direct cooling to the backside of the channel plate.

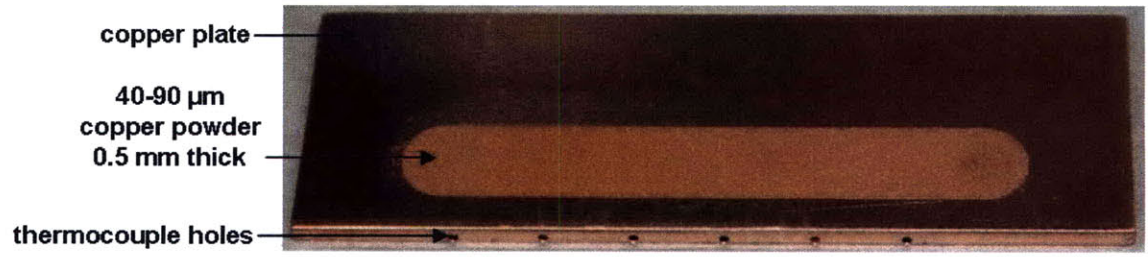

Fig. 4-16 Photograph of the sinter-filled copper plate showing that the sinter completely fills the exit hole.

The top viewing plate and bottom heat exchanger are machined from ½" thick polycarbonate. The top plate has a channel dimensioned as 0.5 mm height, 13 mm width, and 80 mm length. The $^{1}/_{8}$" thick copper plate has a similarly dimensioned channel and 6 small 0.042 inch (#58 drill bit) thermocouple holes drilled to a depth of the channel center-line. When testing an open channel plate, the full channel depth is 1 mm. When testing a sinter-filled plate, the channel has a 0.5 mm depth for vapor space in the polycarbonate and another 0.5 mm depth for sinter in the copper. The entire test section is sealed to vacuum pressure by tightening the #4-40 screws around the periphery of the

polycarbonate until the o-rings are compressed onto the copper plate. RTV sealant was used in addition to pipe tape on all the fittings threading into the polycarbonate pieces to safeguard against leaks. The small size and light weight of the test section allow for mounting the device to a pivoting stand. As shown in Fig. 4-17, flow can be imaged in the horizontal orientation, then the test section can be easily turned to vertical and flow imaging can continue after repositioning the camera.

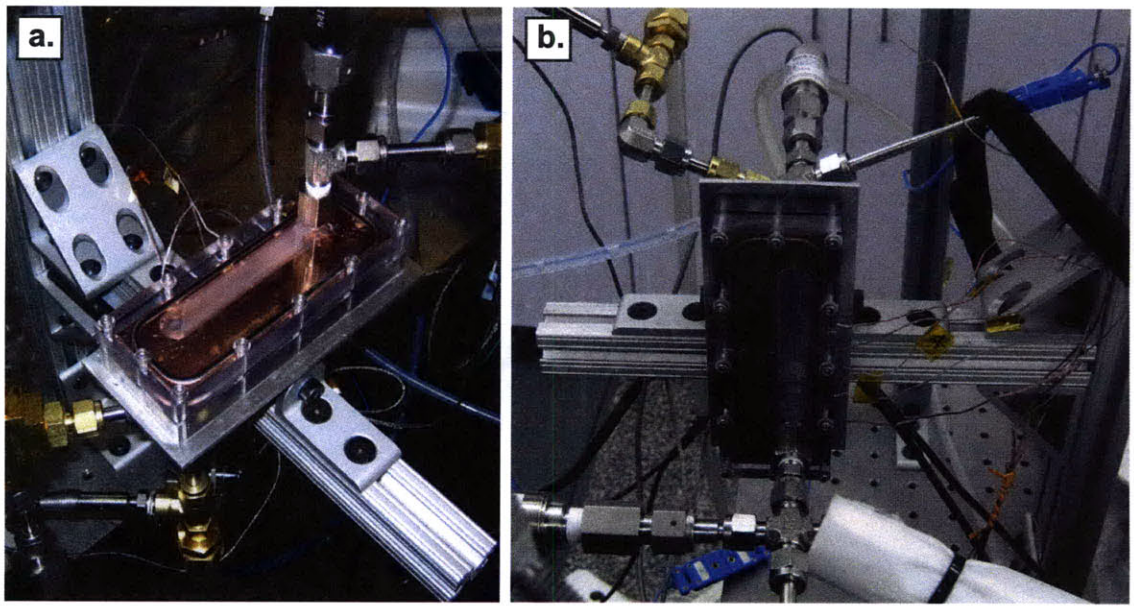

Fig. 4-17 Image of test section mounted to a pivoting stand such condensing flow can be recorded with the test section in horizontal (a.) and vertical (b.) orientations.

Modifications to the setup were also made to improve the level of vacuum and measurement accuracy within the system. The vacuum pump used on this setup is an Adixen 2010SD described in detail in Chapter 4. As seen in the schematic, Fig. 4-11, the vacuum lines are repositioned to pull from the system lines instead of the tanks. The test section is opened frequently to switch out the copper channel plate therefore the system required a method to remove the air from the lines prior to each experiment When pulling vacuum from both ends of a dry system, the thermocouple vacuum sensor (DV-6M, Teledyne Hastings) is able to read vacuum as low as 10 μHg. However, with liquid

drops within the lines, the vapor pressure of the room temperature water prevents the gauge from reading below 500 μHg until all the water has been vaporized and removed. To improve measurement accuracy, the pressure transducers are zeroed daily prior to testing and the thermocouples are calibrated externally before being attached into the system. Before pulling vacuum on the lines, the pressure transducers on the test section are zeroed to ambient pressure. Once the test section and lines are fully evacuated, the pump is disconnected and the valves on the tanks are opened. The offsets on the two tank transducers are adjusted until all four transducers read similar values. Additionally, the thermocouples used in the setup are calibrated using a constant temperature circulating bath (RE-207, Lauda-Brinkmann) with a thermal control of ±0.02 °C. In addition to calibration, the thermocouples and pressure sensors have been repositioned as close to the inlet and outlet of the test section as possible for sensitivity to the condensing flow. As shown in Fig. 4-18, the temperature and pressure sensors are both attached to a cross fitting (SS-400-4, Swagelok) immediately adjacent to the test section ports. The $^{1}/_{16}$" diameter thermocouples (TMQSS-062G-3, Omega) are inserted into the fitting until their tip is located mid-flow at the center of the cross.

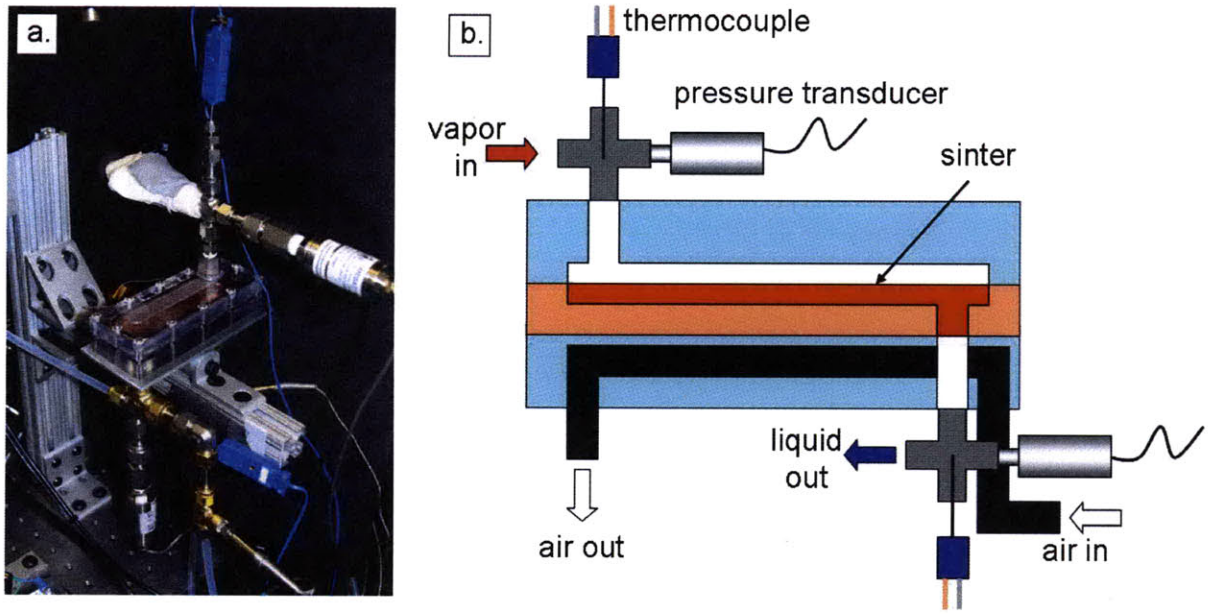

Fig. 4-18 Image (a.) and schematic (b.) of the test section illustrating the locations of the thermocouples and pressure transducers monitoring the inlet and outlet condensing flow.

System Performance

The "tabletop" system was a substantial improvement over the previous setup. The smaller footprint allowed the entire experiment to be mounted to the optical table. The reduced liquid volume and quick-disconnect features on the tanks resulted in a higher degree of water degassing. The addition of vacuum ports on the lines, the superheater, and insulation improved the vapor quality entering the test section and minimized the amount of air introduced to the system between tests. The redesign of the test section allows for improved visibility of the condensing flow and better measurement sensitivity. The new test section could also accommodate both open and sinter plates and be rotated into different gravitational orientations during testing.

All of these improvements led to better quality condensing flow results than were obtained from the first experimental setup. However, further adjustments to the system

operation were required to test under conditions similar to the heat pipe condenser. The next section will explain the minor changes that were made to this test setup.

"Heat Pipe" Experimental Setup

System Operation Modifications

As shown in the schematic in Fig. 4-19, the "tabletop" test setup was modified to function more similarly to the heat pipe condenser. All components in the condensing flow loop remained the same except for the flow control valve, which was removed. Instead of holding the hot tank to a set temperature and letting the solid state relay flash at full power, the variac on the band heater was adjusted to provide a constant input of 45 V which corresponds to about 40 W of power. This power level was chosen because it should be the power required to evaporate 0.017 g/s of water (corresponding to a flow meter measurement of 1 ccm after the test section). As shown in Fig. 4-20, the cold tank was placed within the constant temperature circulating bath used to calibrate the system thermocouples. By setting a constant temperature in the bath, the cold tank was effectively set to the saturation pressure corresponding to that temperature. If the line connecting the test section to the cold tank was completely filled with liquid, setting the pressure in the tank would essentially set the pressure at the test section outlet. In the real heat pipe, the primary wick meniscus in the evaporator adjusts to accommodate pressure drops within the loop and thereby sets the pressure on either side of the condenser. In effect, operating the loop at constant power in the hot tank and constant temperature in the cold tank similarly allows for condensing flow testing under a set pressure drop.

Also within the heat pipe, the 15 parallel condensers and dual flow paths reduce the expected flow rate within each layer to be approximately 0.01 g/s or 0.5 ccm.

However, with water backside cooling, the heat transfer rates are so large that flow rates on that order would completely condense upon entering the test section and flooding of the test section was observed. Both to extend the length of condensation and mimic the heat transfer expected from the Phump fan blades, the backside cooling was changed to compressed air.

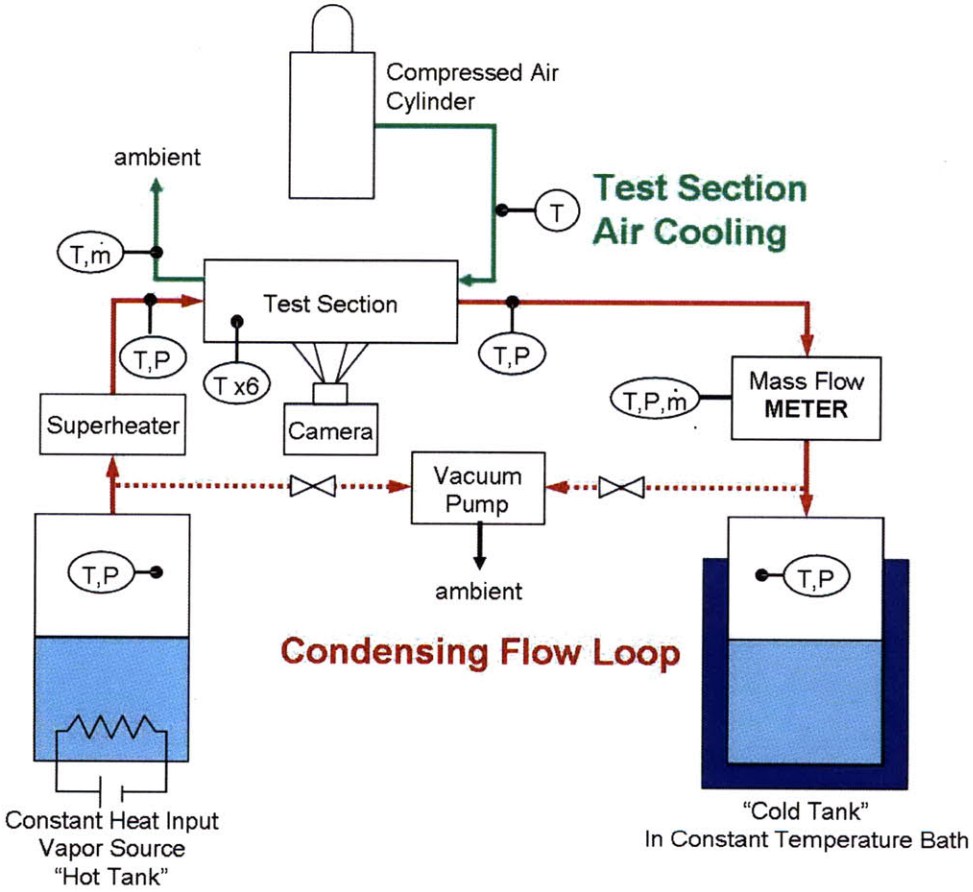

Fig. 4-19 Schematic showing the condensing flow and cooling loop implemented for the experiment to better mimic the heat pipe condenser. Major changes include the addition of air-cooling, the removal of the flow control valve, and the addition of the constant temperature bath to set the saturation condition in the cold tank.

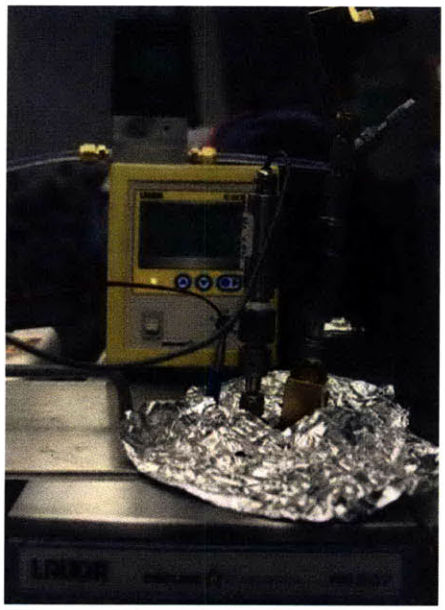

Fig. 4-20 Photograph of the cold tank sitting in the constant temperature circulating bath set to 75 °C.

Finally, to allow the test section to investigate condensing flow with a sub-cooling length, the o-ring used to seal the channel side of the test section was replaced with a silicone gasket. The entire copper plate was covered with a $^{1}/_{32}$" thick gasket with a hole cut out for the channel as shown in Fig. 4-21. To create the sub-cooling length, a $^{1}/_{16}$" thick gasket of channel width and lengths from 7 to 20 mm was laid over the sinter in the channel and compressed into place. Results from condensing flow in this test setup will be described in Chapter 5.

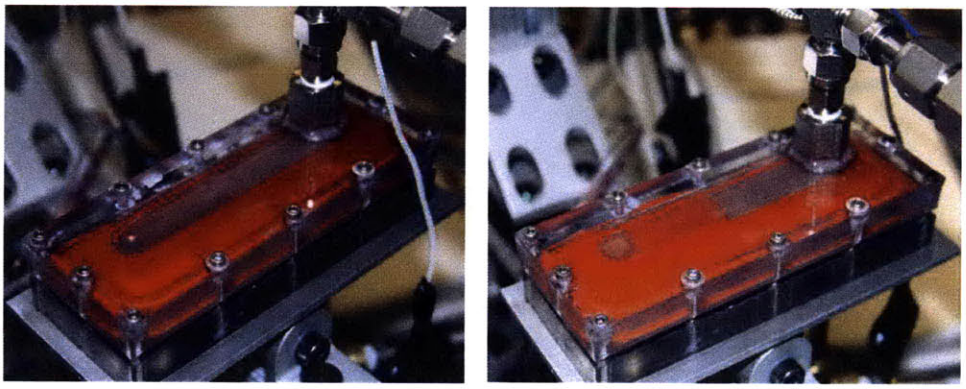

Fig. 4-21 Images of the test section showing silicone gasket used in place of the o-ring for vacuum sealing and to create a sub-cooling section for testing plates with sinter.

Chapter 5: Condensing Flow Experiments

Overview

This section describes experimental work to investigate condensing flow within geometries similar to the loop heat pipe condenser design. Experiments were performed with an open channel while varying flow rate, backside cooling temperature, and gravitational orientation. Open channel testing exhibited a condensing length beyond which the temperature of the fluid decreased and a sensitivity to orientation resulting in an unstable interface when gravity acted opposite the flow direction. In comparison, testing in channels with sintered wick demonstrated suppression of flow patterns, isothermal surface temperatures, and phase separation regardless of orientation. Finally, experiments were performed with a sub-cooling length to force condensate to drop below saturation conditions before reaching the test section outlet. These experiments showed temperature reduction under low condensing flow rates and air-cooling similar to the real condenser design. Future work will investigate the placement of condensers in parallel with a gravity head in between to study flow distribution and flooding failure modes.

Open Channel Flow Testing

The first step in validating the condenser design is to understand how condensing flow behaves in an open channel without wick. The geometry of the channel is designed to mimic the flow in the interior of the flat plate parallel condensers. The dimensions of the channel are 1 mm depth, 13 mm width, and 80 mm length. These experiments are performed in the "tabletop" setup using water degassed by helium sparging. The condensing flow is imaged through the polycarbonate top plate as depicted in Fig. 5-1.

The vapor flow enters from the inlet on the left and condenses as droplets on the copper plate. An interface is formed at the condensing length when the vapor has completely condensed and downstream is filled with liquid. The condensed liquid exits through the outlet on the right. Bubbles in the liquid flow indicate the presence of non-condensable gases (NCGs) in the working fluid reservoirs due to incomplete deaeration. In the course of this open channel flow testing, condensing flow rate and backside cooling temperature were varied to understand their effect on condensing length. Additionally, gravitational orientation was varied to understand its effect on flow stability and pressure drop.

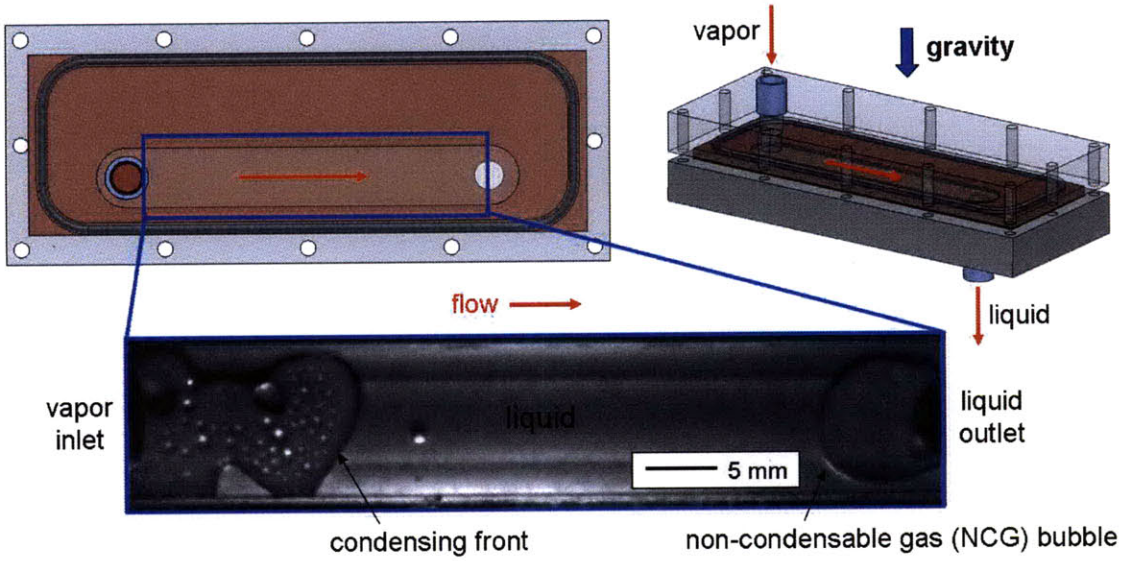

Fig. 5-1 Example image of condensing flow inside an open channel geometry in a horizontal orientation.

Condensing Flow Patterns

Two-phase flow inside open channels has been studied for decades, primarily focusing on visualization and flow pattern mapping within round tubes [27]. The broad two-phase category includes flow under adiabatic conditions such as gas/liquid mixtures and diabatic conditions such as the condensing flow studied in this thesis. During condensing flow in a capillary tube, the flow regimes transition as shown in Fig. 5-2.

Initially vapor condenses on the circumference of the cool wall and an annulus of liquid is formed. As vapor continues to condense on the liquid layer, collars are formed that grow in size until they bridge across the diameter of the tube. The relative size of the vapor core compared to the liquid volume designates the slug, plug and bubble regimes. Larger diameter tubes also may experience stratified flow where the vapor and liquid form separate vertical layers due to the influence of gravity.

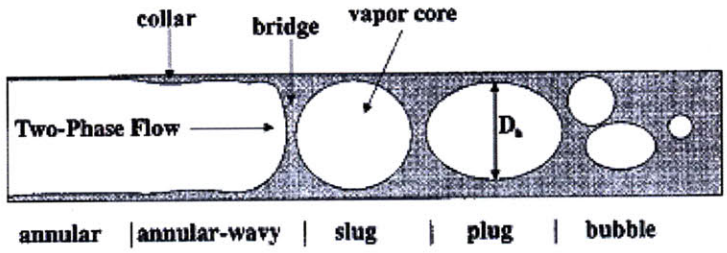

Fig. 5-2 Illustration of flow regime transition during two-phase condensing flow within capillary horizontal tubes [16].

The work by Tabatabai *et al* suggests that condensing flow in tubes with millimeter scale diameters experiences flow regimes that are influenced by surface tension. As shown in Fig. 5-3, they propose a pattern map where the ratio of superficial velocities (velocity of each phase) is plotted as a function of the ratio of pressure drop due to surface tension divided by pressure drop due to shear. Fig. 5-4 shows flow pattern mapping as a function of hydraulic diameter for the dimensions and flow rates anticipated for the heat pipe condenser; The Matlab code used to generate the graph is given in Appendix C. By comparison with the graphs in Fig. 5-3, a channel of this hydraulic diameter will experience slug and plug flow when cooled from both sides. Although the hydraulic diameter is on the order of the channel depth, the width is 20 times larger. Therefore flow visualization is required to define flow regimes in this high aspect ratio geometry.

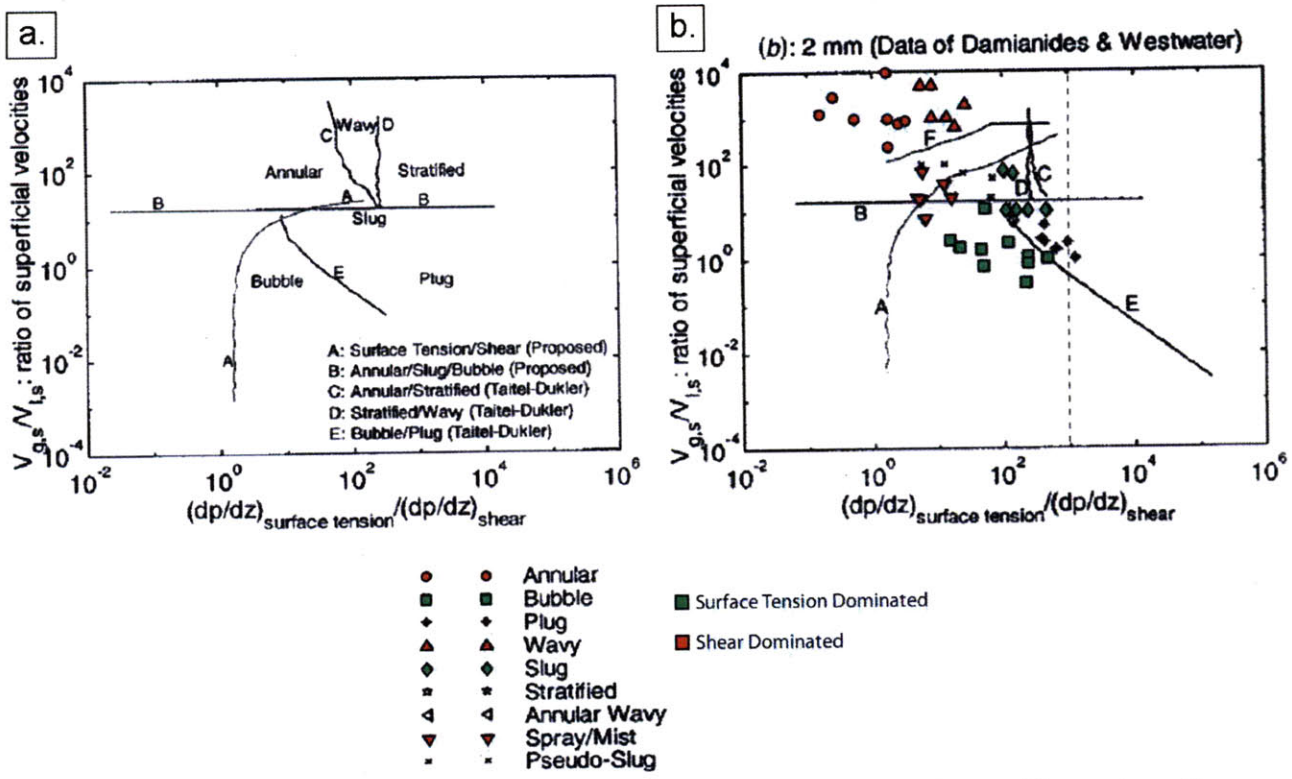

Fig. 5-3 Flow regime mapping suggested by Tabatabai *et al* [16] along with overlay of data for a tube diameter matching the hydraulic diameter of the condenser interior.

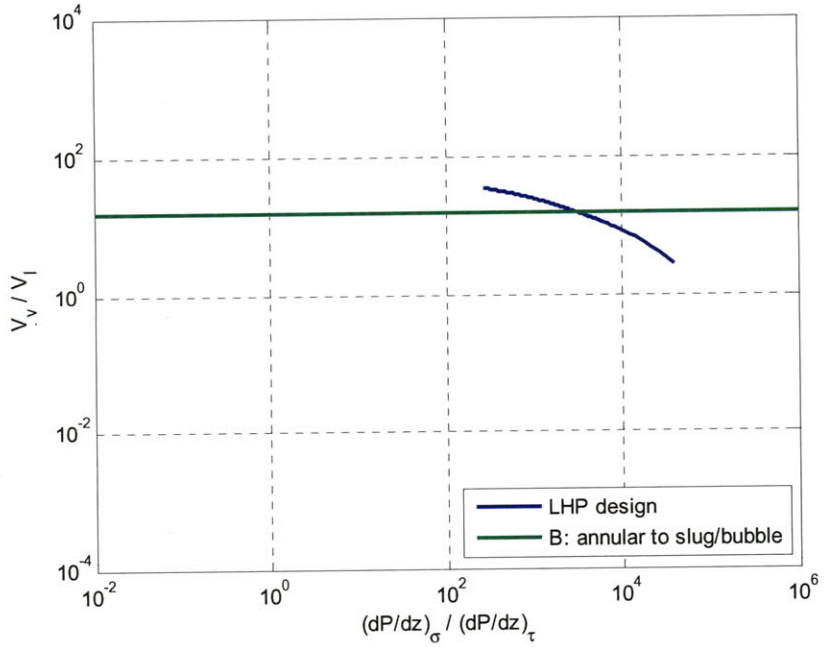

Fig. 5-4 Graph showing anticipated flow regime transitions for open channel flow within the loop heat pipe geometry. Graph should be compared to ref. [16] to conclude that regimes are always slug and plug.

Dimensionless Correlations

For these experiments, a few preliminary calculations were done to understand the tradeoffs of surface tension, inertia and gravity within this channel geometry. Fluid properties are taken from RefProp [24]. The Weber number, shown in Eqn. 5.1, was used to investigate the relative influence of inertia versus surface tension on a condensed droplet in a horizontal channel.

$$We = \frac{\rho_v v^2 L}{\sigma} = \frac{\dot{m}^2 L}{\rho_v \sigma A^2} \tag{5.1}$$

For incoming water vapor at 80 °C, the density (ρ_v) is 0.294 kg/m^3 and the surface tension (σ) of the condensed liquid is 0.062 N/m. The characteristic length (L) was chosen as the channel depth of 1 mm, but using the hydraulic diameter of 1.86 mm will yield similar results. The cross sectional area (A) was 1 mm depth by 13 mm width. For liquid flow rates ranging from 5 – 15 ccm, the mass flow rate ($\dot{m}$) ranges from 8.3 x 10^{-5} to 2.5 x 10^{-4} kg/s and therefore the vapor velocity (v) ranges from 22 – 65 m/s, using $v = \dot{m} / \rho_v A$. For this geometry, the Weber number ranges from 2 – 20 indicating that condensed droplets will be pushed by vapor inertia instead of held in place by surface tension for all flow rates.

The Bond number, calculated by Eqn. 5.2, was used to investigate the relative influence of gravity versus surface tension on a condensed droplet inside a vertically oriented channel.

$$Bo = \frac{\rho_l g L^2}{\sigma} \tag{5.2}$$

For a droplet condensed at 80 °C, surface tension is the same as before and the liquid density (ρ_l) is 971.77 kg/m^3. The characteristic length (L) was again the channel depth.

Gravity (g) was the standard 9.81 m/s^2. For this geometry, the Bond number was 0.15 indicating that surface tension should dominate over gravity to keep a condensed drop stationary. However, this calculation inherently assumes that the drop diameter is approximately the characteristic length, the 1 mm channel depth. For this experimental setup, the Bond number becomes 1 for L > 2.6 mm. However, because the liquid-vapor interface can fill the width of the channel as droplets grow, the modified Bond number given in Eqn. 5.3 could better represent the influence of this geometry.

$$Bo = \frac{drop\ weight}{surface\ tension\ force} = \frac{\rho_l g V}{\sigma P} \approx \frac{\rho_l g R L}{\sigma} \tag{5.3}$$

The drop volume (V) is $\pi R^2 L$ and the perimeter (P) is $2\pi R$. For a droplet forming a cylinder between the channel and the viewing plate with a radius (R) of 6.5 mm (half the channel width) and a depth (L) of 1 mm, the modified Bond number is 1. Thus both gravity and inertia can influence the liquid motion. In summary, when the open channel is oriented vertically, small droplets will have a high enough surface tension force to overcome gravity, but as the drops grow to fill the width of the channel, gravity will prevent the liquid from being held in place by surface tension.

The Froude number was used to investigate the relative influence of inertia versus gravity on a condensed droplet inside a vertically oriented channel. The characteristic length (L) was equal to the channel depth of 1 mm and vapor velocities (v) ranged from 22 – 65 m/s as calculated for the Weber correlation. The standard Froude calculation shown in Eqn. 5.4, resulted in Froude numbers in the 10^5 range implying the inertia by far dominates gravity.

$$Fr = \frac{v^2}{gL} \tag{5.4}$$

The Froude relation can also be rewritten as a shown in Eqn. 5.5 as the balance of vapor pushing the drop to the drop weight.

$$Fr = \frac{force\ pushing\ drop}{drop\ weight} = \frac{\rho_v v^2 A}{\rho_l g V} = \frac{\rho_v v^2}{\rho_l g R} \tag{5.5}$$

For a drop sandwiched into a cylinder shape between the channel and the viewing plate, the surface area of the drop is calculated as $A=2\pi RL$ and the volume as $V= \pi R^2 L$ for a drop radius (R) of 6.5 mm (half the channel width) and a depth (L) of 1 mm. For the vapor flow, the density (ρ_v) is 0.294 kg/m^3 and, for the gravity component, the liquid density (ρ_l) is 971.77 kg/m^3. Using Eqn. 5.5, the Froude numbers range from 2 – 20 reinforcing, but with a much slimmer margin, that inertia influences the flow more than gravity for liquid flow rates of 5 – 15 ccm. However, if the flow rate is reduced to 1 ccm at a corresponding velocity of 4.4 m/s, the Froude number is 0.01. These results imply that high condensing flow rates will enable inertia to dominate gravity, however at the low flow rates expected in the real device, gravity will dominate the flow pattern.

Horizontal Flow Testing

The first experimental testing was completed with the test section oriented horizontally while varying flow rate and backside cooling temperature. As shown in Fig. 5-5, when backside cooling is held at a constant temperature, condensing length increases with increasing flow rate. The condensing length is denoted by the colored vertical lines at the last active vapor condensation location. For 15 ccm, a condensing length is not shown because the vapor does not completely condense in the channel. The graph in Fig. 5-6 shows the temperature profile of the channel as recorded by the thermocouples imbedded in the copper plate. The vertical lines illustrate that the condensing length

occurs at the point of sharp temperature drop in the condensing flow. Additionally, the temperature plot of the 15 ccm flow shows that an isothermal surface can only be obtained in open channel flow when the entire length is used for condensation.

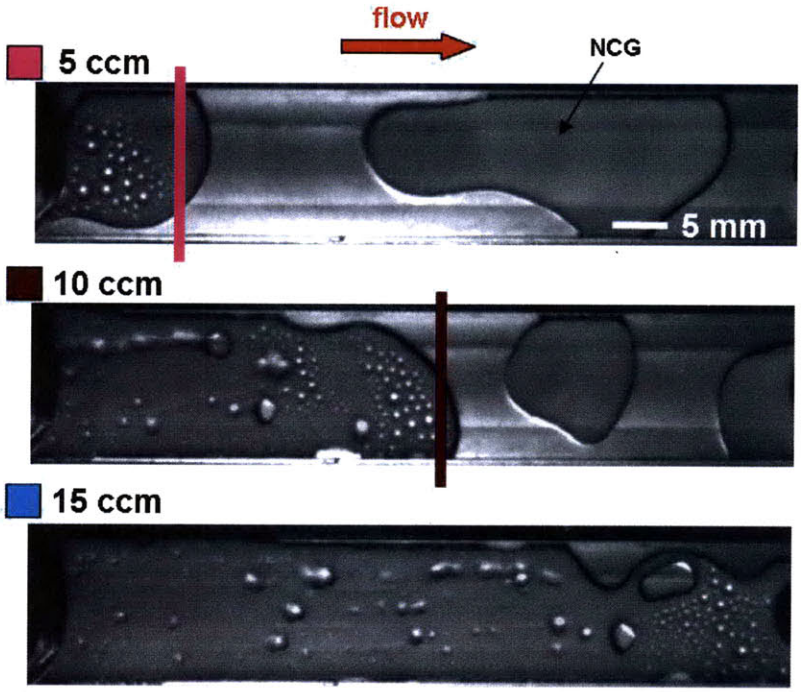

Fig. 5-5 Comparison of horizontal condensing flow with 50 °C backside cooling for increasing flow rates. The vertical lines indicate the condensing lengths.

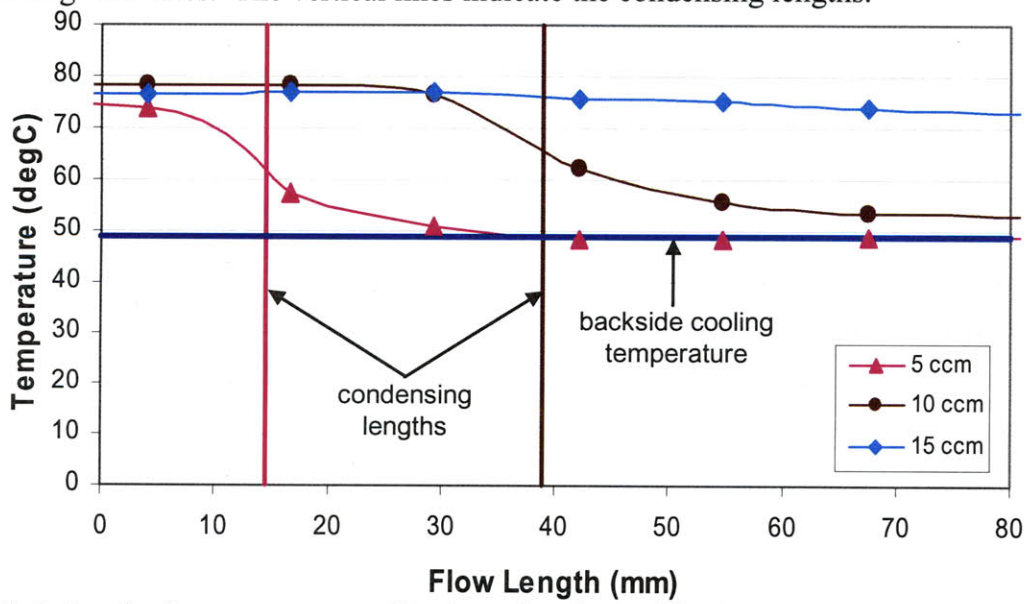

Fig. 5-6 Graph of temperature profile along the channel for horizontal flow with 50 °C backside cooling. For 5 and 10 ccm, condensing lengths occur at locations of sharp drop in temperature profile. For 15 ccm, the flow is almost isothermal because complete condensation does not occur in the channel.

For these images and temperature plots, the water backside cooling has an inlet temperature of 50 °C and an average flow rate of 1950 ccm. The quoted flow rate is for the condensed liquid flow; mass flow is constant within the system therefore the vapor flow rate will be 3300 times the liquid flow rate in ccm. The total flow length in the condensing channel is 80 mm and the channel cross section is 1 mm depth by 13 mm width. The temperature in the hot tank is set to 85 °C such that the vapor is 80 °C at the thermocouple preceding the test section inlet. To determine the heat transfer provided by the backside water cooling, first the Reynolds number was calculated with Eqn. 5.6.

$$\mathrm{Re}_{Dh} = \frac{\rho_w v D_h}{\mu_w} = \frac{\dot{m}_w D_h}{\mu_w A} \tag{5.6}$$

The backside heat exchanger has a hydraulic diameter (D_h) of approximately 2 mm and a cross sectional area (A) of 1 mm by 26 mm. The 1950 ccm flow rate converts to a mass flow rate ($\dot{m}_w$) of 0.033 kg/s. The 50 °C water has a density (ρ_w) of 988.04 kg/m^3, a viscosity (μ_w) of 546.85 μPa-s, a Prandtl number (Pr_w) of 546.85, and a conductivity (k_w) of 0.644 W/m-K. The Reynolds number as a function of hydraulic diameter was 4640 for this geometry indicating that the liquid flow is turbulent. The Nusselt correlation applied for turbulent flow was Gnielinski's formula in Eqn. 5.7.

$$Nu_{Dh} = \frac{h_{cool} D_h}{k_w} = \frac{(f/8)(\mathrm{Re}_{Dh} - 1000)\,\mathrm{Pr}_w}{1 + 12.7(f/8)^{1/2}(\mathrm{Pr}_w^{2/3} - 1)}\ ;\ \mathrm{Re} > 3000 \tag{5.7}$$

The Nusselt number was 28.9 using a friction factor (f) of 0.04 which resulted in a corresponding heat transfer coefficient (h_{cool}) for the water cooling of 9311 W/m^{2}K.

Using this cooling heat transfer coefficient, a condensing length (L_{cond}) for these open channel flows can be determined analytically from the heat transfer balance shown in Eqn. 5.7.

$$Q_{cond} = \dot{m}h_{fg} = h_{cool}WL_{cond}(T_{wall} - T_{water}) \tag{5.7}$$

Under ideal conditions, the incoming vapor is saturated steam with a quality of 1. The heat that must be removed to condense the steam is given by $Q = \dot{m}h_{fg}$, where the latent heat (h_{fg}) is 2308 kJ/kg. The channel plate (T_{wall}) is assumed to be at the vapor temperature, 80 °C, due to the high heat transfer coefficient typically associated with condensation (10,000-300,000 W/m^{2}K). The incoming backside cooling (T_{water}) is 50 °C and the channel width (W) is 13 mm. For 5, 10 and 15 ccm, the mass flow rates ($\dot{m}$) will be respectively 8.3 x 10^{-5}, 1.67 x 10^{-4}, and 2.5 x 10^{-4} kg/s. If the backside cooling absorbs all of the phase-change heat transfer, the condensing lengths will be respectively 58, 108, and 167 mm.

Fig. 5-6 shows that the real condensing length for 5 ccm is 15 mm, for 10 cm is 39 mm, and for 15 ccm is greater than the 80 mm channel length. Therefore, clearly the calculation is overestimating the condensing length. If the vapor is partially condensed when it enters the test section, a better estimate of the heat transfer during condensation would be Eqn. 5.8, which uses the change in temperature of the backside cooling.

$$Q_{cool} = \dot{m}_w c_{p,w}\Delta T_w = h_{cool}WL_{cond}(T_{wall} - T_{water}) \tag{5.8}$$

The specific heat of the water ($c_{p,w}$) is 4181 J/kgK and the change in temperature of the backside cooling (ΔT_w) is 0.8-2.2 °C. For the flows in this experiment, the ratio of Q_{cool}/Q_{cond} was on average 0.55 confirming that almost half of the heat associated with condensing the steam is lost to the surroundings, rather than transferred to the backside

cooling fluid. Using Eqn. 5.8, the calculated condensing lengths are 31, 61 and 87 mm. While these values are closer to the actual condensing lengths, the values are still over estimates.

The heat transfer coefficient (h_{cool}) was calculated using Eqn. 5.7 as an average value for the entire surface assuming fully developed flow. In the case of this heat exchanger, the hydrodynamic and thermal entry lengths are far longer than the test section, making the backside cooling developing flow. Additionally the cooling flow makes a sharp 90° turn at the inlet as it exits the liquid tubing and enters the heat exchanger. As seen in Fig. 5-7, turbulent flow with this entrance geometry can experience a heat transfer coefficient 2.5 times the downstream average coefficient. This increase in heat transfer may potentially explain why the measured condensing length was shorter than anticipated analytically.

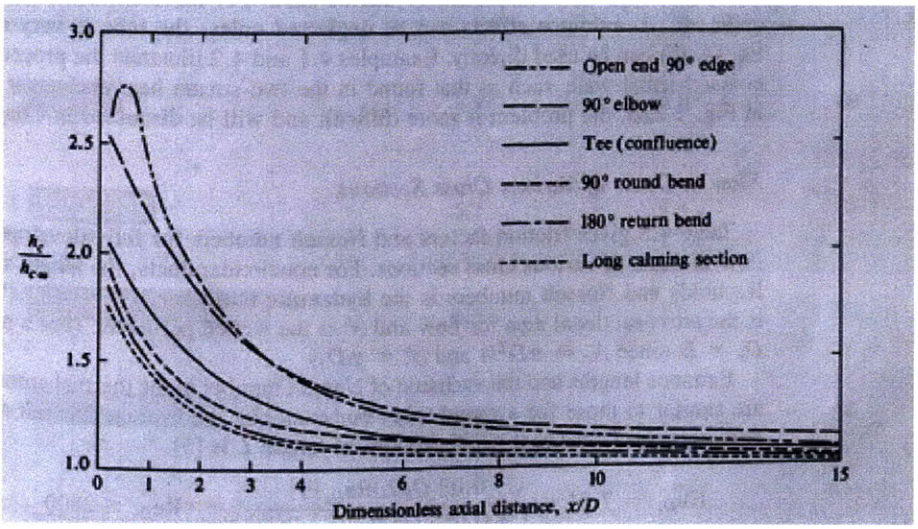

Fig. 5-7 Entrance region heat transfer for turbulent flows with various entrance configurations. $h_{c,\infty}$ is the heat transfer coefficient far from the entrance, x is the distance from the start of heating, and D is the tube diameter [25].

The same equations from the previous analysis also conclude that for constant flow rate, condensing length increases with increasing the backside cooling temperature

as is shown in Fig. 5-8. For these experiments, the flow rate was set to 10 ccm and flow was observed for 30, 50 and 70 °C backside cooling. The graph in Fig. 5-9 shows that after the condensing length, the thermocouple readings drop to match the temperature of the backside cooling unless the flow does not condense completely as in the 70 °C scenario. When compared, the thermocouples under the condensed liquid are typically within 5 °C of the thermocouple at the outlet of the test section. These results suggest that the slow liquid flow combined with the high backside heat transfer can cause rapid subcooling after condensation. Alternatively, beyond the condensation length, the thermocouples could be more sensitive to the backside temperatures. Under the condensing front, the condensation heat transfer coefficient can be on the order of 10,000-300,000 W/m^{2}K and therefore the embedded thermocouples would be more sensitive to the condensing flow. However, once condensed, the liquid velocity is only 0.65 – 2 cm/s resulting in low Reynolds number laminar flow. Using the Nusselt number correlation in Eqn. 5.9,

$$Nu_{Dh} = \frac{hD_h}{k} = 3.66 + \frac{0.065(D_h/L)\,\mathrm{Re}\,\mathrm{Pr}}{1 + 0.04[(D_h/L)\,\mathrm{Re}\,\mathrm{Pr}]^{2/3}};\ \mathrm{Re} < 2300, \qquad (5.9)$$

the heat transfer coefficients are approximately 1200 W/m^{2}K on the front side of the channel. The heat transfer coefficient of 6,000-12,000 W/m^{2}K on the backside will be the lower thermal resistance and therefore the thermocouple will be more sensitive to the backside cooling temperature.

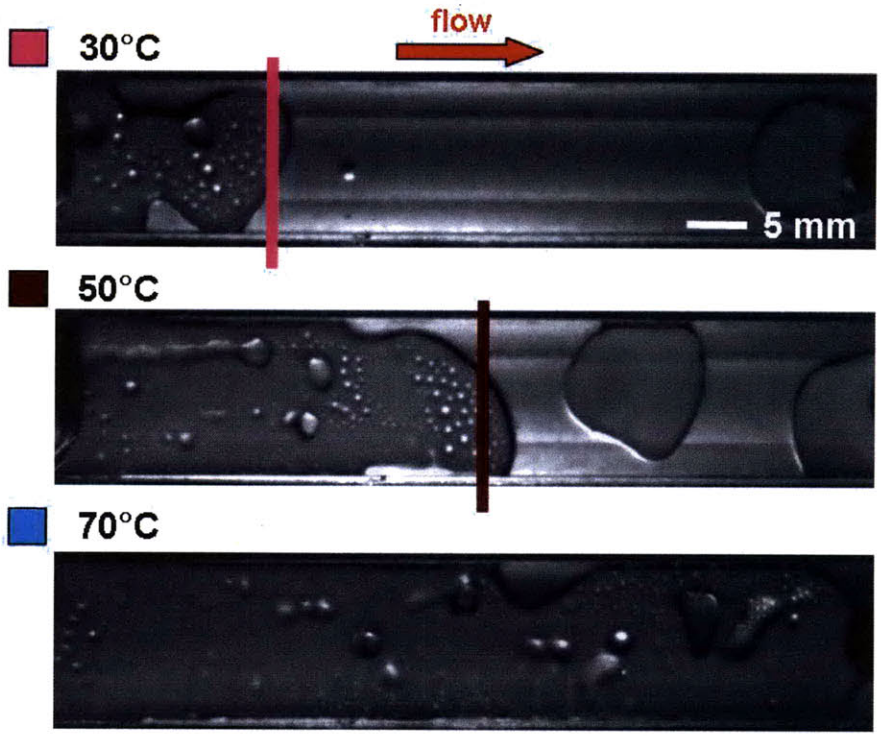

Fig. 5-8 Comparison of horizontal condensing flow at 10 ccm flow rate for increasing backside cooling temperature. The vertical lines indicate the condensing lengths for each temperature; the condensing length for 70 °C is not shown because it is longer than the channel.

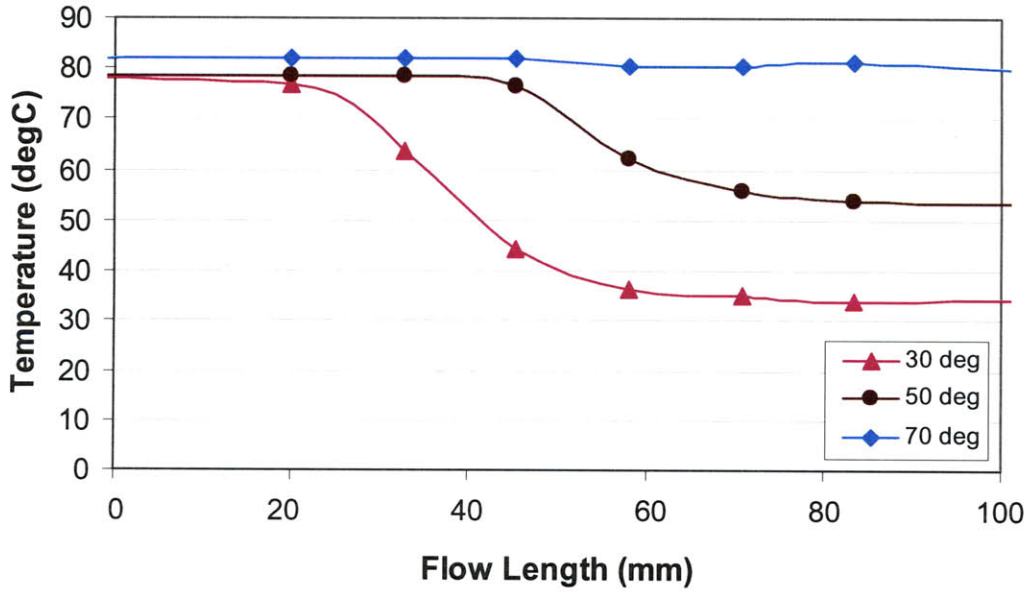

Fig. 5-9 Graph of temperature profile along the channel for horizontal flow at 10 ccm flow rate with backside cooling temperatures of 30, 50 and 70 °C. When the flow condenses completely, the temperature of the condensing flow drops until it reaches the temperature of the backside cooling as shown in the 30 and 50 °C cases. However, if the flow has not completely condensed as in the 70 °C case, the channel may remain isothermal.

Testing With Varying Gravitational Orientation

In addition to varying flow rate and backside cooling temperature, experiments were also conducted to investigate the effect of gravitational orientation on the condensing flow. As shown in Fig. 5-10, 10 ccm condensing flow with 50 °C backside cooling was observed in horizontal and both vertical orientations. The horizontal flow displays the characteristic condensing length described in the previous sections. In contrast, the orientation with gravity opposing the flow direction results in an unstable, churning liquid-vapor interface. The instability appears to be caused by liquid backflow toward the inlet under the influence of gravity. This flow pattern upholds the Bond number analysis that suggests that gravity will dominate surface tension in the condensed liquid sheet near the outlet allowing it to recirculate to the inlet. Additionally, the ability of the churning front to change shape and even force its way to the outlet upholds the Froude number analysis that suggests that vapor inertia should be able to overcome gravity at these flow rates. With gravity acting in the flow direction, the vapor condenses as small drops on the surface. These condensed droplets grow on the surface until they contact the side walls and fall in streams toward the bottom outlet. This flow pattern upholds the Bond number analysis that suggests that surface tension will keep small drops stationary, however once the drops grow in size, gravity can overcome surface tension causing the drops to fall toward the outlet.

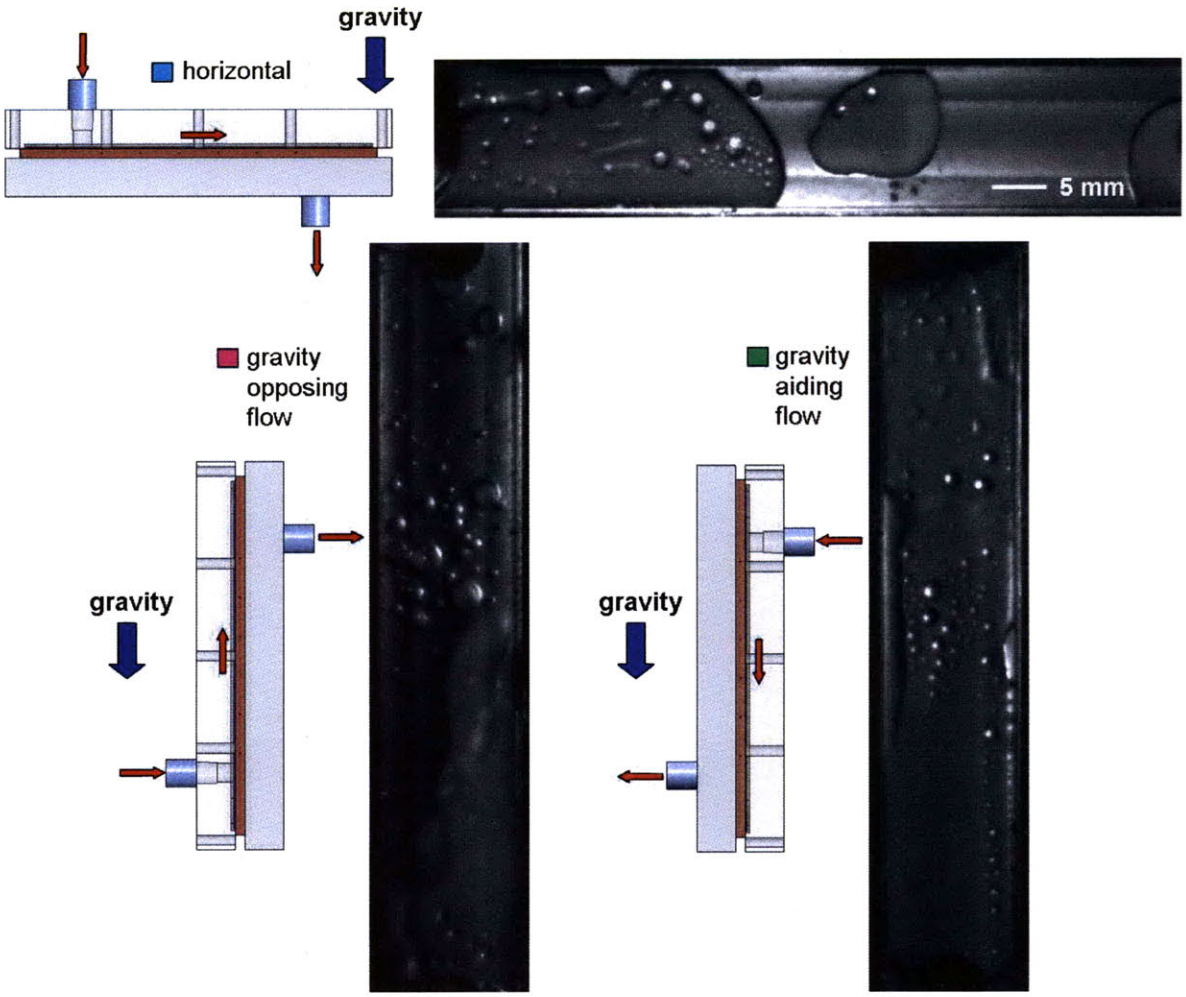

Fig. 5-10 Images of 10 ccm condensing flow with 50 °C backside cooling under varying gravitational orientation.

Finally, the pressure drops for the condensing flow were measured using a differential pressure transducer for 5, 10 and 15 ccm in all three gravitational orientations. As shown in the graph in Fig. 5-11, pressure drop increases with increasing flow rate as expected since viscous losses scale with velocity. Additionally, the gravitational head of a liquid column creates a pressure difference such that there are larger pressure drops in the case of flow against gravity than in the horizontal case. The average pressure difference between horizontal and against gravity is 0.5 kPa. An 80 mm gravity head of liquid can generate a pressure drop of 760 Pa and therefore a slightly

shorter head could have caused the pressure difference. Conversely, the case of flow with gravity lacks a downstream pool of liquid, so condensed drops can stream unimpeded to the outlet resulting in pressure drops much lower than horizontal.

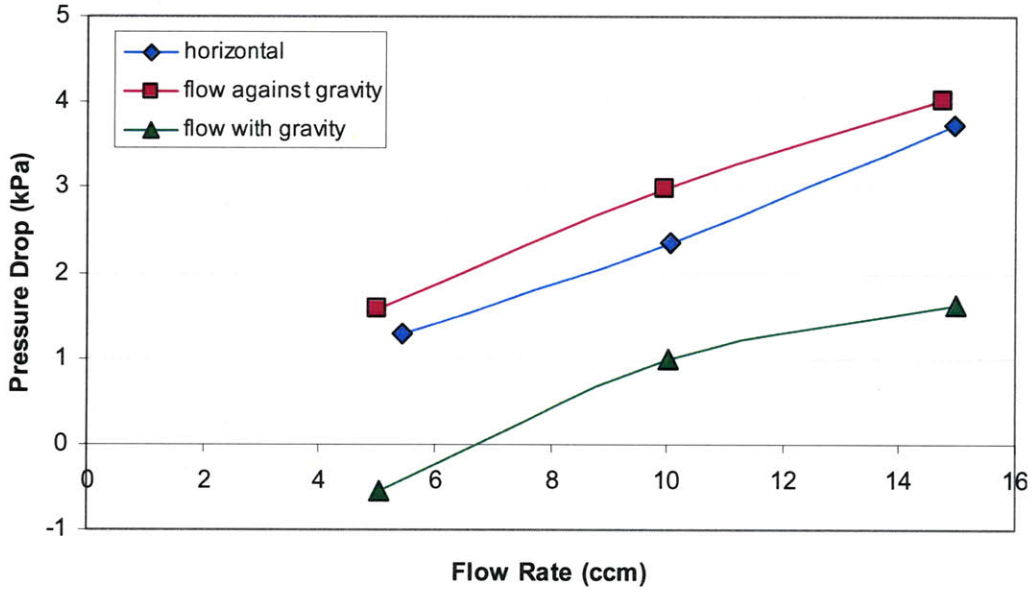

Fig. 5-11 Graph of pressure drop (kPa) vs. liquid flow rate (ccm) for different gravitational orientations. Data was taken at 5, 10 and 15 ccm with 50 °C liquid backside cooling.

The pressure drop in the horizontal orientation can be calculated analytically using the condensing length (L_{cond}) measured during the previous experiments and Eqn. 5.10.

$$\Delta P = \frac{32\,\dot{m}}{D_h{}^2 A}\left[\left(\frac{\mu_v L_{cond}}{\rho_v}\right)+\left(\frac{\mu_l (L - L_{cond})}{\rho_l}\right)\right] \tag{5.10}$$

For laminar flow, the friction factor is f=64/Re. The fluid properties used in the calculation were the following: vapor viscosity (μ_v) of 11.592 μPa-s, vapor density (ρ_v) of 0.294 kg/m^3, liquid viscosity (μ_l) of 354.33 μPa-s, and liquid density (ρ_l) of 971.77 kg/m^3. The total channel length (L) was 80 mm, the hydraulic diameter (D_h) was 2 mm, the cross

sectional area (A) was 1 mm x 13 mm, and the mass flow rates were the same values used in previous calculations.

The pressure drops for 5, 10 and 15 ccm with respective condensing lengths of 15, 39 and 80 mm were 0.138, 0.661 and 1.815 kPa. However, the measured pressure drops of 1.3, 2.3 and 3.7 kPa are substantially higher. The calculation in Eqn. 5.10 does not take into account minor losses associated with changes in the flow direction and sharp edged entrances and exits, which may explain some of the higher-than-expected pressure drop. In addition, the differential pressure transducer is attached across the test section using 1/6" stainless steel capillary tubes. The pressure reading could be off by 200 Pa due to surface tension effects if there is air trapped in the capillary line or a liquid vapor interface at the entrance to the capillary tube. In later testing, the differential pressure transducer was replaced by absolute pressure transducers that could be mounted directly on vapor and liquid flow lines.

The open channel flow in this testing was dimensioned similar to the condenser design. The conclusions from this testing could be expanded by allowing cooling from both sides of the channel and comparing flow regimes and pressures drops to flow maps in literature [16]. Broader future work on this type of open channel flow could vary geometry to investigate its influence on flow pattern and gravitational stability. For example, two-phase flow in millimeter-scale square cross-section tubes has been studied in literature [28]. By varying aspect ratio of the channel, the limit for when the square flow patterns apply can be determined and trends for flow patterns beyond this limit can be defined. Additionally, the channel depth can be varied during vertical flow to investigate when the gravity instability is overcome by surface tension.

Sinter Channel Flow Testing

In open channel flow testing, it was observed that condensing length varied with condensing flow rate and backside cooling temperature. Additionally, the flow pattern was substantially affected by gravitational orientation. Applying these findings to the condenser design, the flow rate and hence the heat transfer into each condenser would have to be perfectly balanced with the heat removed by air-cooling to maintain an isothermal surface with condensation along the full length. If the air-cooling is too high or the flow rate too slow, the vapor will form a condensing length with the plate under the downstream liquid substantially lower in temperature. If the air-cooling is too low or the flow rate too fast, the vapor will be able to reach the liquid return line before condensing completely. Additionally because the flow pattern varies substantially with orientation, it would not be possible to design an open channel condenser of this geometry with stable, predictable operation regardless of mounting orientation.

As described in Chapter 2, it was hypothesized that lining the condensation surfaces of the plates with sintered wick will result in a more robust design than the open channel. As vapor condenses on the sintered surface, the wick should absorb the liquid and create an interface separating the liquid and vapor phases. This design was tested experimentally using the "tabletop" test setup and water degassed by FPT cycling. The backside cooling was circulated water. The wick was formed by loose sintering 40-90 μm copper powder, shown in the SEM in Fig. 5-12, directly in the copper channel plates using an atmosphere controlled tube furnace (Lindberg-Blue HTF55667C). A reducing atmosphere of 5% H_2, 95% N_2 was used to remove surface oxidation from the copper particles and prevent any additional oxidation during the sintering process. The furnace

was heated at a rate of 20 °C/min and the plates were sintered at 850 °C for 30 min [26]. After sintering and between tests the plates were stored in a desiccator under a nitrogen atmosphere. Prior to testing, the sinter plates were plasma cleaned for an hour. After testing and prolonged exposure to air, there were indications that the surface turned hydrophobic. The plasma cleaning appeared to restore the wicking capability of the sinter however it is uncertain whether the improvement was only at the wick surface or throughout its volume.

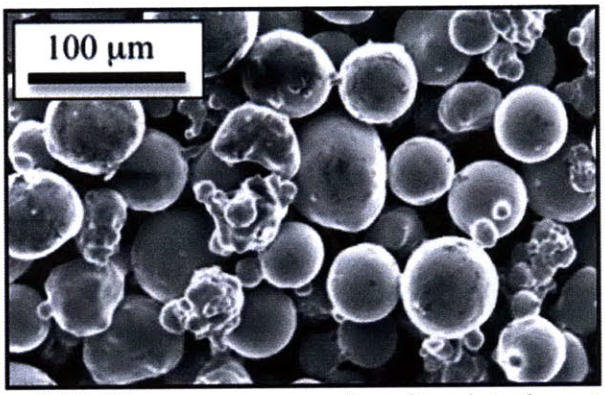

Fig. 5-12 SEM image of 40-90 μm copper powder after sintering at 850 °C for 30 minutes [1][26].

As shown in Fig. 5-13, at 4 ccm and 65 °C backside cooling, there is a characteristic condensing length of 53 mm in the open channel. For the same flow conditions, the channel filled with 40-90 μm copper sinter suppresses the flow pattern and all that is seen is a vapor fog across the entire polycarbonate viewing plate. The small droplets are on the polycarbonate and not in contact with the sinter surface. The temperature profile in Fig. 5-14 shows that the open channel has a sharp drop of 8 °C after the condensing length. In contrast, the sinter is able to maintain an isothermal surface across the entire plate with temperature fluctuations of less than 2 °C. As shown in Fig. 5-15, when the test section is oriented vertically with gravity opposing the incoming vapor flow, the open channel displays an unstable churning front due to liquid

backflow. The image of the sinter channel however is completely static in the pictured condition. A vapor fog connects the inlet to the outlet and the dark spots are slugs of liquid trapped between the viewing plate and the sinter surface. The gravitational force and surface tension force acting on the slugs of liquid can be compared in order to confirm that it is reasonable for surface tension to keep the slugs in place. Revisiting the modified Bond number analysis from the previous section and assuming that the trapped slug is approximately 5 mm in width, 30 mm in length, and the same thickness as the vapor space, 0.5 mm, the liquid slug volume is 75 mm^3. Assuming that surface tension acts on the 3 sides in the channel for a perimeter of 40 mm, the modified Bond number using Eqn. 5.3 is 0.29 validating that surface tension could hold the slug in place despite the vertical orientation.

From the comparison of open and sinter channel flow testing it can be concluded that sinter is able to suppress flow patterns under horizontal and vertical orientations. In addition, covering the plate with sinter encourages condensation over the entire surface leading to an isothermal plate temperature.

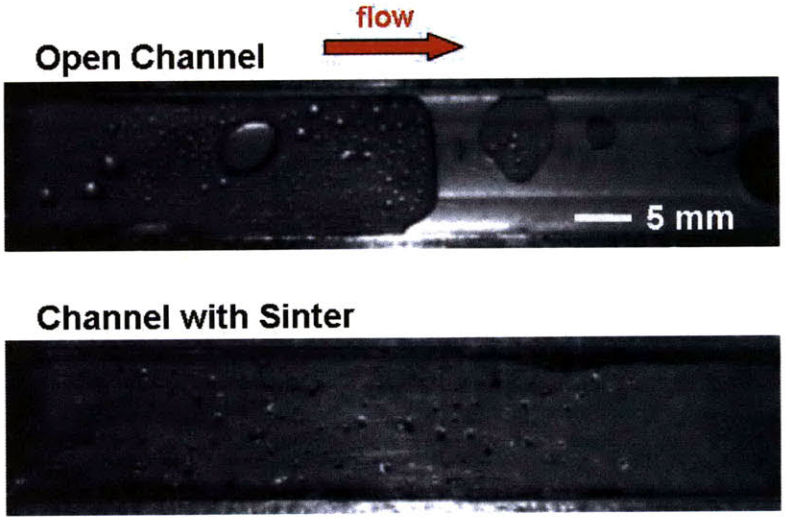

Fig. 5-13 Comparison of horizontal condensing flow at 4 ccm with 65 °C backside cooling in an open channel and a channel with 40-90 μm sinter.

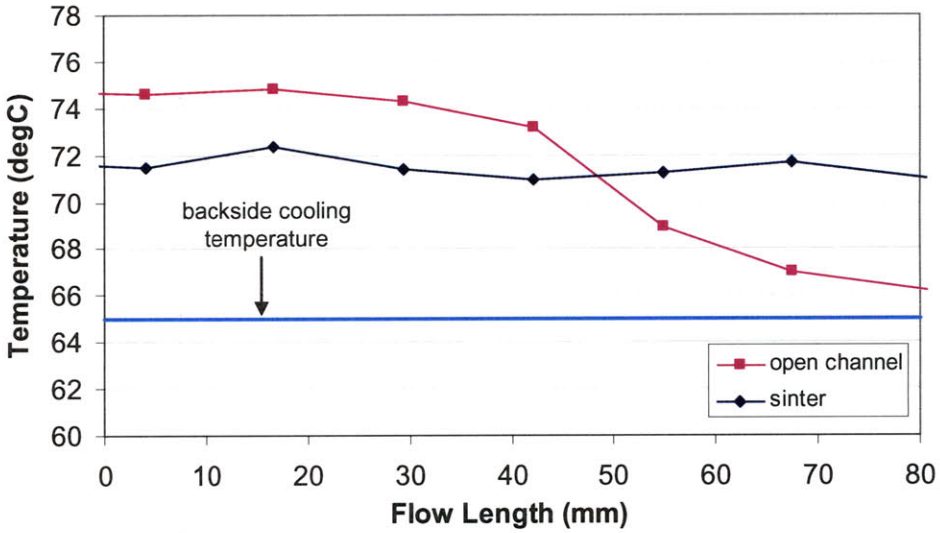

Fig. 5-14 Graph of temperature profile along the channel for horizontal flow at 4 ccm with 65 °C backside cooling. For the open channel, the temperature profile sharply declines at the condensing length. However, the sinter filled channel under the same conditions maintains an isothermal temperature profile. Error is estimated as ±1 °C.

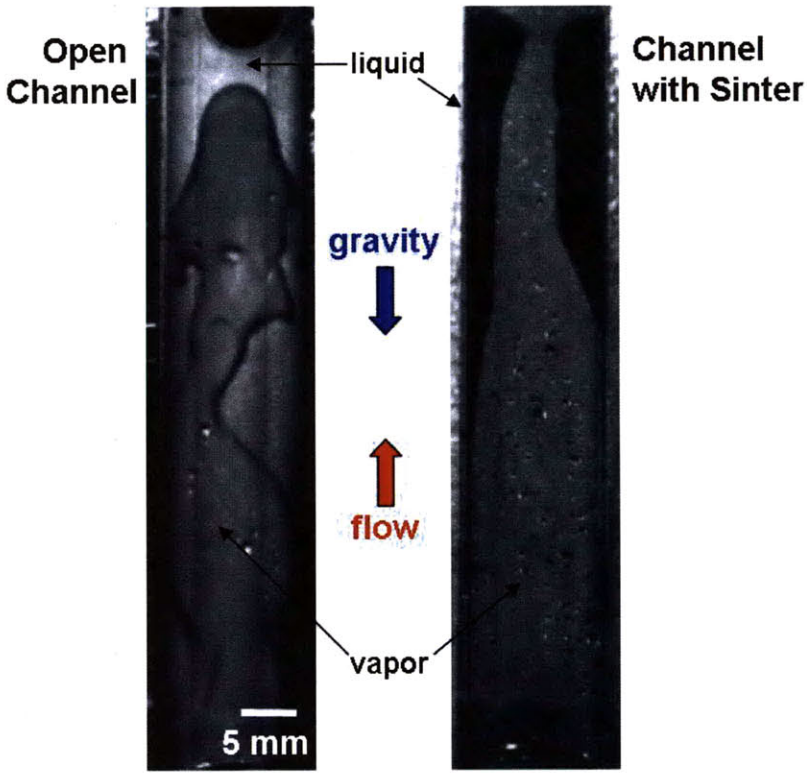

Fig. 5-15 Comparison of vertical condensing flow at 4 ccm with 65 °C backside cooling in an open channel to a channel with 40-90 μm sinter.

Including sinter in the condenser has advantages in terms of flow stability, but this stability comes at the cost of added pressure drop. The sinter has a higher viscous pressure drop due to the liquid flowing through the porous wick and an additional capillary pressure drop due to the meniscus at the wick surface. For the 4 ccm horizontal flows shown in Fig. 5-13, the open channel had a pressure drop of 0.2 psi or 1.4 kPa. In comparison, the flow with sinter had a pressure drop of 1.4 psi or 9.5 kPa, over 6 times higher than the open channel. To understand results for the sinter, the pressure drop can be calculated analytically for flow through the vapor channel and the wick. The 40-90 μm sinter has an average particle size (D) of 65 μm. Assuming the sinter can be represented as unconsolidated, packed, spherical particles, the effective pore radius can be approximated by $r_{eff} = 0.21D$ [6]. The surface tension (σ) of water at 80 °C saturation is 0.062 N/m. The capillary pressure drop is calculated using the Young-Laplace equation:

$$\Delta P_{cap} = \frac{2\sigma \cos\Theta}{r_{eff}} \tag{5.11}$$

The maximum capillary pressure drop is 7.4 kPa for a receding contact angle (Θ) of 35° for water on copper [6]. For an assumed porosity (φ), ratio of pore volume to total wick volume, of 0.4, the permeability (K) of the sinter can be calculated as 5×10^{-12} m^2 using:

$$K = \frac{D^2 \varphi^3}{150(1-\varphi)^2} \tag{5.12}$$

The viscous pressure drop due to flow through the sinter can be calculated using Darcy's law for porous media:

$$\Delta P = \frac{\mu_l \dot{m} L}{\rho_l A_w K} \tag{5.13}$$

For 80 °C saturated water, the viscosity (μ_l) is 354.33 μPa-s and the density (ρ_l) is 971.77 kg/m^3. The mass flow rate for 4 ccm is 6.67x10^{-5} kg/s and the wick cross sectional area (A_w) is 0.5 mm x 13 mm. If all of the vapor condensed at the inlet and the liquid flowed through the full 80 mm length (L) of sinter channel, the pressure drop would be 60 kPa which is 6 times larger than the measured 9.5 kPa. An alternate scenario would be if all of the vapor condensed at the exit and liquid only flowed through the sinter plug in the outlet hole. Using the vapor properties noted previously and applying Eqn. 5.10 for L_{cond} = L = 80 mm, the pressure drop due to vapor flow through a 0.5 mm x 13 mm channel (A) with a 1 mm hydraulic diameter (D_h) would be 1 kPa. For an outlet diameter (D) of 6.35 mm, a flow length (L) of 3.175 mm and a wick area (A_w) of $\pi D^2/4$, the pressure drop through the sinter is 0.49 kPa leading to a total pressure drop of 1.5 kPa for this flow path. When this 1.5 kPa is added to the maximum capillary pressure drop of 7.4 kPa, complete condensation at the outlet is a plausible explanation for the pressure drop measured for the sinter channel. For capillary pressure less than the maximum, the measured pressure drop could also be explained by low liquid mass flow through the full length of sinter up to the outlet where the remainder of the vapor condenses.

Future work related to condensation and flow through sinter could focus on improved measurement of the capillary pressure and further characterization of wick properties. Literature has demonstrated that confocal microscopy can be used to measure capillary meniscus curvature at wick interfaces while a heat pipe is in operation [29]. This curvature can be used to directly calculate capillary pressure. Additionally, a parametric study can be done to characterize wick permeability and capillary pressure

limit as a function of wick geometry and sintering conditions. This would allow for a better estimation of viscous pressure drop due to flow through the sinter.

Sub-cooling Length Flow Testing

As described in Chapter 5, after validating that the sinter functioned as desired, the test setup was modified such that the experiments would better represent the operation inside the heat pipe design. The heater on the hot tank was operated at constant power input using a reduced voltage of 35 V to 45 V from a variac while the cold tank was held at constant temperature by a circulating bath. By maintaining a line completely filled with liquid downstream of the test section, the saturation condition in the cold tank could be used to set the test section outlet pressure. The flow rate of the backside air cooling was varied from 10 to 40 lpm to maintain a condensing flow rate between 0.4 and 1 ccm through the test section. Absolute pressure transducers were added onto the both tanks, the inlet port, and the outlet port of the test section. Gauge pressure was recorded so that the saturation temperature could be defined at all four locations during experimental testing. To improve imaging of the sinter surface, a 125 W heat lamp, shown in Fig. 5-16, was used to prevent vapor condensation on the polycarbonate viewing plate. A 1.3 mega pixel color camera (PixelInk PL-B742F) recorded condensing flow to provide better differentiation between the liquid and the channel surface. As shown in Fig. 5-17, the color camera and the heat lamp allow for much clearer droplet definition in the open channel and differentiation between the wick and liquid slugs in the sinter channel. Additionally, the image of open channel flow verifies that 40 lpm provides sufficient cooling for the vapor to condense completely within the length of the channel. To accommodate the addition of a sub-cooling length, the o-ring used to seal

the condensing flow side of the test section was replaced with silicone gasketing. As shown in Fig. 5-17(b), occasionally the ultra compressive gasketing used to ensure a good seal would overhang slightly into the channel. As long as the location did not impede flow, experiments were done with the gasket in this condition.

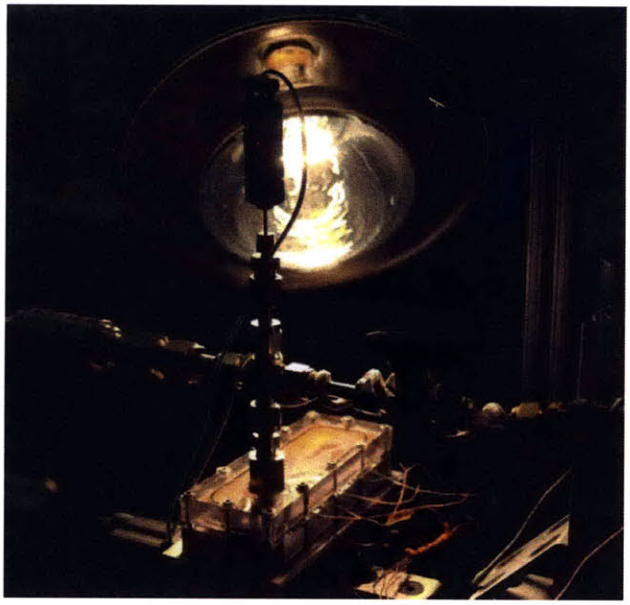

Fig. 5-16 Image of heat lamp used to prevent vapor condensation on the polycarbonate viewing plate during condensing flow with a sinter channel.

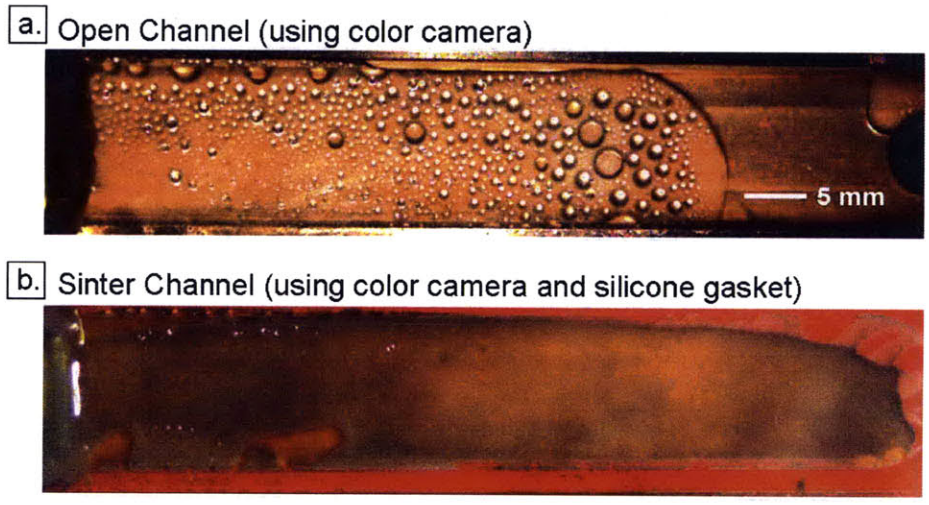

Fig. 5-17 (a.) Image of open channel at a flow rate of 1 ccm with 40 lpm backside cooling recorded using the color video camera. (b.) Image of 40-75 μm sinter channel sealed with silicone gasketing at a flow rate of 0.75 ccm with 20 lpm backside cooling.

A sub-cooling section, as shown in Fig. 5-18, was incorporated into the test section once it was determined that the gasket could form a vacuum seal. The sub-cooling section was manually positioned on the sinter plate and compressed to fill the vapor space above the sinter when the test section was sealed. It is clear that flow bypass did not occur between the sinter and the sub-cooling section because after testing the gasket needed to be peeled off the sinter surface like chewing gum verifying. Without a bypass, the vapor must condense upstream of the sub-cooling section and the condensed liquid must flow through the length of sinter under the gasket to reach the outlet port.

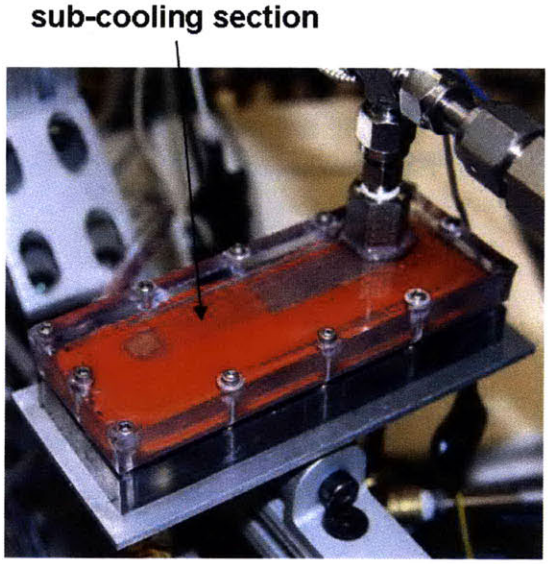

Fig. 5-18 Image of the test section using a silicone gasket for sealing and incorporating a sub-cooling section. The sub-cooling section was typically 25 mm long and the filled the width of the channel.

Within the real heat pipe, the total flow generated by the 1000 W heat input into the evaporator is 0.43 g/s or 26 ccm. This total flow is subdivided into a flow rate of only 0.43 ccm through each sinter surface in the condenser due to the multiple condensers and transfer pipes. Initially, a flow rate of approximately 1 ccm was used for experiments because it was considered a conservative high-end estimate of the real flow rate. An image from these initial tests using 75-100 μm copper sinter is shown in Fig. 5-

19. The heater on the hot tank was set to 45 V to provide 40 W of input power while the cold tank was held at 75 °C. The condensing flow rate was 0.88 ccm ($1.47x10^{-5}$ kg/s) and the backside air-cooling flow rate was 30 lpm. Typically, the entire flow length upstream of the sub-cooling section is filled with vapor and a few liquid slugs above the sinter surface. Subsequent testing attributed the occurrence of liquid slugs to early condensation in the vapor lines due to heat loss at the stainless steel fittings. As shown in the graph in Fig. 5-20, the pressures in the hot and cold tanks set the pressures at the test section inlet and outlet, respectively. The -9.66 psig (34.8 kPa) outlet pressure corresponds to approximately a saturation temperature of 73 °C. Fig. 5-21 shows that the addition of the 26 mm long sub-cooling section causes the condensed water temperature to drop to a 68.8 °C sub-cooled state, which prevents vaporization when the liquid emerges from the wick.

With this sub-cooling length, the pressure drop across the test section was large, 3.8 psi (26.2 kPa) as shown by Fig. 5-20. Using Eqn. 5.12 the permeability (K) of this sinter should be $9.18x10^{-12}$ m^2, assuming a porosity (φ) of 0.4. Eqn. 5.13 is applied to determine the expected viscous pressure drop due to liquid flow through the sinter under the sub-cooling section. Using the properties of saturated 80 °C water, a sub-cooling length (L) of 26 mm, wick cross section (A_w) of 0.5 mm x 13 mm, and a mass flow rate ($\dot{m}$) of $1.47x10^{-5}$ kg/s (corresponding to 0.88 ccm), the expected pressure drop is 2.3 kPa. If this value is subtracted from the measured pressure drop, it suggests that the wick would have to be capable of holding a capillary pressure difference of 23.9 kPa. Applying the Young-Laplace in Eqn. 5.11 for this wick (average particle size 88 μm) assuming an effective pore radius of 18.5 μm, the maximum capillary pressure is only 5.5

kPa. To understand the additional 18.4 kPa of pressure drop, it's important to look at failure modes for the wick. If the pressure drop across the meniscus exceeds capillary pressure, the liquid-vapor interface will recede into the wick. Eqn. 5.13 can be rearranged to solve for flow length (L) as a function of vapor properties at 80 °C and the same mass flow and geometry. The calculations show that a 1.9 mm vapor flow through the sinter will result in an 18.4 kPa pressure drop. Therefore it's plausible that the large measured pressure drop indicates that the condensing flow rate is too high for this sinter to stably maintain a liquid-vapor interface at its surface.

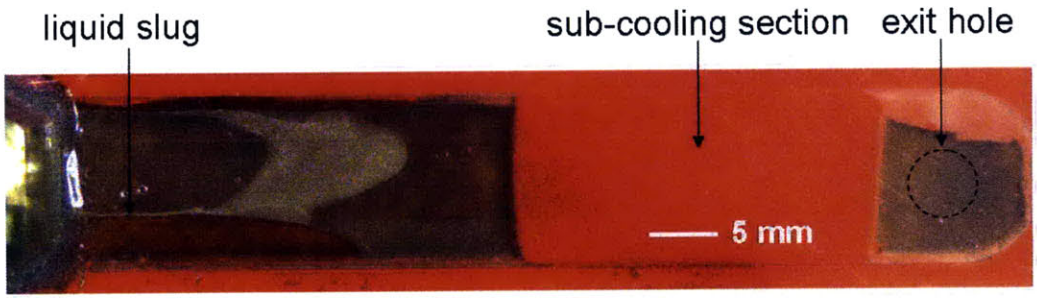

Fig. 5-19 Image of horizontal condensing flow on 75-100 μm sinter at 0.88 ccm and 30 lpm backside cooling.

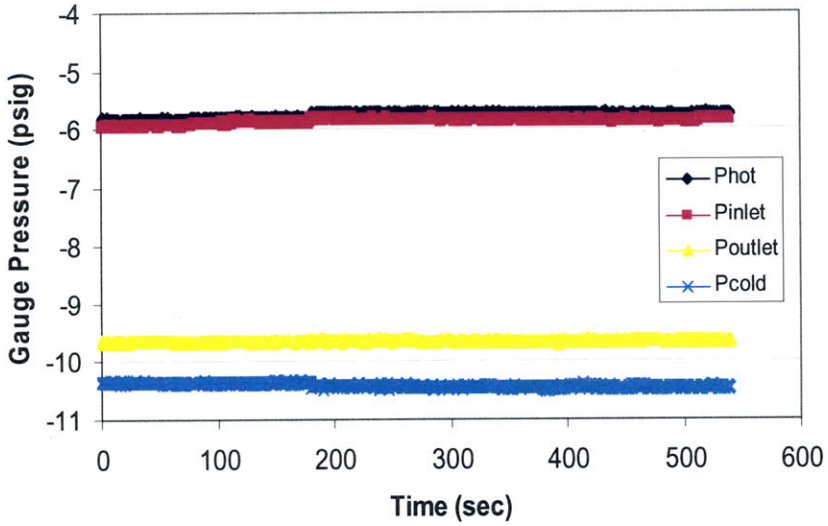

Fig. 5-20 Graph of pressure transducer measurements in psi gauge as a function of time. Data indicates that pressures are stable over the recorded time period. The pressures in the hot and cold tanks seem to set the inlet and outlet pressures, respectively.

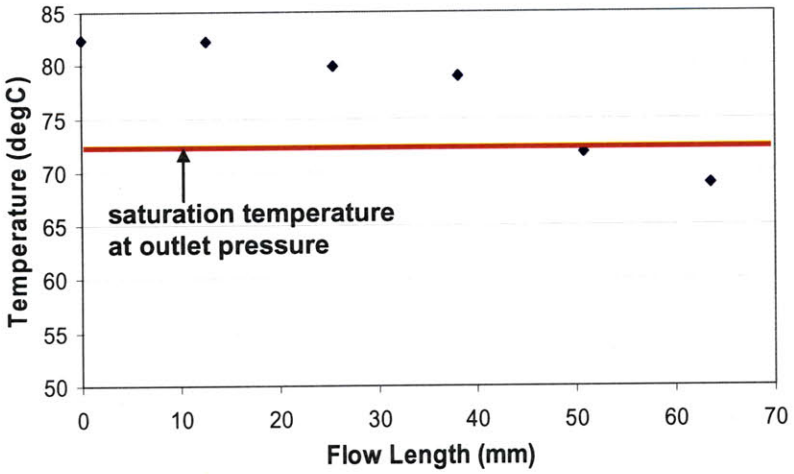

Fig. 5-21 Graph of copper channel plate temperature as a function of flow length. Plate temperatures cross below the saturation temperature, therefore the liquid is sub-cooled at the outlet of the wick.

To investigate this hypothesis and mimic the condenser operation, another sub-cooling experiment was conducted with the condensing flow rate reduced to 0.4 ccm. An image from these tests using 40-90 μm copper sinter is shown in Fig. 5-22. The heater on the hot tank was reduced to 35 V to provide 30 W of input power while the cold tank was held at 75 °C. The sub-cooling length (L) was 28.8 mm and the backside air-cooling flow rate was 10 lpm. Fig. 5-22 shows that the upstream section was vapor-filled above the sinter although occasional pre-condensed liquid slugs would appear. However, unlike the last test, the downstream section surrounding the exit hole had liquid pooling over the entire surface with a single slug contacting the polycarbonate. As shown in the graph in Fig. 5-23, the pressure drop was 1.8 psi (12.4 kPa) and the outlet pressure was -9.54 psig which corresponds to a 73 °C saturation temperature Fig. 5-24 shows that the plate temperature drops below the saturation condition to 70.7 °C such that the liquid leaves the test section sub-cooled.

The pressure drop analysis can be revisited for these new conditions using the same geometry and liquid properties. The permeability (K) for this 40-90 μm sinter was

previously calculated as $5x10^{-12}$ m^2 and the maximum capillary pressure was 7.4 kPa. A volume flow rate of 0.4 ccm converts to a mass flow rate ($\dot{m}$) is $6.67x10^{-6}$ kg/s. Using these parameters and Eqn. 5.13, the liquid viscous pressure drop is 2.2 kPa which corresponds to a 10.2 kPa pressure drop across the wick interface. As in the previous experiment, the required pressure drop exceeds what capillary pressure can provide, but in this case the values are much closer. A different possible explanation for the mismatch could be that the calculated permeability is not accurately representing the sintered wick.

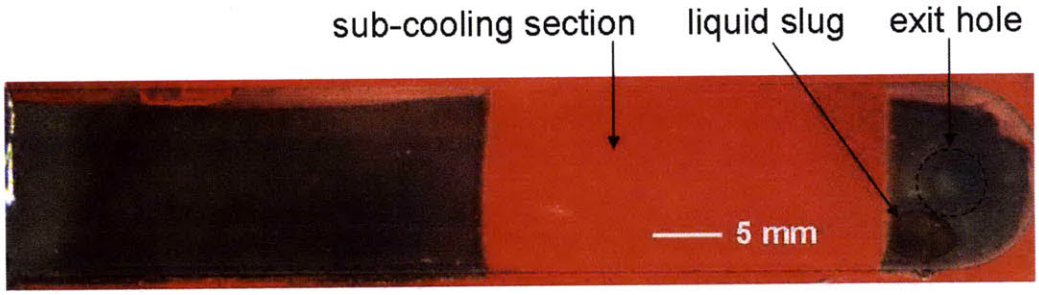

Fig. 5-22 Image of horizontal condensing flow on 40-90 μm sinter at 0.4 ccm and 10 lpm backside cooling.

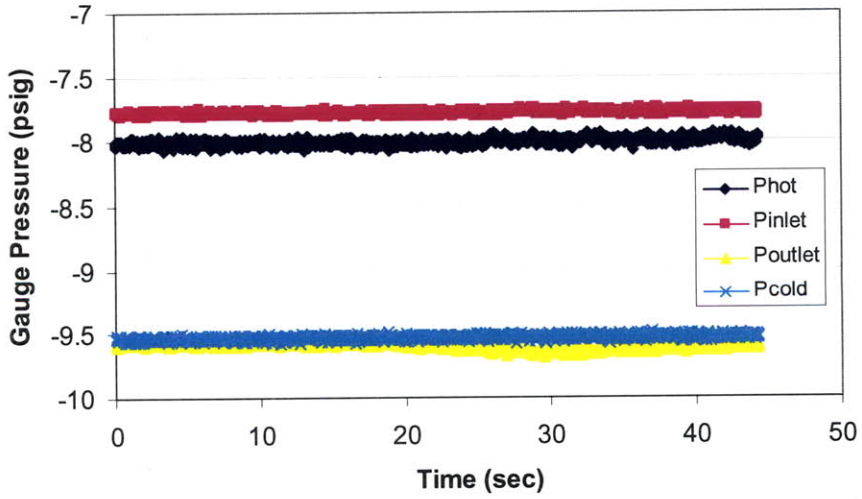

Fig. 5-23 Graph of pressure transducer measurements in psi gauge as a function of time. The test section pressure drop is 1.8 psi or 12.4 kPa.

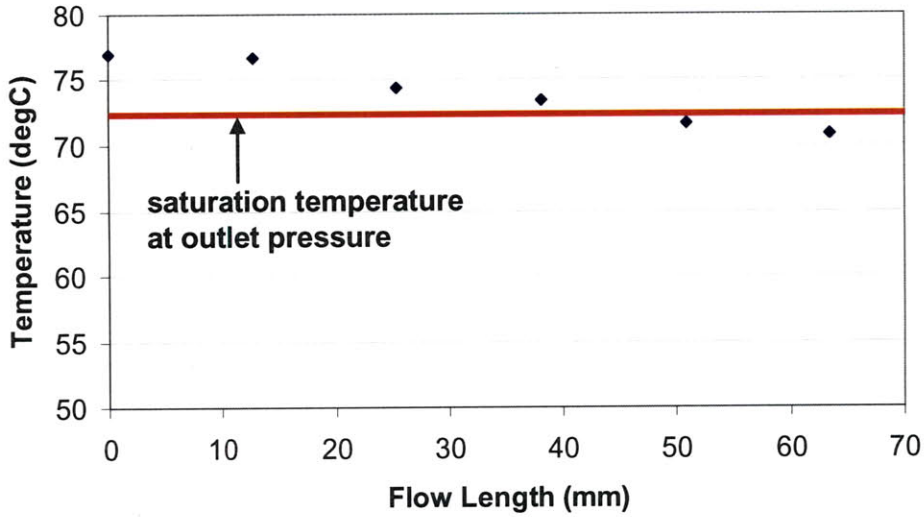

Fig. 5-24 Graph of copper channel plate temperature as a function of flow length for 40-90 μm sinter with a 28.8 mm sub-cooling section at 0.4 ccm. Plate temperatures cross below saturation, therefore the liquid is sub-cooled at the outlet.

To measure the real permeability of the sinter wick, the test section was modified as shown in Fig. 5-25. The test section was disconnected from the tanks, leaving the liquid flow meter downstream, and a pressurized water reservoir was added at the inlet. Another piece of the gasket material used for the sub-cooling section was cut to cover the entire sinter surface except for a circular opening under the inlet. The gasket ensured that all liquid entering the test section flowed only through the sinter layer on the way to the outlet. As the pressure was increased in the reservoir, the liquid flow rate through the sinter and the pressure drop across the test section increased. The graph in Fig. 5-26 shows the pressure drop (ΔP) at each flow rate (Q) and the linear trend line that fits the data. The slope of 9.8×10^{12} can be used in Eqn. 5.14 to calculate the permeability of the sinter:

$$K = \frac{\mu_l Q L}{A_w \Delta P} = \frac{\mu_l L}{slope \times A_w} \tag{5.14}$$

For a cross section (A_w) of 0.5 mm by 13 mm, a flow length (L) of 80 mm, and a liquid viscosity (μ_l) of 932.16 μPa-s at 23 °C and 1 atm, the permeability is 1.17×10^{-12} m^2. Compared to the calculated permeability of 5×10^{-12} m^2, the measured permeability is 4.3 times smaller. If this lower measured permeability is used to calculate viscous pressure drop under the sub-cooling section, the corrected pressure drop would be 9.2 kPa. If subtracted from a total pressure drop of 12.4 kPa, the capillary pressure would only have to support 3.2 kPa which is well within its 5.4 kPa maximum limit. The measured permeability may be lower than calculated for a variety of reasons. The calculated value assumes a single particle diameter where the real sinter powder has a range of sizes that can result in smaller particles filling the voids created between larger particles. Additionally, the sintering conditions can affect the way that particles fuse together resulting in a more compact porous structure. Also, the channel geometry has a lot of surface area relative to volume, so there could be significant edge effects. In light of the difference in permeability, the sintered wick should be characterized in the condenser geometry so that a wick can be chosen that can handle the expected condenser flow rates while maintaining a stable liquid-vapor interface at the wick surface. If the wick is appropriately chosen, the results of this experimental testing show that a sub-cooling section can adequately reduce the condensate temperature so that it is sub-cooled at the condenser outlet.

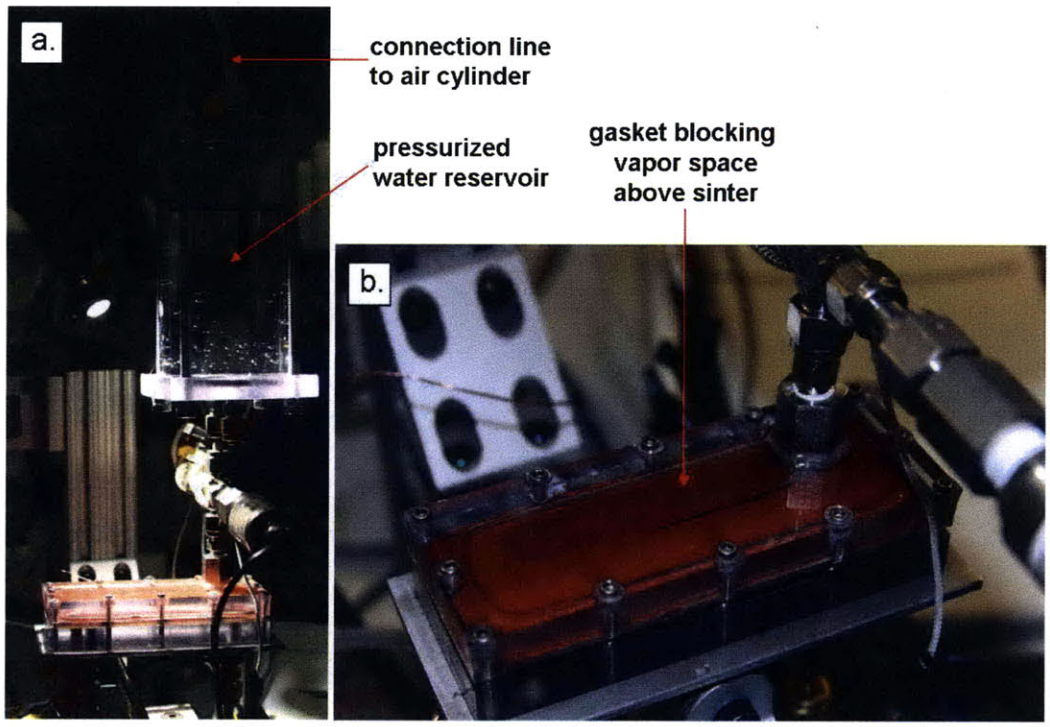

Fig. 5-25 (a.) Image of the pressurized water reservoir attached to the test section as the liquid source for permeability testing. (b.) Image of the test section with gasket covering the entire sinter surface except for an opening under the inlet.

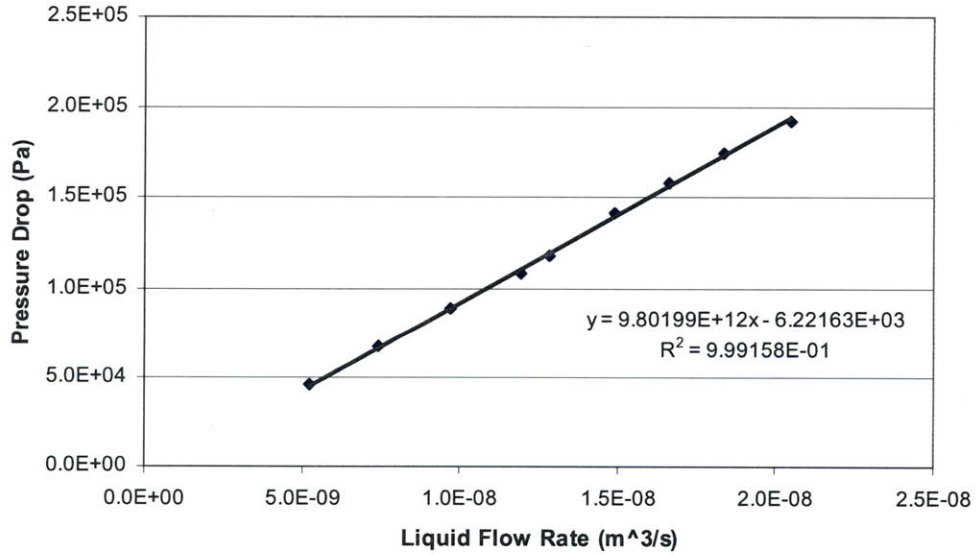

Fig. 5-26 Graph of measured pressure drop versus flow rate for flow through the 40-90 μm sinter wick. The slope is used to calculate permeability.

In future work, a lot can be done with the current test section and experimental setup to expand understanding of these test results and to develop new tests that can

further evolve the condenser design. The sub-cooling section testing was the most recent work. Further experiments should be done to optimize the length of the sub-cooling section to balance viscous pressure drop and required temperature reduction. Additionally, more testing at low condensing flow rates is needed to better estimate the pressure drop expected under flow conditions within the heat pipe.

During experimental testing, it was noted that over time condensate began pooling on the sinter surface instead of wicking in. The initial hypothesis was that the copper sinter became hydrophobic due to exposure to non-condensables and contaminants in the working fluid. Work to improve water quality and eliminate contaminants such as vacuum grease from the setup did not prevent the problem from continuing to occur, suggesting that new methods of cleaning the sinter plates between tests are needed. Possible solutions are acid cleaning or rerunning the plates through a sintering cycle at high temperature and a reducing atmosphere. Additionally in between sintering and experimental testing, the plates are stored in a nitrogen dessicator. Despite the minimum exposure to air, the sinter becomes hydrophobic after only a few days. This inability to retain surface chemistry suggests that maybe a more robust solution is needed such as oxidizing the entire surface or adding a hydrophilic coating.

To test a geometry that better replicates the current condenser design, the test section and channel plate can be modified as shown in Fig. 5-27. The vapor will still enter the test section at the same location, but then follow a dead ending flow path, forcing it to completely condense on the sinter surface. The condensate will then flow in a perpendicular direction through the sinter and under the sub-cooling section where it will reduce in temperature. Then the liquid will flow to the outlet through the sinter and

an open liquid path. This design would allow for testing to quantify the expected pressure drops and sub-cooling temperatures inside the heat pipe condenser for varying sinters and lengths of sub-cooling.

Finally, the test setup can be modified in several ways to experiment with the flooding failure mode due to gravity head between the parallel condensers. One solution is to fabricate another identical test section and operate the setup with one condenser 10 cm above the other. In addition to visual monitoring of the lower condenser for flooding, the liquid pipes exiting each condenser can be instrumented with mass flow meters to quantify flow balance. Another option is to modify the setup as shown in Fig. 5-28. The test section outlet tube is extended to create a 10 cm tall liquid column. The liquid exiting the column will trickle down the walls of the much larger pipe such that the top surface of the column is at cold tank pressure. By adjusting pressure and mass flow, conditions that lead to flooding can be explored.

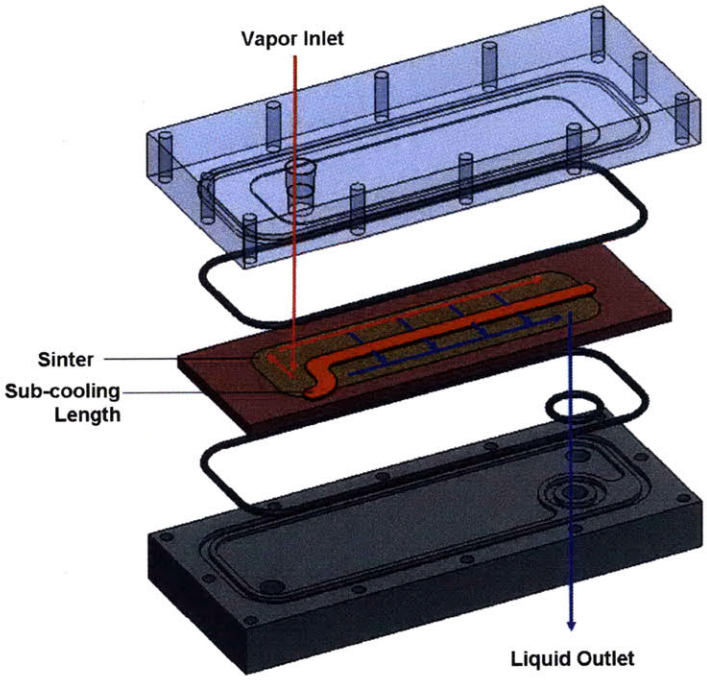

Fig. 5-27 Schematic of condensing flow through test section with updated geometry to mimic the flow direction of liquid under the sub-cooling section in real condenser.

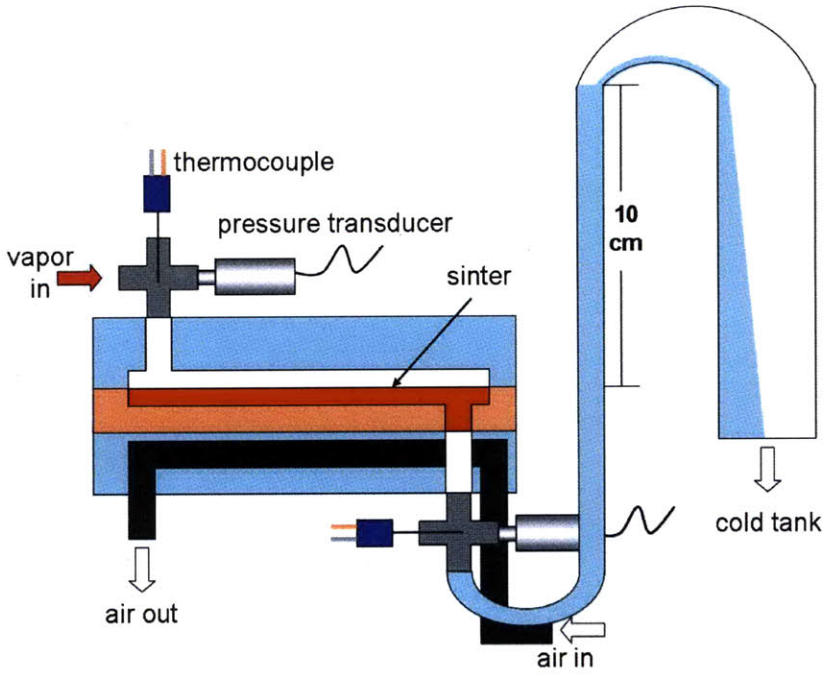

Fig. 5-28 Schematic of test section design for creating 10 cm gravity head on test section outlet to test for conditions that cause condenser flooding.

Chapter 6: Conclusions and Future Work

In this work, parallel plate condensers for a loop heat pipe were designed and experimentally investigated for use in a high power dissipation compact heat exchanger. The design required large surface areas maintained at a uniform high temperature of 80 °C and even mass flow distribution between the parallel layers to maximize heat transfer to the cooling air. Analytic modeling suggested that an ideal geometry would include high flow resistance in the condenser layers to balance flow and pressure drop exceeding gravitational head in the condenser and liquid pipes to prevent flooding. These results pointed toward a condenser design with sinter wick lining the condensation surfaces and a sub-cooling length to reduce condensate temperature before entering the liquid pipe.

An experimental setup was designed, fabricated, and revised multiple times in order to closely replicate the conditions and control within the LHP. The final iteration was a table-top setup consisting of a constant heat input vapor source, a constant temperature liquid reservoir setting test section outlet pressure, and air-cooling for condensation heat removal. Three different methods of deaeration were investigated as a means to process the working fluid, water, prior to use in the experimental setup. Freeze-pump-thaw cycling of water within the tank used as the vapor source was shown to remove the highest volume of non-condensable gases.

Experiments on condensing flow were conducted with open and sinter filled channels. Horizontal open channel flow demonstrated a condensing length beyond which the condensate sharply decreased in temperature. When orientation was varied, the open channel flow was shown to be heavily influenced by gravity. Further experiments demonstrated that lining the condenser interior with sinter resulted in isothermal plate

temperatures and stable flow patterns due to phase separation. However the incorporation of sinter also made it necessary to sub-cool the condensate before it returned to the liquid lines in order to prevent vaporization upon emerging from the wick. Experiments with a sub-cooling length demonstrated that directing the flow through the wick before the outlet reduced the liquid temperature below saturation conditions at the cost of large pressure drops in the channel. At high flow rates, that pressure drop exceeds the capillary pressure that condenser wick is able to support. Further work on sub-cooling should focus on lower flow rates and geometries that more closely replicate the condenser design.

Several examples of future work were described in the experimental results chapter. In addition to those ideas, the wick sinter size and sub-cooling length can be optimized to achieve the best trade off between permeability and capillary pressure and between sub-cooling and pressure drop. An ideal design provides adequate temperature reduction at a pressure drop manageable by the capillary interface at the condenser wick surface. To aid this optimization, sinter cleaning methods need to be developed to ensure that the sinter wick has constant, known surface chemistry in each experiment. In addition to controlling the wick surface properties, further effort is needed to prevent condensation from occurring in the vapor line. Although multiple rope heaters were used to superheating the incoming vapor, the continued presence of liquid drops implies a need for further reduction of inlet distance and addition of insulation to protect against heat loss.

It may be possible to better quantify the effect of the sub-cooling section with additional thermocouples. Currently the temperature is monitored with 6 thermocouples

spaced 13 mm apart in the copper plate. Only one of these thermocouples is located under the sub-cooling section, and none of these thermocouples give the temperature of the liquid where it re-emerges from the wick after the sub-cooling section. By adding more thermocouples, resolution of the plate temperature profile can be improved. Ideally a thermocouple could be integrated directly into the liquid space at the channel exit.

Freeze-pump-thaw degassing made the most significant reduction in the non-condensable gas content of the water used in this apparatus. This method may be useful as part of a heat pipe filling process. However, unlike the condensing flow setup that runs open loop, the heat pipe would need to be charged with a exact amount of working fluid. Therefore, a potential solution is to develop a filling station with a manifold that interfaces a vacuum pump, a syringe, the heat pipe filling line, and the tank of degassed water.

Although experimental testing in this setup can help define the governing parameters of the condenser design, a more accurate experiment would be for the test section to mimic the full 10 cm x 10 cm plate condenser. The current test section only allows for one straight, constant cross-sectional area flow path; however the flow in the real condenser spreads from a single vapor inlet to two liquid outlets in a curved path around the central airflow core. Behavior of the condensing flow could change due to these dimensional differences and warrants investigation.

Finally, a single sealed condenser must be manufactured for integration with an evaporator to validate a single layer of the loop heat pipe. Then, a complete 15 layer condenser loop heat pipe will be fabricated and integrated with the blower components to

validate that the entire heat exchanger design can achieve its required high efficiency power dissipation and low thermal resistance metrics.

Acknowledgements

The author gratefully acknowledges the help and support of Professor Evelyn Wang, Professor John Brisson, and Dr. Teresa Peters, whose ideas and guidance were instrumental in completing this work. The author would also like to acknowledge the entire project team working on the heat exchanger design: Professor Jeffrey Lang, Dr. Matt McCarthy, Arthur Kariya, David Jenicek, Jonathan Allison, Alonso Dominguez, and Mike Demaree. The author would finally like to acknowledge the financial support for this work provided by the Defense Advanced Research Projects Agency (DARPA) Microsystems Technology Office (MTO) Grant Number W31P4Q-09-1-0007, Microtechnologies for Air-Cooled Exchangers (MACE) with Dr. Tom Kenny as the contract monitor.

Bibliography

[1] G.E. Moore. "Cramming more components onto integrated circuits", Electronics Magazine, vol. 38, no. 8 (1965).

[2] I. Mudawar. "Assessment of high-heat-flux thermal management schemes", IEEE Transactions on Components & Packaging Technologies, vol. 24, no. 2 (2001), pp. 122-141.

[3] Aavid Thermalloy. (2010, May) Thermal Solutions for Intel® Server CPU. [Online] http://www.aavidthermalloy.com/

[4] ThermalTake. (2010, May) CPU Coolers. [Online] http://www.thermaltakeusa.com/

[5] Kingwin Technology Inc. (2010, May) CPU Coolers. [Online] http://kingwin.com/

[6] A. Faghri. Heat Pipe Science and Technology. Taylor & Francis, London, 1995.

[7] Yu.F. Maydanik. Review. "Loop Heat Pipes", Applied Thermal Engineering, vol. 25, no. 5-6 (2005), pp. 635-657.

[8] S. Launay, V. Sartre, J. Bonjour. "Parametric analysis of loop heat pipe operation: a literature review", International Journal of Thermal Sciences, vol. 46, no. 7 (2007), pp. 621-636.

[9] R. Singh, A. Akbarzadeh, M. Mochizuki. "Thermal potential of flat evaporator miniature loop heat pipes for notebook cooling", IEEE Transactions on Components and Packaging Technologies, vol. 33, no. 1 (2010), pp. 32-45.

[10] M.A.Chernysheva, S.V. Vershinin, Yu.F. Maydanik. "Development and test results of loop heat pipes with a flat evaporator", Proc. of 12th Int. Heat Pipe Conf (2002).

[11] N. Riviere, V. Sartre, J. Bonjour. "Fluid mass distribution in a loop heat pipe with a flat evaporator". Proc. of 15th Int. Heat Pipe Conf (2010).

[12] I. Muraoka, F.M. Ramos, V.V. Vlassov. "Experimental and Theoretical Investigation of Capillary Pumped Loop with a Porous Element in the Condenser," International Journal of Heat and Mass Transfer, vol.25, no.8 (1998), pp.1085–1094.

[13] Z. Liu, W. Liu, and J. Yang. "Experimental investigation of new flat-plate-type capillary pumped loop," Journal of Thermophysics and Heat Transfer, vol. 22, no. 1 (2008), pp. 98-104.

[14] A.S. Dalkilic, S. Wongwises. "Intensive literature review of condensation inside smooth and enhanced tubes". International Journal of Heat and Mass Transfer, vol. 52, no. 15-16 (2009), pp. 3409–3426.

[15] L. Cheng, G. Ribatski, J.R. Thome. "Two-phase flow patterns and flow-pattern maps: Fundamentals and applications", Applied Mechanics Reviews, vol. 61, no. 1-6 (2008), pp. 0508021-05080228.

[16] A. Tabatabai, A. Faghri. "A new two-phase flow map and transition boundary accounting for surface tension effects in horizontal miniature and micro tubes". Journal of Heat Transfer, vol. 123, no. 5 (2001), pp. 958-968.

[17] W.M. Rohsenow, J.P. Hartnett, Y.I. Cho. Handbook of Heat Transfer (3rd Edition). McGraw-Hill. 1998.

[18] R. Sander. "Compilation of Henry's Law Constants for Inorganic and Organic Species of Potential Importance in Environmental Chemistry." April 8, 1999. http://www.mpch-mainz.mpg.de/~sander/res/henry.html

[19] Welch Vacuum Technology. (2010, May) Two-Stage Belt Drive Vacuum Pump Model 1402. [Online] http://www.welchvacuum.com/

[20] D.W. Green, R.H. Perry. Perry's Chemical Engineering Handbook (8^{th} edition). McGraw-Hill. 2008.

[21] Vernier Software & Technology. (2010, May) Dissolved Oxygen Probe DO-BTA. [Online] http://www2.vernier.com/booklets/do-bta.pdf

[22] University of Houston, Advincula Research Group. (2010, May) "Procedure for Degassing of Liquids using Freeze-Pump-Thaw." [Online] http://www.nanostructure.uh.edu/Forms/FPT%20procedure.pdf

[23] Alcatel Vacuum Products, Inc. (2010, May) Rotary Vane Pumps Model 2010SD. [Online] http://www.adixen-usa.com/roughing_pumps/

[24] E.W. Lemmon, M.L. Huber, M.O. McLinden, NIST Standard Reference Database 23: Reference Fluid Thermodynamic and Transport Properties-REFPROP, Version 8.0, National Institute of Standards and Technology, Standard Reference Data Program, Gaithersburg, 2007.

[25] A.F. Mills Heat and Mass Transfer. 2^{nd} ed. New Jersey: Prentice-Hall, 1999.

[26] A. Kariya et al., "A Capillary-Pumped Loop Heat Pipe with Multi-Layer Microstructured Wicks," 9th International Workshop on Micro and Nanotechnology for Power Generation and Energy Conversion Applications (PowerMEMS 2009), Washington D.C., 2009, In press.

[27] O. Baker, "Simultaneous Flow of Oil and Gas," Oil & Gas Journal, vol. 53 (1954), pp.185–195.

[28] J.W. Coleman and S. Garimella. "Two-phase flow regimes in round square and rectangular tubes during condensation of refrigerant R134a," Int. J. Refrig. vol. 26 (2003), pp. 117–128.

[29] F. Lefèvre, R. Rullière, S. Lips, and J. Bonjour. "Confocal Microscopy for Capillary Film Measurements in a Flat Plate Heat Pipe." J. Heat Transfer, vol. 132, no. 3 (2010), article 031502 (6 pages).

Appendix A

Matlab code to calculate the mass flow rate distribution within the parallel condenser layers.

```
function [DP,M] = condenser_flow3(RS,RL,RV,Pg,Pcap2)
% includes capillary pressure drop - appropriate for sinter

% RS = input condenser flow resistance
% RL = input liquid pipe flow resistance
% RV = input vapor pipe flow resistance
% Pg = input total gravity pressure head
% Pcap2 = input constant capillary pressure in condenser wick

%%
n_max=18;       % maximum number of stators
m0 = 0.433/2;   % total mass flow (g/s) - 1/2 because 2 of each pipe

q=1;
M=zeros(2*n_max,n_max/2);
DP=zeros(n_max/2,1);

for n = 2:2:n_max   % number of stators

    Rs = RS/1000;             % resistance of stator
    Rl = (RL/1000)/n;         % resistance of liquid pipe with sinter
    Rv = (RV/1000)/n;         % resistance of vapor pipe
    DPg = Pg/n;               % pressure rise due to gravity

    R = zeros(2*n,2*n);       % resistance matrix
    P = zeros(2*n,1);         % pressure drop matrix

    E = 1e-5;   % allowable error on mass flow difference
    error = 1;

    P_guess = 5000; % pressure drop guess (Pa)

    % Equation 1 (i=1)
    R(1,1) = -Rl; % battery
    R(1,2) = -Rs; % middle
    R(1,3) = -Rv; % bottom
    P(1) = -P_guess - Pcap2 + DPg;
    % Mass Balance
    R(n+1,1) = 1;
    R(n+1,2) = -1;
    R(n+1,3) = -1;

    % -(a+c)*m(2i-1) - b*m(2i) + b*m(2i-2) = -DPg
    for i=2:n-1
        % R matrix (Coefficients of mass flow rates)
        R(i,2*i-1) = -(Rl+Rv);
        R(i,2*i)   = -Rs;
```

```
        R(i,2*i-2) = Rs;

        % pressure rise due to gravity term in each loop
        P(i) = DPg;

        % Mass Balances (in-out-out = 0 such as i=2, m3 - m4 - m5 = 0)
        R(n+i,2*i-1) = 1;
        R(n+i,2*i)   = -1;
        R(n+i,2*i+1) = -1;
        P(n+i)       = 0;

    end

    % final equation
    % Only difference in final equation is the mass balance.
    % R matrix (Coefficients of mass flow rates)
    R(n,2*n-1) = -(Rl+Rv);
    R(n,2*n)   = -Rs;
    R(n,2*n-2) = Rs;

    % pressure rise due to gravity term in each loop
    P(n) = DPg;

    % Mass Balances (in - out - out = 0 such as i=2, m3 - m4 - m5 = 0)
    R(n+n,2*n-1) = 1;
    R(n+n,2*n)   = -1;
    P(n+n)       = 0;
    % End of final equation

    while (abs(error) > E)
        m=R\(-P);               % create array of mass flow rates (g/s)
        error=m(1)-m0;          % difference between actual and solved
values for mass flow
        P_guess = P_guess -(error/100)*P_guess; % increment guess to
try new value
        P(1) = P_guess - Pcap2 + DPg;
    end

    M(1:2*n,q)=m;
    DP(q)=P_guess;
    q=q+1;
end
```

Appendix B

Labview Program used to record data during experimental condensing flow testing.

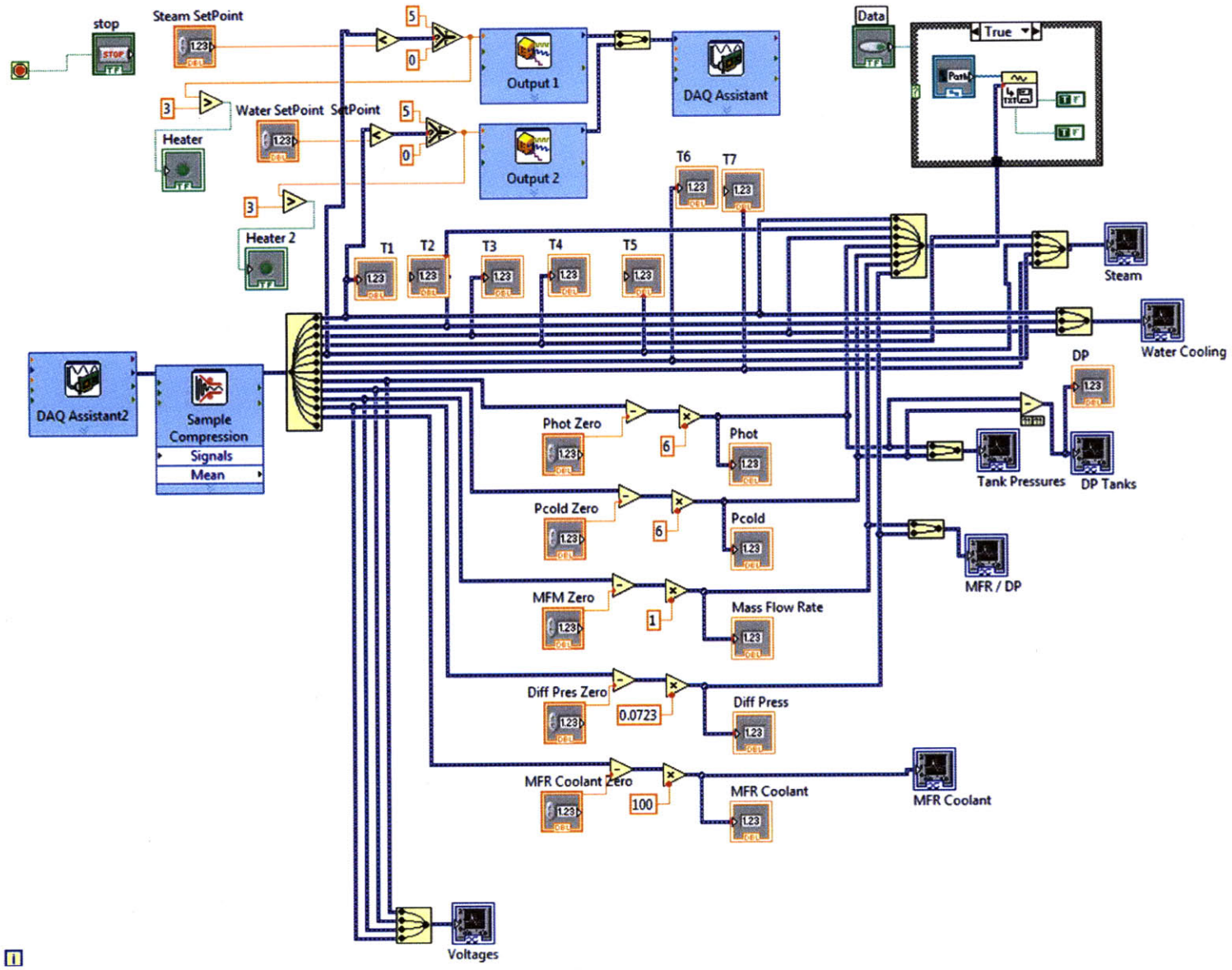

Fig. B-1 Block diagram for Labview program used to record pressure, temperature and mass flow data in experimental setup. Program also controlled heaters by outputting voltages to solid state relays.

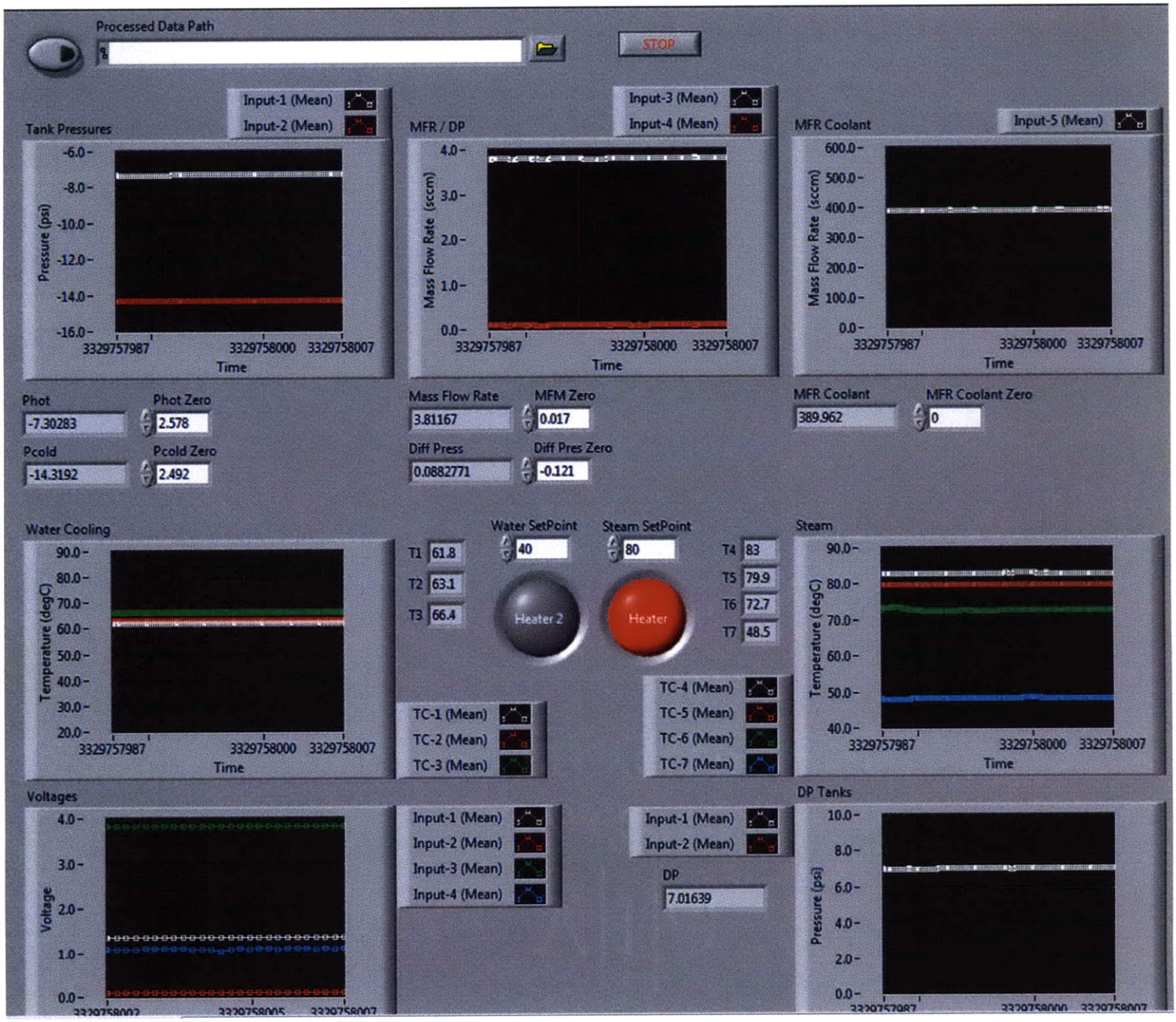

Fig. B-2 Interface for Labview program used to monitor temperature, pressure and mass flow rate graphically over time. Interface included offsets for zeroing equipment as a means of calibrating before testing and inputs for set point temperatures for heaters to turn on.

Appendix C

Matlab code for two-phase condensing flow mapping.

```
close all
clear all
clc

% properties of water at 80 degC
rhol=971.77;          % liquid density (kg/m^3)
rhov=0.294;           % vapor density (kg/m^3)
hfg=2308e3;           % heat of vaporization (J/kg)
mul=354.33e-6;        % liquid viscosity (Pa-s)
muv=11.592e-6;        % vapor viscosity (Pa-s)
sigma=62.673e-3;      % surface tension (N/m)

% heat transfer properties
Q=1000;         % power dissipation per stator (W)
h=80;         % heat transfer coefficient (W/m^2K)
Tsat=80;      % saturated vapor temp (degC)
Tair=30;      % air temp (degC)

% system properties
N=15;         % number of stators
a=20e-3;      % stator width (m)
b=1e-3;       % stator height (m)

A=a*b;                % stator cross-sectional area (m^2)
Dh=2*a*b/(a+b);       % hydraulic diameter (m)
P=2*a+2*b;            % perimeter (m)

mdot=(Q/N)/hfg;       % total mass flow (kg/s)
G=mdot/A;         % total mass flux (kg/m^2s)

% length to condense completely
L=(Q/N)/(h*2*a*(Tsat-Tair));  % pipe length (m)

% quality (x) - assume linear relation
z=0:0.001:L;      % length of pipe from 0 to L (m)
x=1-z/L;          % quality at each position z

% void fraction (alpha)
rho_ratio=rhov/rhol;
x_ratio=(1-x)./x;
alpha=1./(1+rho_ratio.*x_ratio.*(0.4+0.6.*sqrt((1/rho_ratio+0.4*x_ratio
)./(1+0.4*x_ratio))));

% velocity ratio (v_ratio) : V_ratio = Vv / Vl
V_ratio=(rhol/rhov).*((1-alpha)./alpha).*(mdot*hfg-h*2*a*(Tsat-
Tair).*z)./(h*2*a*(Tsat-Tair).*z);

% pressure drop ratio (P_ratio) : P_ratio = (dP/dz)sigma / (dP/dz)l +
(dP/dz)v
```

```
P_ratio=(sigma./(4.*alpha*G)).*1./((mul.*(1-x)/rhol)+(muv.*x/rhov));

% boundary between annular and slug/plug flow
boundaryB=1/0.06-1;

% graph of flow map for heatpipe
loglog(P_ratio,V_ratio,'linewidth',2)
hold on
grid on
xlim([10^(-2) 10^6])
ylim([10^(-4) 10^4])
line([10^(-2) 10^6],[boundaryB boundaryB],'color','g','linewidth',2)
xlabel('(dP/dz)_\sigma / (dP/dz)_\tau')
ylabel('V_v / V_l')
legend('LHP design','B: annular to slug/bubble','location','southeast')
```